

REPORT NO.  
UCB/EERC-83/12  
JUNE 1983

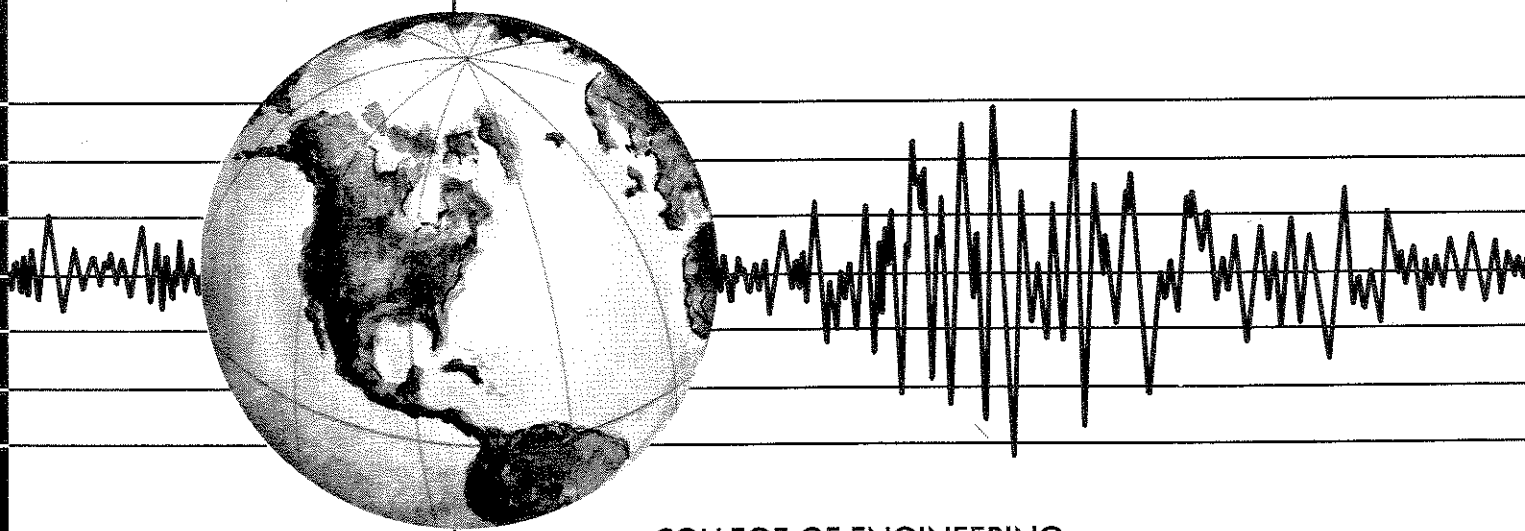
EARTHQUAKE ENGINEERING RESEARCH CENTER

# EXPERIMENTAL ERROR PROPAGATION IN PSEUDODYNAMIC TESTING

by

PUI-SHUM B. SHING  
STEPHEN A. MAHIN

Report to the National Science Foundation



COLLEGE OF ENGINEERING  
UNIVERSITY OF CALIFORNIA • Berkeley, California

**EXPERIMENTAL ERROR PROPAGATION  
IN  
PSEUDODYNAMIC TESTING**

by

Pui-shum B. Shing

and

Stephen A. Mahin

A Report to Sponsor  
National Science Foundation

Report No. UCB/EERC-83/12  
Earthquake Engineering Research Center  
College of Engineering  
University of California  
Berkeley, California

June 1983

## ABSTRACT

This report presents the findings of an analytical study regarding the propagation of experimental errors during seismic performance testing of structural systems by an on-line computer-control (pseudodynamic) method. Numerical methods for suppressing the error-propagation effects are proposed and investigated, so that reliable experimental results can be obtained.

The pseudodynamic method is a relatively new experimental technique which can simulate quasi-statically the seismic response of large scale structural models using a computer-controlled actuator system and a numerical integration algorithm. This method uses step-by-step numerical integration to solve the equations of motion for a structural system with the nonlinear structural restoring forces directly measured from the test specimen during an experiment; and the mass and damping properties of the structure are modelled using idealized analytical assumptions. In each step of a test, errors in restoring force measurements are introduced into the numerical computations. Due to the large number of integration steps involved in a single test, the cumulative errors can be significant even though the actual experimental feedback errors within each step are relatively small.

This study looks into the possible sources and the characteristics of experimental feedback errors in pseudodynamic testing, and presents a general analytical technique to study the error-propagation behavior of step-by-step integration algorithms. The error-propagation characteristics of three explicit algorithms recommended for pseudodynamic testing are investigated. Equations are also formulated to estimate the upper cumulative error bounds for both single- and multiple-degree-of-freedom linear elastic tests. In addition, error propagation in inelastic testing is examined and compared with the linear elastic results.

The results of this study indicate that certain systematic experimental errors are most detrimental to pseudodynamic testing, particularly to multiple-degree-of-freedom tests. Significant energy effects are induced by these errors, and the higher frequency modes of a test specimen can be erroneously excited. Based on these findings, two numerical methods are

proposed to compensate for these error effects and to suppress the spurious growth of higher frequency responses. It is shown that reliable pseudodynamic test results can be obtained if adequate experimental equipment and technique, and appropriate numerical methods for mitigating error-propagation effects are used. Guidelines for achieving reliable pseudodynamic test results are also discussed in this report.



## ACKNOWLEDGEMENTS

The financial support of the National Science Foundation in sponsoring this study and the development of the pseudodynamic test facilities is gratefully acknowledged. Most of the numerical simulations in this report were performed with the pseudodynamic test system and computer software at the Structural Engineering Laboratory at Berkeley. Chris Thewalt developed the data reduction and computer graphics programs which were used to illustrate the simulation results in this report. Gail Feazell did the drafting. The contributions of these persons to the publication of this report are appreciated.

# TABLE OF CONTENTS

	Page
ABSTRACT	i
ACKNOWLEDGEMENTS	iii
TABLE OF CONTENTS	iv
1. INTRODUCTION	1
1.1 The Pseudodynamic Method	1
1.2 Previous Research and Limitations	2
1.3 Numerical Formulation	3
1.4 Error Propagation Effect	5
1.5 Objectives and Scope	6
2. EXPERIMENTAL ERRORS	8
2.1 Classification and General Expressions	8
2.2 Systematic Errors	10
2.3 Random Errors	20
2.4 Concluding Remarks	20
3. EVALUATION OF INTEGRATION ALGORITHMS	22
BASED ON EXPERIMENTAL ERROR PROPAGATION	
3.1 Recursive Form of Integration Algorithms	22
3.2 Error Cumulation Equation	24
3.3 Cumulative Displacement Errors	26
3.4 Error Propagation in the Explicit Numerical Algorithms	29
3.5 Comparisons and Comments	31
3.6 Numerical Examples	33
4. ERROR PROPAGATION CHARACTERISTICS	36
IN SDOF LINEAR ELASTIC SYSTEMS	
4.1 General Cumulative Error Equation	36

4.2	Random Errors	37
4.2.1	Drift Effect	37
4.2.2	Statistical Error Bound	38
4.2.3	Example	40
4.3	Systematic Errors	41
4.3.1	Sinusoidal Errors	41
4.3.2	Resonance Effect and Error Bound	42
4.4	General Errors of Mixed Form	44
4.4.1	Fourier Transformation	44
4.4.2	Implications of Fourier Spectrum	47
4.4.3	Examples	48
4.5	Concluding Remarks	49
5.	ERROR PROPAGATION CHARACTERISTICS	50
	IN MDOF LINEAR ELASTIC SYSTEMS	
5.1	Cumulative Errors in MDOF Systems	50
5.1.1	Modal Superposition Method	50
5.1.2	Cumulative Errors by Modal Superposition	53
5.2	Random Errors	54
5.2.1	Preliminary Considerations	54
5.2.2	Statistical Error Bounds	56
5.2.3	Implications of the Error Bounds	57
5.3	Influence of Structural Characteristics on Error Propagation	58
5.3.1	K-Braced Steel Frame	58
5.3.2	Reinforced Concrete Shear-Wall Structure	59
5.3.3	Comparisons and Comments	60
5.4	Systematic Errors	61
5.5	Numerical Simulations	63

5.6 Force, Velocity, and Acceleration Errors	65
5.7 Summary	66
6. ERROR PROPAGATION IN INELASTIC SYSTEMS	67
6.1 Introduction	67
6.2 SDOF Elasto-Plastic Systems	67
6.2.1 Cumulative Error Equation	68
6.2.2 Equivalent Displacement Errors	69
6.3 Numerical Simulations using the Elasto-Plastic Model	70
6.3.1 System Description and Numerical Results	70
6.3.2 Implications Regarding Inelastic Error Propagation	71
6.4 Parametric Studies of Error Propagation	72
6.4.1 Error Ratio Spectra	73
6.4.2 Relative Error Spectra	74
6.4.3 Error Spectra under Various Conditions	74
6.4.4 Commentary	75
6.5 Reliability Criteria in Inelastic Pseudodynamic Testing	76
7. ERROR COMPENSATION AND NOISE REMOVAL METHODS FOR PSEUDODYNAMIC TESTING	78
7.1 Introduction	78
7.2 Equivalent Hysteretic Energy Compensation	79
7.2.1 Theoretical Basis	80
7.2.2 Application	82
7.2.3 Examples	83
7.3 Noise Removal by Numerical Damping	84
7.3.1 Orthogonal Viscous Damping	85
7.3.2 Dissipative Explicit Algorithm	86
7.3.3 Examples	88

7.4 Comments	90
8. CONCLUSIONS AND RECOMMENDATIONS	91
8.1 Summary	91
8.2 Recommendations for Pseudodynamic Testing	93
8.2.1 Preliminary System Check	93
8.2.2 Improvement Methods	94
8.3 Concluding Remarks	95
REFERENCES	96
TABLES	98
FIGURES	108
APPENDIX A	156
APPENDIX B	159
APPENDIX C	165
APPENDIX D	167

# CHAPTER 1

## INTRODUCTION

### 1.1. The Pseudodynamic Method

For economic reasons, structures are usually designed to deform inelastically when subjected to severe earthquake excitations. However, a well-designed structure should remain stable and be capable of dissipating substantial energy during rare and unusually intense earthquakes. To improve existing building code provisions based on this design philosophy, the inelastic seismic performance of structural systems and components should be well understood. This knowledge can be best accumulated through experimental testing. Experimental data can also provide useful information for developing realistic analytical models for predicting the inelastic behavior of structures.

Most available experimental methods for seismic performance testing suffer from limitations of one type or another [1]. Recently, it has been suggested that an on-line computer-control (or pseudodynamic) method might be used to achieve the realism of *shaking table* testing with the economy and versatility of the conventional *quasi-static* approach. The pseudodynamic method is similar to conventional quasi-static tests except that the displacements imposed on a structure are determined by a computer during a test. The computation of the displacements depends on the dynamic characteristics of the structure and the progressive damage it suffers during the testing process.

In seismic response analysis, a structural system can be idealized by a discrete-parameter model in which all the system mass is lumped at a finite number of nodal points. The equations of motion of a discrete-parameter structural model are expressed by a family of second-order ordinary differential equations. The basic function of the pseudodynamic method is to solve these governing equations of motion by means of step-by-step numerical integration during the test. This method is, therefore, similar in concept to general dynamic-analysis computer programs. However, instead of using idealized mathematical models of structural components to obtain the linear or nonlinear force-deformation properties (stiffness) of a structure, the

pseudodynamic method uses direct experimental feedback. Displacement computations carried out during a test using direct numerical integration are based on the experimental feedback as well as numerically prescribed damping and inertia properties for the structure and a specified ground motion record. Consequently, dynamic effects are fully accounted for in the resulting displacement history. The displacements computed in each step are imposed on the test structure quasi-statically through hydraulic actuators. This is immediately followed by data acquisition; and the computation is repeated in the next step. As a result of this step-by-step procedure, the dynamic response of a structure to a digitized excitation record can be realistically simulated and monitored over a prolonged time span. A typical pseudodynamic test scheme is illustrated in Fig. 1.1.

## **1.2. Previous Research and Limitations**

The pseudodynamic method was initiated in Japan at the Institute of Industrial Science of the University of Tokyo and the Building Research Institute (BRI) of the Ministry of Construction [2-5]. Extensive experimental tests were carried out by Japanese researchers using the pseudodynamic method, from single-degree-of-freedom (SDOF) steel columns [3] to two- and three-story steel and reinforced concrete structures [5]. Test results correlated closely with analytical predictions. However, significant control problems were experienced in the testing of a seven-story reinforced concrete structure at BRI under the U.S.-Japan Cooperative Research Program [6]. The failure of the method in that multiple-degree-of-freedom (MDOF) stiff structure was attributed to inadequate instrumentation and the sensitivity of the system to small displacement-control errors.

Besides the above mentioned problem, the pseudodynamic method has not been fully verified. Modelling assumptions used in establishing the equations of motion may not realistically reflect the actual dynamic characteristics of a structure. For example, idealized lumped-mass and viscous-damping assumptions characterizing a test specimen are not realistic for a structure which has uniformly distributed mass and complex damping mechanisms. In addition,

since load is applied with a much slower rate in pseudodynamic testing than in an actual seismic response, strain-rate effects may be significant in some cases. The concentration of load application through hydraulic actuators can induce large local deformations or premature local failures in a structure. Approximations used in step-by-step integration procedures also introduce numerical errors. More significantly, various experimental errors may exist. These can seriously affect test reliability, and lead to numerical instability because of error-propagation characteristics of numerical integration algorithms. Some of these problems were addressed and studied recently by researchers at the University of California, Berkeley [7] and the University of Michigan, Ann Arbor [8,9]. The results of these studies confirmed the theoretical feasibility of the pseudodynamic method. However, the reliability and accuracy of the method still have to be verified through further analytical and experimental researches.

### 1.3. Numerical Formulation

As pseudodynamic results are obtained by solving the equations of motion for a structural system using step-by-step numerical integration, a typical numerical algorithm will be outlined in this section. Due to the experimental nature of the pseudodynamic procedure [1,10], explicit numerical algorithms are usually employed. The reasons for this will become clear in the following formulation. An *explicit* algorithm is one in which the displacement solution in an integration step is assumed to be a function of previous step solutions only. Otherwise, the algorithm is *implicit*. One of the most widely used explicit algorithms is the central difference method, currently used in pseudodynamic testing in Japan.

In a step-by-step integration process, dynamic equilibrium of a MDOF structural system is enforced only at discrete time intervals:

$$\mathbf{m} \mathbf{a}_i + \mathbf{c} \mathbf{v}_i + \mathbf{r}_i = \mathbf{f}_i \quad (1.1)$$

in which  $\mathbf{m}$  and  $\mathbf{c}$  are the mass and viscous-damping matrices of the structural system;  $\mathbf{a}_i$ ,  $\mathbf{v}_i$ , and  $\mathbf{r}_i$  are the acceleration, velocity, and restoring force vectors at time  $i\Delta t$ ; and  $\mathbf{f}_i$  is the



external excitation force vector. In this report, vector and matrix quantities are always represented by boldfaced variables, as in the above equation. The integration time step  $\Delta t$  is the interval at which response is computed. However, equilibrium is usually not satisfied between any two consecutive steps,  $i$  and  $(i+1)$ . In the central difference method, velocity and displacement are approximated by the difference equations:

$$\mathbf{v}_i = \frac{\mathbf{d}_{i+1} - \mathbf{d}_{i-1}}{2 \Delta t} \quad (1.2)$$

$$\mathbf{a}_i = \frac{\mathbf{d}_{i+1} - 2 \mathbf{d}_i + \mathbf{d}_{i-1}}{\Delta t^2}$$

where  $\mathbf{d}_{i-1}$ ,  $\mathbf{d}_i$ , and  $\mathbf{d}_{i+1}$  are the displacements in three consecutive steps. By substituting Eq. (1.2) into Eq. (1.1), we can solve for the displacement response in each step as

$$\mathbf{d}_{i+1} = \left( \mathbf{m} + \frac{\Delta t}{2} \mathbf{c} \right)^{-1} \left[ \Delta t^2 (\mathbf{f}_i - \mathbf{r}_i) + \left( \frac{\Delta t}{2} \mathbf{c} - \mathbf{m} \right) \mathbf{d}_{i-1} + 2 \mathbf{m} \mathbf{d}_i \right] \quad (1.3)$$

Therefore, the numerical solution is only an approximation. In spite of this, the method is of sufficient accuracy if the step size  $\Delta t$  is small enough [1,12].

In a pseudodynamic test, the restoring force of the structure,  $\mathbf{r}_i$ , is measured in each step, rather than computed from a mathematical model as in conventional dynamic analysis. Assuming that mass is lumped at each degree of freedom of the structure, we have a diagonal mass matrix  $\mathbf{m}$ . With this information and a suitably selected damping matrix  $\mathbf{c}$ , the displacement response can be easily calculated by means of Eq. (1.3). Thus, the pseudodynamic method is a rational approach with both theoretical and numerical bases.

Although the central difference method has desirable numerical properties (stability and accuracy), its applicability in pseudodynamic testing is still not justified. It is not known whether the numerical algorithm will remain stable and accurate under experimental conditions where errors are numerous. The reliability of this algorithm is only proved for purely analytical applications. However, experimental errors can be many times greater than any error that is

introduced by numerical operations in a digital computer. Therefore, the effects of experimental errors have to be investigated. To be more specific, the feedback of  $r_i$  is subjected to errors because computed displacements can never be exactly imposed on a structure. The degree of discrepancy depends on the accuracy of displacement controlling devices. Experience in Japan favors the use of the computed rather than the measured displacements in Eq. (1.3), while restoring forces can only be obtained experimentally. No rational explanation is yet available to support this choice. In any case, the errors in  $r_i$  have a significant consequence. In addition, the testing of a stiff MDOF system presents a serious problem, because the force feedback in this kind of system is very sensitive to small displacement discrepancies [6]. All these problems will be studied in the rest of this report.

#### 1.4. Error Propagation Effect

The adverse effect of experimental errors in pseudodynamic testing can be visualized with the help of some intuitive considerations. Errors are introduced in each step of the loading process during a pseudodynamic test. As will be examined in more detail in the next chapter, these errors may be caused by noises in electronic instruments, loss of significance in analog to digital conversions, the resolution and accuracy limitations of measurement and control instruments, and so on. The magnitudes of these errors depend on the instruments used, the ranges for which the measurement instruments are calibrated, the features of the electronic system, and the overall design of the experiment. These errors will persist no matter how good the instruments are, and how well the experiment is performed, although a careful setup and good instrumentation can greatly reduce their magnitudes.

In a pseudodynamic test, the displacement history of a structure advances in a discrete, incremental manner through direct numerical integration. An actual test may involve hundreds or thousands of numerical time steps. The displacement increment in each step depends on the feedback from the previous ones. Therefore, the errors introduced at each of these steps have a cumulative effect and are carried over to subsequent computations. Consequently, even though

a test is so designed that these errors are relatively small within each step, the result can still be unreliable because of cumulation or propagation of errors.

### 1.5. Objectives and Scope

The main objective of this report is to study the propagation characteristics of experimental errors in pseudodynamic testing, and to investigate possible improvement methods. Various numerical algorithms are compared in terms of their error-propagation behaviors. These algorithms include the basic central difference method, the summed form of the central difference method, and the Newmark explicit method, which have been recommended for pseudodynamic testing in previous studies [7,8,10]. The work reported here offers a better insight into the problems of the pseudodynamic test method, and reveals some useful guidelines for more reliable and successful testing. The goals of this study can be summarized as:

- (i) identifying the sources and effects of different error types, such that they can be avoided or minimized in future experiments;
- (ii) identifying more desirable numerical algorithms and implementation schemes to minimize the experimental error-propagation effects;
- (iii) deriving analytical methods for predicting cumulative error bounds, such that error tolerance limits and the reliability of test results can be assessed;
- (iv) analyzing additional problems in MDOF testing, and developing methods of improving stability and accuracy under adverse experimental conditions;
- (v) assessing the reliability of testing inelastic structures, which is the main application of the pseudodynamic method, and establishing criteria to ensure good test results.

In this report, we will not consider other inaccuracies, such as those caused by improperly prescribed dynamic characteristics of a test specimen, and the approximations used in the numerical algorithms. These problems have been examined in previous studies [1], and they are assumed to be not existing here. The design of a stable and accurate displacement-control

system, which is investigated by other researchers [9], is beyond the scope of this study. However, the adverse error-propagation effects of the displacement-control errors are included as part of the above objectives.

The contents of this report are arranged in the following order. In Chapter 2, we first discuss the sources and types of experimental errors as well as their physical effects. Furthermore, consistent mathematical expressions of these errors are established to serve as the basis for subsequent mathematical developments. In Chapter 3, equations governing error propagation in the step-by-step numerical algorithms are derived for the case of linear elastic SDOF systems, and comparisons are made among the different numerical methods. In Chapter 4, upper bounds of cumulative displacement errors are established, and the effects of integration step size and of different error types on error propagation are studied. In Chapter 5, the error analysis is extended to MDOF systems. Additional problems are identified and suggestions are provided for MDOF testing. In Chapter 6, we investigate error propagation in inelastic systems by means of numerical simulations and parametric studies. In Chapter 7, two numerical methods are proposed to compensate for the experimental error effects, and to improve the stability and accuracy of MDOF testing. Finally, general conclusions are drawn in Chapter 8, regarding error propagation, experimental precautions, error checking and compensation procedures, and the reliability of the pseudodynamic method.

## CHAPTER 2

### EXPERIMENTAL ERRORS

#### 2.1. Classification and General Expressions

Errors are inevitable in every experiment, no matter how carefully it is designed and performed. Experimental results are usually acceptable if errors introduced during experiments are reasonably small. In a pseudodynamic test, however, experimental feedback is used in the step-by-step numerical integration. Errors introduced in any step are carried over to subsequent computations. Consequently, the instantaneous numerical result in any step depends on the accuracy of the feedback from every previous step during an experiment. Due to this cumulative effect and the large number of computation steps involved, a test result may diverge significantly from the correct result as an experiment proceeds, even though errors introduced within a step are relatively small. The rate of error propagation in an experiment depends on the numerical scheme used and the nature of these errors. Therefore, before going into detailed analytical evaluation of the error-propagation problem, it is helpful to identify the sources as well as the nature of the errors which may be introduced into pseudodynamic experiments, and to formulate them in consistent mathematical expressions.

The errors discussed herein will be restricted to those introduced in the experimental environment. Errors of other sources are assumed to be insignificant and will not be considered in this study; these include numerical errors of integration algorithms and errors in the idealization of test specimens.

In each step of a displacement increment in a pseudodynamic test, errors can be introduced during the control and feedback processes as shown in Fig. 2.1. The displacement computed in any step  $i$ ,  $\bar{d}_i$ , may not be accurately imposed on the structure due to displacement control errors  $e_i^{dk}$ . In addition, the actually imposed displacement and the restoring force developed by the structure may be incorrectly measured and returned to the computer with errors  $e_i^{dm}$  and  $e_i^{rm}$ , respectively. These *control* and *measurement* errors amount to the total *feedback* errors introduced in each step. The error amplification effect can be observed from the

fact that incorrect displacements will result in erroneous restoring-force feedback, and that errors in restoring forces will lead to incorrect displacements being computed and imposed in the next step.

Experimental errors come from many sources. The control errors can be caused by: (i) inaccurate calibration of displacement transducers used in the closed-loop feedback system, which controls hydraulic actuators; (ii) resolution limits imposed by the analog-to-digital (A/D) conversion of control signals transferred by microprocessors; (iii) movement or deformation of specimen's supports; and (iv) lack of hydraulic actuator sensitivity to keep up the speed of displacement change. Similarly, the measurement errors can be caused by: (i) inaccurate measurement transducers; (ii) the A/D conversion of data transferred; (iii) electrical noises; and (iv) frictional forces in system connections. Consequently, the actual displacement- and force-feedback values are likely to deviate from the originally computed and expected quantities. All of these will be discussed in greater detail in the following section.

The control and feedback values in a MDOF pseudodynamic test can be related by the general expressions as

$$\hat{\mathbf{d}}_i = \bar{\mathbf{d}}_i + \mathbf{e}_i^d \quad (2.1)$$

$$\hat{\mathbf{r}}_i = \bar{\mathbf{r}}_i + \mathbf{e}_i^r \quad (2.2)$$

where  $\bar{\mathbf{d}}_i$  is the specified displacement vector determined by numerical computation in step  $i$ , and  $\bar{\mathbf{r}}_i$  is the restoring force that would be exerted by the test structure if  $\bar{\mathbf{d}}_i$  were imposed. The actual feedback values of these quantities are  $\hat{\mathbf{d}}_i$  and  $\hat{\mathbf{r}}_i$ , with feedback errors  $\mathbf{e}_i^d$  and  $\mathbf{e}_i^r$ , respectively. According to the definitions in Fig. 2.1, each of the error terms,  $\mathbf{e}_i^d$  and  $\mathbf{e}_i^r$ , consists of two contributing components:

$$\mathbf{e}_i^d = \mathbf{e}_i^{dc} + \mathbf{e}_i^{dm} \quad (2.3)$$

$$\mathbf{e}_i^r = \mathbf{k} \mathbf{e}_i^{dc} + \mathbf{e}_i^{rm} \quad (2.4)$$

in which  $\mathbf{k}$  is the elastic stiffness matrix of the structure.

As is the case with most experimental errors,  $\mathbf{e}_i^d$  and  $\mathbf{e}_i^f$  may consist of *systematic* and *random* parts. Systematic errors are those in which a regular pattern of occurrence can be identified. They are usually caused by persistent inaccuracy in instrumentation and experimental setup. The following discussions will show that these errors always tend to oscillate at the response frequency of the test structure during pseudodynamic experiments, and that they have a significant influence on experimental results. Fortunately, these errors can often be avoided or reduced to insignificant levels with careful instrumentation and test design. Random errors are more difficult to predict or control.

## 2.2. Systematic Errors

We will show in later chapters that systematic errors can impose a severe error-propagation problem on pseudodynamic testing. Some of these errors cause numerical instability in pseudodynamic tests. For this reason, several possible sources of the errors and their accompanying physical phenomena are discussed here. The physical phenomena illustrated will help to explain the analytical results presented later and to identify other systematic errors which might be present under various experimental conditions.

Systematic errors are usually due to inherent limitations of experimental equipment or persistent instrumental inaccuracies resulting from improper usage. Digital microprocessors, which are used to collect and transfer data during pseudodynamic experiments, can only store numbers with finite precisions; values smaller than their resolution limits are lost. No structural supports are perfectly rigid or fixed; therefore, structural deformation is usually influenced by support movement or deformation under applied load. In addition, restoring-force feedback is always affected by friction in the physical connections of a test structure to actuators and support apparatus. Significant systematic errors may also result from improper experimental techniques, such as mis-calibrations of control and measurement devices, and inadequate adjustment of servo controllers for the hydraulic actuators. However, most of these systematic errors

can be avoided or significantly reduced by an appropriate understanding of instrument limitations, a proper selection of test apparatus, and careful instrumentation.

These errors are usually well-defined and reproducible, so that some definite physical effects on experimental results can be observed. For simplicity, some of these effects will be described and illustrated here with a linear elastic SDOF model. Similar phenomena can be observed, however, in general MDOF systems.

In the following discussions, we assume that only one source of errors exists at a time. Furthermore, the discussions are based on a typical pseudodynamic displacement-control loop, as shown in Fig. 2.2. According to that, displacement is imposed in an incremental manner:

$$\Delta \bar{d}_i^* = \bar{d}_i - \hat{d}_{i-1} \quad (2.5)$$

and it is converted into a voltage signal before arriving at the *actuator controller*, which is responsible for the control of actuator displacement. If no experimental errors enter the control loop, then  $\hat{d}_{i-1}$  is equal to  $\bar{d}_{i-1}$ , and  $\Delta \bar{d}_i^*$  becomes  $\Delta \bar{d}_i$ . In Fig. 2.2,  $C_d$ ,  $C_r$ , and  $C_f$  are the calibration factors for measurement and control devices. The *SPAN* adjustment option in the controller can scale down the voltage excitation received by the controller. The *SPAN* is always equal to or less than one, and  $C_f$  should be equal to  $C_d \times \text{SPAN}$  under normal circumstances.

#### (i) Transducer Calibration Errors

Linear potentiometers (displacement transducers) are used to monitor structural displacements imposed by hydraulic actuators during pseudodynamic testing. The restoring forces developed by the structure are measured with load cells (load transducers) mounted on the actuators. The displacement and force variations are indicated by the corresponding voltage changes in the transducers. Therefore, the transducers need to be calibrated in order to convert the output voltage into appropriate physical units (e.g. inches, kips). The calibration factors for the transducers,  $C_r$  (force units/volt) or  $C_d$  (displ. units/volt), are usually obtained by a least square linear fit through a number of scattered points experimentally acquired for relating physical values to measured voltage.



The deviation of these points from the least square fit in a typical calibration depends on: the qualities of the instruments and supporting electronics; the precision used in installing the instruments; and the care taken in designing their attachments. Generally, most displacement and force transducers will exhibit a limited degree of nonlinearity. This error can be minimized by using high quality instruments, and by proper calibration. For example, calibration of transducers over the expected range of test response rather than over their entire useful range can substantially reduce the apparent nonlinearity of the instruments. In addition, by using time-stable signal conditioners, line voltage regulators, and careful temperature compensation (where needed), the desired transducer accuracy can usually be obtained.

The calibrations of the transducers are very susceptible to errors due in part to the lack of calibrated standards and to improper techniques. It is common to find instruments accurate to within 0.1%, while it may be difficult to calibrate them in place to within 1.0%. To illustrate the consequences of calibration errors, we will consider a simple case where the instruments and supporting apparatus are sufficiently accurate to give a linear relationship between input and output values. However, the coefficients  $C_r$  and  $C_d$  are inaccurately obtained, with small errors  $\pm\delta C_r$  and  $\pm\delta C_d$ , respectively.

By using the displacement control loop shown in Fig. 2.2 and the erroneous calibration factors to do voltage conversions, we can model the resulting control and measurement errors as

$$e_i^{dc} = -e_i^{dm} = \pm \frac{\delta C_d}{C_d} \bar{d}_i \quad (2.6)$$

$$e_i^{rm} = \pm \frac{\delta C_r}{C_r} k \bar{d}_i$$

such that the total feedback errors are

$$e_i^d = 0 \quad (2.7)$$

$$e_f = \left( \pm \frac{\delta C_r}{C_r} \pm \frac{\delta C_d}{C_d} \right) k \bar{d}_i$$

In deriving the above expressions, as shown in Appendix A, all the  $\delta C_d/C_d$  and  $\delta C_r/C_r$  terms with exponential orders greater than or equal to 2 are neglected. Furthermore, according to the fact that the specified displacement  $\bar{d}_i$  and the measured force  $\hat{f}_i$  constitute the force-displacement relationship perceived in numerical computations, we define an effective secant stiffness,  $\tilde{k}$ , for the structure as

$$\tilde{k} \bar{d}_i = \hat{f}_i \quad (2.8)$$

In this case,

$$\tilde{k} = \left( 1 \pm \frac{\delta C_r}{C_r} \pm \frac{\delta C_d}{C_d} \right) k \quad (2.9)$$

We can also note that  $\bar{d}_i$  is equal to  $\hat{d}_i$  here.

From Eq. (2.7), we observe that the variation of the errors  $e_f$  is either in-phase or 180 degrees out-of-phase with the computed displacement response  $\bar{d}_i$  depending on the sign of the total relative calibration errors. Eq. (2.9) indicates that mis-calibrations of the transducers can change the effective stiffness of a test specimen, and that the actual experimental result will correspond to the apparent stiffness  $\tilde{k}$  (see Fig. 2.3). This condition can be improved by a careful calibration procedure such that  $\delta C_d$  and  $\delta C_r$  will be relatively small.

However, we must also realize that recorded responses can still be in error due to transducer installation, even though the calibrations are accurate. In some types of load cells, errors can be induced by misalignment, which may introduce bending. If the misalignment is substantial or if the structure undergoes large deformations, the measured force may significantly differ from the component in the assumed direction of loading. These force errors can usually be corrected or minimized by careful design of the test setup. Displacement measurements can also suffer from misalignment problems and large deformation effects. In addition, certain

types of transducers (or means of attaching transducers to structures) produce hysteresis or other types of nonlinearity under displacement reversal. Again such errors in displacement can be minimized by careful design of the test apparatus.

(ii) *Actuator Displacement Calibration Errors*

Since displacements are measured in terms of voltage by the transducers, the displacement values computed by a computer must be converted into volts before being sent to the actuator controller. This conversion requires an actuator displacement-calibration factor  $C_j$  (actuator displ./volt). This factor may or may not be equal to the potentiometer calibration  $C_d$ , depending on how the controller modifies the incoming signal, i.e. the *SPAN* adjustment. In any case, it should be equal to  $C_d \times \text{SPAN}$  (see Fig. 2.2). Otherwise, errors will occur in the displacement control loop due to the inconsistency between the actuator and the displacement transducer calibrations. We now consider the case where only the actuator is mis-calibrated, and the transducer calibration is accurate. Assuming that  $C_j$  is off by  $\pm \delta C_j$ , and that displacement is imposed in an incremental manner, we have the control and measurement errors as

$$\begin{aligned} e_i^{dm} &= 0 \\ e_i^{dc} &= \pm \frac{\delta C_j}{C_j} \Delta \bar{d}_i \\ e_i^{rm} &= 0 \end{aligned} \tag{2.10}$$

Consequently, the total feedback errors are

$$\begin{aligned} e_i^{dt} &= \pm \frac{\delta C_j}{C_j} \Delta \bar{d}_i \\ e_i^f &= \pm \frac{\delta C_j}{C_j} k \Delta \bar{d}_i \end{aligned} \tag{2.11}$$

See derivations in Appendix A. Similarly, the effective stiffness (as defined in Eq. (2.8)) becomes

$$\tilde{k} = \left( 1. \pm \frac{\delta C_j}{C_j} \frac{\Delta \bar{d}_i}{\bar{d}_i} \right) k \quad (2.12)$$

Eq. (2.11) shows that the errors vary either in-phase or 180 degrees out-of-phase with the incremental displacement (or approximately the velocity response), depending on the sign of  $\delta C_j$ . The effective stiffness shown by Eq. (2.12) indicates that the apparent force-displacement relationship is not linear, and extra energy is either dissipated from or added into the response motion, depending on the sign of  $\delta C_j$ . These are illustrated in Fig. 2.4. This type of error can be easily observed during experiments by monitoring  $e_i^d$ , which should be extremely small and completely random in the absence of systematic errors. The magnitude of these errors depends on how the actuator displacement is calibrated. If it is done with the actual physical motion of the actuator, then the calibration factor is likely to be influenced by the overshooting or lagging-behind behavior of the actuator motion, which will be discussed later. Most often, it is better to compute  $C_j$  directly from  $C_d$ . Sometimes, a trial-and-error approach is required to achieve the best calibration result.

### (iii) Friction

Friction exists in most of the moving components of a pseudodynamic system, such as clevises which connect a test structure to hydraulic actuators and the base support, or the contact surfaces between the structure and its supporting apparatus. Friction can influence the restoring forces developed by structural deformations. Therefore, the forces measured by load cells are usually different from the actual restoring forces of a structure. If the frictional force in a SDOF system is assumed to be constant, then the force measurement errors can be modelled as

$$e_i^{fm} = f \frac{\Delta \bar{d}_i}{|\Delta \bar{d}_i|} \quad (2.13)$$

in which  $f$  represents a constant magnitude. Consequently, the total feedback errors become

$$e_i^f = e_i^{fm} = f \frac{\Delta \bar{d}_i}{|\Delta \bar{d}_i|} \quad (2.14)$$

In this case, the effective stiffness is

$$\tilde{k} = k + \frac{f}{d_i} \frac{\Delta \bar{d}_i}{|\Delta \bar{d}_i|} \quad (2.15)$$

These error effects are sketched in Fig. 2.5. The errors  $e_f^i$  due to a constant friction form a rectangular wave approximately in-phase with the velocity response, and have an energy-dissipation effect. Friction also exists in other structural connections, such as in the member joints. In that case, the friction contributes to realistic Coulomb damping in structural responses, and should not be considered as erroneous.

(iv) *Analog to Digital Conversion of Electrical Signals*

Floating-point displacement values evaluated by a computer are output in the form of digital voltage signals, which are converted by a programmable digital-to-analog (D/A) converter into analog voltage signals finally received by an actuator controller. Similarly, the analog voltages measured from displacement and load transducers are converted into a digital form by an A/D converter in the data acquisition system before being returned to the computer. In these A/D conversions, the fractional parts are either *truncated*, or *rounded-off* to the nearest digit. Most D/A or A/D converters have microprocessors that handle 8 to 16 bit words. If a D/A converter uses 12 bit words, then displacements can only be imposed in increments of  $1/2048$  ( $2/2^{12}$ ) times the maximum displacement for which the system is calibrated. While this is a rather small fractional error, the relative error can become significant when the specimen's displacements are small or when the displacement used to calibrate the system is substantially larger than the maximum displacement to be actually imposed. Assuming that the A/D conversions are carried out by truncation, and that the absolute values truncated in the control and feedback processes are  $t_i^{dc}$ ,  $t_i^{dm}$ , and  $t_i^{fm}$ , corresponding to those in displacement control, displacement measurement, and force measurement, respectively, we then have

$$e_f^{dc} = t_{i-1}^{dm} \frac{\hat{d}_{i-1}}{|\hat{d}_{i-1}|} - t_i^{dc} \frac{\Delta \bar{d}_i}{|\Delta \bar{d}_i|}$$

$$e_i^{dm} = - t_i^{dm} \frac{\hat{d}_i}{|\hat{d}_i|} \quad (2.16)$$

$$e_i^{rm} = - t_i^{rm} \frac{\hat{r}_i}{|\hat{r}_i|}$$

according to the incremental displacement approach. The resulting feedback errors are

$$e_i^d = t_{i-1}^{dm} \frac{\hat{d}_{i-1}}{|\hat{d}_{i-1}|} - t_i^{dc} \frac{\Delta \bar{d}_i}{|\Delta \bar{d}_i|} - t_i^{dm} \frac{\hat{d}_i}{|\hat{d}_i|} \quad (2.17)$$

$$e_i^f = k \left( t_{i-1}^{dm} \frac{\hat{d}_{i-1}}{|\hat{d}_{i-1}|} - t_i^{dc} \frac{\Delta \bar{d}_i}{|\Delta \bar{d}_i|} \right) - t_i^{rm} \frac{\hat{r}_i}{|\hat{r}_i|}$$

The signs of displacement control errors are determined by  $\Delta \bar{d}_i / |\Delta \bar{d}_i|$ , while those of measurement errors are determined by  $\hat{d}_i / |\hat{d}_i|$  and  $\hat{r}_i / |\hat{r}_i|$ . The magnitudes of these truncation errors are limited by

$$\begin{aligned} t_i^{dm} &< \frac{|d_{\max}|}{2^{m-1}} \\ t_i^{dc} &< \frac{|d_{\max}|}{2^{n-1}} \\ t_i^{rm} &< \frac{|r_{\max}|}{2^{m-1}} \end{aligned} \quad (2.18)$$

where  $n$  and  $m$  are the numbers of bits in a word used in the D/A and A/D converters respectively; and  $d_{\max}$  and  $r_{\max}$  are the maximum displacement and force calibrated for.

If  $t_i^{dm}$  and  $t_i^{rm}$  are negligibly small, then the error expressions can be simplified to

$$e_i^d = - t_i^{dc} \frac{\Delta \bar{d}_i}{|\Delta \bar{d}_i|} \quad (2.19)$$

$$e_i^f = - k t_i^{dc} \frac{\Delta \bar{d}_i}{|\Delta \bar{d}_i|}$$

and the effective stiffness becomes

$$\tilde{k} = \left( 1 - \frac{t_i^{dc}}{\bar{d}_i} \frac{\Delta \bar{d}_i}{|\Delta \bar{d}_i|} \right) k \quad (2.20)$$

Eqs. (2.19) and (2.20) are sketched in Fig. 2.6. Energy is added into response motion in this case. In general, this type of errors can be detected by monitoring  $e_i^d$ . If rounding-off is used instead of truncation, the maximum magnitudes of these errors are reduced by half. More importantly, the errors become random and the error-propagation effect is greatly reduced, as will be shown later.

#### (v) Support Movement

In the case of a cantilever structure subjected to a horizontal base excitation, lateral displacements imposed should be measured relative to a vertical reference line through the base of the structure. Experimentally, that may not be easy to do because of possible deformations or movements at the supports of the structure and of the reference frame. In a realistic sense, no support is perfectly rigid or fixed. This imperfection can prevent correct displacements to be imposed, and can subsequently alter the restoring-force feedback. Sometimes it is advantageous to monitor and control structural displacement relative to a stationary reference point instead of measuring the actuator piston movement internally. If this is the case, then the movement of the actuator support frame will not affect imposed displacements. However, such arrangements may adversely affect the stability of the hydraulic control system. The movement or deformation of a structural base support will tend to reduce the actual relative displacement imposed. For example, considering an idealized slip movement of the base support in the direction of load application, we can model the resulting displacement control and measurement errors as

$$e_i^{dc} = -d_s \frac{\hat{r}_i}{|\hat{r}_i|} \quad (2.21)$$

$$e_i^{dm} = -e_i^{dc}$$

The second equation is due to the fact that the displacement transducer will appear as if the correct structural displacement had been applied. The constant  $d_s$  is the amount of slip, which is assumed to occur only at load reversal. Consequently, the feedback errors are

$$e_i^d = 0 \quad (2.22)$$

$$e_i^f = -k d_s \frac{\hat{r}_i}{|\hat{r}_i|}$$

and the effective stiffness is

$$\bar{k} = \left( 1 - \frac{d_s}{d_i} \frac{\hat{r}_i}{|\hat{r}_i|} \right) k \quad (2.23)$$

Eqs. (2.22) and (2.23) are sketched in Fig. 2.7. We see that the effective stiffness is discontinuous at load reversal. No energy effect is observed. However, energy-dissipating hysteresis can happen if the base slip occurs gradually during the loading process. This is more likely to happen in reality. In addition, support deformation can increase the apparent flexibility of a structure without any energy effect, as long as this deformation remains elastic.

#### (vi) Inconsistent Actuator Motion

Hydraulic actuators may either react too slowly or be too sensitive to a voltage change during a displacement increment, depending on the *gain* control and the *servovalve* capacity. The gain control determines the system's speed to respond to a voltage change (either from the command signal or from a correction due to an error between the command and feedback signals). The maximum response speed is limited by the capacity of the servovalve. If the gain is low or the speed required is above the capacity of the servovalve, the hydraulic actuator will respond insensitively and fall behind the command signal. On the other hand, if the gain is too high, the actuator will overshoot and oscillate. If consistent overshooting or lagging-behind persists in a test, the effective force-displacement relationship will result in energy-dissipation or energy-addition type of hysteretic curves (see Fig. 2.8). Again, the errors in these cases can be



observed by monitoring  $e_i^d$ , which will show some systematic behavior if this situation occurs.

### 2.3. Random Errors

Random errors, like systematic errors, result from many causes. Random electrical noise in wires and electronic systems may slightly alter the electrical signals transferred during a test. Random rounding-off or truncation in the A/D conversion of electrical signals provides additional random errors. Furthermore, lagging-behind or overshooting of the actuator motion, as discussed before, may not be consistent from step to step. Instead, they may appear as random alternations. The supports of displacement transducers may not be secure enough, so that the transducer readings can be contaminated by some external mechanical disturbances. These are only a few possible causes. Random errors are so irregular that no specific physical effects can be anticipated.

### 2.4. Concluding Remarks

We have reviewed some possible sources of experimental errors as well as their nature and physical effects. Some idealized systematic errors are modelled in mathematical forms to reveal their effects on structural response computations. Similar physical phenomena can also be observed in other systematic errors, which can usually be identified easily. We can observe from the linear elastic SDOF model that systematic errors tend to be directly in-phase or 180 degrees out-of-phase with structural responses (displacement or velocity). The significance of such systematic effects can be observed from the stiffness influence or energy-changing hysteretic behavior. The response motion of a structure is very sensitive to these persistent stiffness and energy changing effects. In the case of random errors, no systematic physical effects can be inferred.

The magnitudes of these errors can be estimated from the properties of the instruments and electronic systems used, and also from the mechanical design of the experimental setup. Some errors can cancel one another (e.g. some dissipate energy and some add energy), while

others can reinforce one another. Most systematic errors can be detected during pseudo-dynamic experiments by monitoring the displacement-feedback errors  $e_i^d$ , or by the unusual energy change in the response motion.

## CHAPTER 3

### EVALUATION OF INTEGRATION ALGORITHMS BASED ON EXPERIMENTAL ERROR PROPAGATION

#### 3.1. Recursive Form of Integration Algorithms

To identify the basic error-propagation characteristics in pseudodynamic tests, we begin our studies with linear elastic SDOF systems. The step-by-step numerical integration algorithms, which are used to solve the equations of motion, will be expressed in a recursive matrix form. By introducing the experimental feedback errors into this recursive formula, we can arrive at a general error-propagation equation. This equation yields useful information regarding the characteristics of error cumulation in the numerical algorithms. Based on that equation, comparisons will be made among the different numerical methods which have been recommended for pseudodynamic application. This development also serves as a basis for more extensive error-propagation studies which are presented in the subsequent chapters.

The dynamic equilibrium of a SDOF system at time  $t = i \Delta t$  can be written as

$$m a_i + c v_i + r_i = f_i \quad (3.1)$$

where  $m$  is the system mass and  $c$  is the viscous damping coefficient;  $a_i$  and  $v_i$  are the acceleration and velocity responses at  $i \Delta t$ ; and  $r_i$  is the restoring force developed by system deformation. In a linear elastic system, we have

$$r_i = k d_i \quad (3.2)$$

in which  $k$  is the elastic stiffness and  $d_i$  is the corresponding displacement response. We can numerically solve Eq. (3.1) during pseudodynamic tests by means of the central difference method, which is formulated in Eq. (1.3) for general MDOF systems. For a SDOF system, the central difference method, as well as any other step-by-step integration algorithms, can also be expressed by a recursive matrix formulation [12,13] as

$$\mathbf{x}_{i+1} = \mathbf{D} \mathbf{x}_i - \mathbf{I} r_{i+\nu} + \mathbf{I} f_{i+\nu} \quad (3.3)$$

in which  $\mathbf{x}_i$  is the solution vector at  $t = i \Delta t$ . The solution vector contains the appropriate displacement, velocity, and/or acceleration terms, i.e.  $\mathbf{x}_i = \{d_i, v_i, a_i, d_{i-1}, \dots\}^T$ . The parameter  $\nu$  is an integer which is equal to either 0 or 1, depending on the specific numerical algorithm we are considering. Finally,  $\mathbf{D}$  and  $\mathbf{I}$  are the characteristic matrix and vector, respectively, of the specific numerical method. This recursive formula is not as efficient as Eq. (1.3) for numerical computations, but is convenient for formulating the error-propagation equation.

From Eq. (3.2), we can also express the restoring force in terms of the solution vector  $\mathbf{x}_i$  as

$$r_i = \mathbf{S} \mathbf{x}_i \quad (3.4)$$

where  $\mathbf{S}$  is a row matrix that depends on the contents of  $\mathbf{x}_i$  and the stiffness  $k$ . For example,  $\mathbf{S}$  is simply  $\{k, 0, 0\}$  if  $\mathbf{x}_i = \{d_i, v_i, a_i\}^T$ . Substituting Eq. (3.4) into Eq. (3.3), we have

$$\mathbf{x}_{i+1} = \mathbf{A} \mathbf{x}_i + \mathbf{L} f_{i+\nu} \quad (3.5a)$$

where

$$\mathbf{A} = \begin{cases} \mathbf{D} - \mathbf{I} \mathbf{S} & \text{if } \nu = 0 \\ (\mathbf{I} + \mathbf{I} \mathbf{S})^{-1} \mathbf{D} & \text{if } \nu = 1 \end{cases} \quad (3.5b)$$

and

$$\mathbf{L} = \begin{cases} \mathbf{I} & \text{if } \nu = 0 \\ (\mathbf{I} + \mathbf{I} \mathbf{S})^{-1} \mathbf{I} & \text{if } \nu = 1 \end{cases} \quad (3.5c)$$

Matrix  $\mathbf{A}$  is called the amplification matrix. Vector  $\mathbf{L}$  is the load operator, whereas  $\mathbf{I}$  is an identity matrix. The amplification matrix  $\mathbf{A}$  can be used to determine the stability and accuracy of an integration algorithm [12,13]. In addition, we will show that  $\mathbf{A}$  is related to the error-propagation characteristics of a numerical algorithm as well.

### 3.2. Error Cumulation Equation

The significance of experimental errors has been qualitatively discussed in Chapter 2. To gain a better understanding of the cumulative error growth in pseudodynamic experiments, we now formulate the error-propagation equation by introducing the feedback errors,  $e_i^d$  and  $e_i^f$ , discussed in Sec. 2.1 into Eq. (3.3), the recursive formulation of integration algorithms. From the force-feedback errors  $e_i^f$ , we define a new term:

$$e_i^{fd} = k^{-1} e_i^f \quad (3.6)$$

which is the amount of displacement error equivalent to  $e_i^f$ . Using this new error term, we can compare the propagations of displacement- and force-feedback errors more conveniently. Consequently, we can rewrite the control and feedback relationships in Eqs. (2.1) and (2.2) as

$$\hat{d}_i = \bar{d}_i + e_i^d \quad (3.7)$$

$$\hat{r}_i = k (\bar{d}_i + e_i^{fd}) \quad (3.8)$$

Before introducing the error terms into the recursive formula, we have to transform Eqs. (3.7) and (3.8) into a vector form compatible with the definition of  $\mathbf{x}_i$ . They become

$$\hat{\mathbf{x}}_i = \bar{\mathbf{x}}_i + \mathbf{e}_i^d \quad (3.9)$$

$$\hat{r}_i = \mathbf{S} (\bar{\mathbf{x}}_i + \mathbf{e}_i^{fd}) \quad (3.10)$$

in which  $\bar{\mathbf{x}}_i$  is the computed solution vector which contains  $\bar{d}_i$ ;  $\hat{\mathbf{x}}_i$  is the vector that contains the corresponding measured quantity  $\hat{d}_i$ ; and  $\mathbf{e}_i^d$  and  $\mathbf{e}_i^{fd}$  are the error vectors with elements  $e_i^d$  and  $e_i^{fd}$  in locations corresponding to that of  $\bar{d}_i$  in  $\bar{\mathbf{x}}_i$  and with zero values elsewhere. Now, assuming that both displacement- and force-feedback values are used in the computation of structural response during a pseudodynamic test, we replace  $\mathbf{x}_i$  and  $r_{i+\nu}$  in Eq. (3.3) by  $\hat{\mathbf{x}}_i$  and  $\hat{r}_{i+\nu}$ , respectively. As a result, the computed solution is no longer the true numerical solution. To indicate that, we also replace  $\mathbf{x}_{i+1}$  in Eq. (3.3) by  $\bar{\mathbf{x}}_{i+1}$ , assuming that  $\mathbf{x}_{i+1}$  represents the true

numerical solution without the influence of experimental errors. Finally, by substituting Eqs. (3.9) and (3.10) into Eq. (3.3), we have

$$\bar{\mathbf{x}}_{i+1} = \mathbf{D} (\bar{\mathbf{x}}_i + \mathbf{e}_i^d) - \mathbf{L} \mathbf{S} (\bar{\mathbf{x}}_{i+\nu} + \mathbf{e}_{i+\nu}^{rd}) + \mathbf{L} f_{i+\nu} \quad (3.11)$$

Following the subtraction of Eq. (3.3) from Eq. (3.11), we have

$$\bar{\mathbf{e}}_{i+1} = \mathbf{A} \bar{\mathbf{e}}_i + \mathbf{B} \mathbf{e}_i^d - \mathbf{L} \mathbf{S} \mathbf{e}_{i+\nu}^{rd} \quad (3.12a)$$

where

$$\bar{\mathbf{e}}_i = \bar{\mathbf{x}}_i - \mathbf{x}_i \quad (3.12b)$$

$$\mathbf{B} = \begin{cases} \mathbf{D} & \text{if } \nu=0 \\ \mathbf{A} & \text{if } \nu=1 \end{cases} \quad (3.12c)$$

Therefore,  $\bar{\mathbf{e}}_i$  is defined as the total cumulative error in the computed solution  $\bar{\mathbf{x}}_i$ . Correspondingly, there exists a cumulative displacement error:

$$\bar{e}_i = \bar{d}_i - d_i \quad (3.13)$$

which is an element of  $\bar{\mathbf{e}}_i$ .

By recursive substitutions of  $\bar{\mathbf{e}}_i$ 's in Eq. (3.12a) and assuming that  $\bar{\mathbf{e}}_{1-\nu}$  equals zero (i.e. no errors in the first step), cumulative errors can be expressed as

$$\bar{\mathbf{e}}_{n+1} = \sum_{i=1-\nu}^n \mathbf{A}^{n-i} \mathbf{B} \mathbf{e}_i^d - \sum_{i=1-\nu}^n \mathbf{A}^{n-i} \mathbf{L} \mathbf{S} \mathbf{e}_{i+\nu}^{rd} \quad (3.14)$$

The first term on the right hand side of the equation is the cumulative error due to displacement-feedback errors and the second term is due to force-feedback errors.

Note that if the computed solution  $\bar{\mathbf{x}}_i$  is used instead of the measured quantity  $\hat{\mathbf{x}}_i$  in the numerical computations, then we simply have

$$\bar{\mathbf{e}}_{n+1} = - \sum_{i=1-\nu}^n \mathbf{A}^{n-i} \mathbf{L} \mathbf{S} \mathbf{e}_{i+\nu}^{fd} \quad (3.15)$$

Eq. (3.14) is the matrix form of the error-propagation equation. The total cumulative errors can be calculated if the error vectors  $\mathbf{e}_i^{fd}$  and  $\mathbf{e}_i^{fd}$  are known. However, this equation is not very informative. The computation involved to obtain  $\bar{\mathbf{e}}_i$  is tedious. Therefore, we will further simplify Eq. (3.14) in the following section.

### 3.3. Cumulative Displacement Errors

Before acquiring a more useful equation of cumulative displacement errors from Eq. (3.14), we shall review the following mathematical relations.

If a matrix  $\mathbf{A}$  has dimensions  $N \times N$  and  $N$  distinct eigenvalues,  $\lambda_1, \lambda_2, \lambda_3, \dots$ , and  $\lambda_N$ , then there exists a diagonal matrix  $\mathbf{J}$  such that

$$\mathbf{J}^n = \Phi^{-1} \mathbf{A}^n \Phi \quad (3.16)$$

in which  $\Phi = [\phi_1, \phi_2, \dots, \phi_N]$  and  $\mathbf{J} = \text{diag}(\lambda_1, \lambda_2, \dots, \lambda_N)$ ; and  $\phi_i$  is an eigenvector of  $\mathbf{A}$ , corresponding to the eigenvalue  $\lambda_i$ . This similarity transformation is the property of an eigenvalue problem. Hence, for any  $N$ -dimensional vector  $\mathbf{y}_n$  which is defined as

$$\mathbf{y}_n = \mathbf{A}^n \mathbf{y}_0 \quad (3.17)$$

where  $\mathbf{A}$  satisfies the condition in Eq. (3.16), we can have the expression:

$$y_{nj} = c_{j1} \lambda_1^n + c_{j2} \lambda_2^n + \dots + c_{jN} \lambda_N^n \quad (3.18)$$

in which  $y_{nj}$  is the  $j$  th element of  $\mathbf{y}_n$ ; and  $c_{j1}, c_{j2}, \dots$ , and  $c_{jN}$  are constants determined by the eigenvectors of  $\mathbf{A}$  and the initial vector  $\mathbf{y}_0$ .

If  $f_{i+\nu}$  is equal to zero in Eq. (3.5a), the recursive formula represents the free-vibration response of a SDOF system. Furthermore, by letting  $i+1$  equal to  $n$  and performing recursive substitutions, we can transform Eq. (3.5a) into exactly the same form as Eq. (3.17). Therefore,

we can conclude that Eq. (3.18) should represent the numerical solution of a free-vibration response.

As will be seen in the next section when specific numerical algorithms are discussed, the amplification matrix  $\mathbf{A}$  is usually a  $2 \times 2$  or  $3 \times 3$  matrix. From Eq. (3.18), it is apparent that a numerical algorithm can produce a bounded oscillatory free-vibration response if two of the eigenvalues,  $\lambda_1$  and  $\lambda_2$ , are complex conjugates and  $|\lambda_3| < |\lambda_{1,2}| \leq 1$  (if  $\lambda_3$  exists at all). These are the stability conditions which can be met if  $\omega \Delta t$  is within a certain range; where  $\omega$  is the natural frequency of the structural system and is equal to  $\sqrt{k/m}$ . Assuming that these conditions are satisfied, we can represent  $\lambda_1$  and  $\lambda_2$  by

$$\lambda_{1,2} = A \pm i B = e^{(-\bar{\xi} \pm i) \bar{\Omega}} \quad (3.19)$$

where  $i = \sqrt{-1}$ . In this expression, the following relations are implied:

$$\bar{\xi} = - \frac{\ln (A^2 + B^2)}{2 \bar{\Omega}} \quad (3.20a)$$

$$\bar{\Omega} = \arctan \left( \frac{B}{A} \right) \quad (3.20b)$$

It is further defined that

$$\bar{\omega} = \frac{\bar{\Omega}}{\Delta t} \quad (3.20c)$$

By substituting Eqs. (3.19) and (3.20c) into Eq. (3.18) and assuming  $N = 3$ , we have

$$y_{nj} = e^{-\bar{\xi} \bar{\omega} \Delta t n} (c_{j1} \cos \bar{\omega} \Delta t n + c_{j2} \sin \bar{\omega} \Delta t n) + c_{j3} \lambda_3^n \quad (3.21)$$

The parameters in the above equation have some physical interpretations. Since Eq. (3.21) is a direct consequence of Eq. (3.18) and thus presents a free-vibration response,  $\bar{\xi}$  and  $\bar{\omega}$  are the apparent damping ratio and frequency of the response computed by a numerical algorithm. For this reason, these quantities are called the *numerical damping ratio* and *numerical frequency* of a



dynamic system, in contrast to the real dynamic properties of the system under a closed-form solution. As a matter of fact, they often serve as indicators of numerical accuracy. The third eigenvalue,  $\lambda_3$ , if it exists, is responsible for a spurious numerical solution, which will readily approach zero as  $n$  goes to infinity when  $|\lambda_3| < |\lambda_{1,2}| < 1$ . A more detailed discussion on this subject can be found in Reference 13. In our case, these results can be applied to the development of a simplified error-propagation equation.

Now, returning to the problem of error propagation, we apply the previous results into Eq. (3.14) by expanding it in the form of Eq. (3.21). In the expansion, we will only consider the cumulative displacement errors  $\bar{e}_i$  in vector  $\bar{\mathbf{e}}_i$ . As a result, we can have the following expression for cumulative displacement errors:

$$\bar{\mathbf{e}}_{n+1} = \sum_{i=1-\nu}^n \alpha_{ni} - \sum_{i=1-\nu}^n \beta_{ni} \quad (3.22a)$$

in which

$$\alpha_{ni} = e^{-\bar{\xi}\bar{\omega}\Delta t(n-i)} [a_{1i} \cos \bar{\omega}\Delta t(n-i) + a_{2i} \sin \bar{\omega}\Delta t(n-i)] + a_{3i} \lambda_3^{n-i} \quad (3.22b)$$

$$\beta_{ni} = e^{-\bar{\xi}\bar{\omega}\Delta t(n-i)} [b_{1i} \cos \bar{\omega}\Delta t(n-i) + b_{2i} \sin \bar{\omega}\Delta t(n-i)] + b_{3i} \lambda_3^{n-i} \quad (3.22c)$$

The constants  $a_{1i}$ ,  $a_{2i}$ ,  $a_{3i}$ ,  $b_{1i}$ ,  $b_{2i}$ , and  $b_{3i}$  can be determined by the values of  $\alpha_{ni}$ ,  $\alpha_{(i+1)i}$ ,  $\alpha_{(i+2)i}$ ,  $\beta_{ni}$ ,  $\beta_{(i+1)i}$ , and  $\beta_{(i+2)i}$ , respectively, which, in turn, can be computed from the equations:

$$\alpha_{ni} = \mathbf{A}^{n-i} \mathbf{B} \mathbf{e}_i^d \quad (3.23a)$$

$$\beta_{ni} = \mathbf{A}^{n-i} \mathbf{L} \mathbf{S} \mathbf{e}_{i+\nu}^d \quad (3.23b)$$

Eq. (3.22) is a general equation describing the cumulative displacement errors in an under-damped dynamic system. However, further simplification of the equation is possible when specific numerical methods are considered.

### 3.4. Error Propagation in the Explicit Numerical Algorithms

Three explicit numerical integration algorithms which are suitable for the pseudodynamic method will be compared here, based on the error-propagation properties, by using Eq. (3.22). They are the basic central difference method [10,12] which is currently used in Japan for pseudodynamic testing as discussed in Sec. 1.3, the Newmark explicit method [7,11], and the summed form of the central difference method [8,14]. These three methods are algebraically identical to one another. They are transformable to one another by algebraic manipulations, and have the same accuracy and stability properties (see Appendix B). However, their error-propagation characteristics can be different due to the different numerical formulations. In the following, the numerical formulations of the three explicit methods are illustrated to provide necessary information for the error studies. For simplicity, viscous damping is neglected in the equation of motion.

#### (i) Basic Central Difference Method

The algorithmic form for pseudodynamic computation is

$$d_{i+1} = 2 d_i - d_{i-1} + \frac{\Delta t^2}{m} (f_i - r_i) \quad (3.24)$$

and the corresponding recursive form is

$$\begin{Bmatrix} d_{i+1} \\ d_i \end{Bmatrix} = \begin{bmatrix} 2 & -1 \\ 1 & 0 \end{bmatrix} \begin{Bmatrix} d_i \\ d_{i-1} \end{Bmatrix} + \begin{Bmatrix} \Delta t^2/m \\ 0 \end{Bmatrix} (f_i - r_i) \quad (3.25)$$

#### (ii) Newmark Explicit Method

The algorithmic form for pseudodynamic computation is

$$d_{i+1} = d_i + \Delta t v_i + \frac{\Delta t^2}{2} a_i$$
$$a_{i+1} = \frac{1}{m} (f_{i+1} - r_{i+1}) \quad (3.26)$$

$$v_{i+1} = v_i + \frac{\Delta t}{2} (a_i + a_{i+1})$$

and the corresponding recursive form is

$$\begin{Bmatrix} d_{i+1} \\ v_{i+1} \\ a_{i+1} \end{Bmatrix} = \begin{bmatrix} 1 & \Delta t & \Delta t^2/2 \\ 0 & 1 & \Delta t/2 \\ 0 & 0 & 0 \end{bmatrix} \begin{Bmatrix} d_i \\ v_i \\ a_i \end{Bmatrix} + \begin{Bmatrix} 0 \\ \Delta t/2m \\ 1/m \end{Bmatrix} (f_{i+1} - r_{i+1}) \quad (3.27)$$

(iii) *Summed Form of the Central Difference Method*

The algorithmic form for pseudodynamic computation is

$$d_{i+1} = d_i + \Delta t z_i \quad (3.28)$$

$$z_{i+1} = z_i + \frac{\Delta t}{m} (f_{i+1} - r_{i+1})$$

and the corresponding recursive form is

$$\begin{Bmatrix} d_{i+1} \\ z_{i+1} \end{Bmatrix} = \begin{bmatrix} 1 & \Delta t \\ 0 & 1 \end{bmatrix} \begin{Bmatrix} d_i \\ z_i \end{Bmatrix} + \begin{Bmatrix} 0 \\ \Delta t/m \end{Bmatrix} (f_{i+1} - r_{i+1}) \quad (3.29)$$

From the recursive formulations above, we can readily identify for each method the characteristic matrices and vectors described in Eqs. (3.3) to (3.5). They are shown in Table 3.1. Although the amplification matrices,  $\mathbf{A}$ , are different among the three numerical methods, their eigenvalues are identical. The eigenvalues  $\lambda_{1,2}$  are equal to  $A \pm iB$ , with  $A = 1 - \omega^2 \Delta t^2/2$  and  $B = \sqrt{4 - (\omega^2 \Delta t^2 - 2)^2}/2$ . The eigenvalue  $\lambda_3$  is equal to zero in the Newmark Explicit method, and it does not exist in the other two. Consequently, the stability limit of the numerical methods is  $\omega \Delta t \leq 2$  (see Appendix B). Furthermore, the numerical damping ratios  $\bar{\xi}$  are equal to zero, according to Eq. (3.20). The parameters  $a_{1i}$ ,  $a_{2i}$ ,  $b_{1i}$ , and  $b_{2i}$ , in Eq. (3.22) can be obtained by means of Eq. (3.23), with the characteristic matrices and vectors in Table 3.1. These parameters are listed in Table 3.2. Substituting these parameters back into Eq. (3.22), we can simply express the cumulative displacement errors for all three

methods as

$$\bar{e}_{n+1} = C \sum_{i=1}^n e_i^d \sin (\bar{\omega} \Delta t (n-i) + \phi) + D \sum_{i=1}^n e_i^{fd} \sin \bar{\omega} \Delta t (n-i+1) \quad (3.30)$$

where  $C$  and  $D$  are error amplification factors. The parameters in the above equation are:

(i) *In the Basic Central Difference Method,*

$$\begin{aligned} C &= \frac{\sqrt{5-4A}}{B} \\ D &= \frac{2(A-1)}{B} \\ \phi &= \arctan \left( \frac{2B}{2A-1} \right) \end{aligned} \quad (3.31)$$

(ii) *In the Newmark Explicit & Summed-Form Central Difference Methods,*

$$\begin{aligned} C &= -\frac{\sqrt{2(1-A)}}{B} \\ D &= \frac{2(A-1)}{B} \\ \phi &= -\arctan \left( \frac{B}{1-A} \right) \end{aligned} \quad (3.32)$$

A sample derivation of Eq. (3.30) for the basic central difference method is shown in Appendix C.

### 3.5. Comparisons and Comments

Eq. (3.30) indicates how cumulative displacement errors propagate in the three different numerical methods. The first term on the right hand side stands for the cumulative errors due to displacement-feedback errors, and the second term is due to force-feedback errors. By

observing Eqs. (3.31) and (3.32), we can conclude that the Newmark explicit method and the summed form of the central difference method have exactly the same error-propagation properties, while the basic central difference method has a different amplification factor  $C$ . Amplification factor  $D$  is the same for all three methods. Therefore, force-feedback errors have similar effects in these numerical algorithms.

Some error-propagation characteristics can be revealed by studying the variations of amplification factors  $C$  and  $D$  with respect to  $\omega\Delta t$ . From Eqs. (3.31) and (3.32), the absolute values of  $C$  and  $D$  are plotted against  $\omega\Delta t$  in Fig. 3.1 for the three methods. We see that the basic central difference method is a poor scheme in terms of error propagation, because the value of  $|C|$  approaches infinity as  $\omega\Delta t$  goes to zero. This means that cumulative errors can be extremely large when  $\omega\Delta t$  is small. However, a small value of  $\omega\Delta t$  is favorable to numerical stability and accuracy (see Appendix B). Hence, good results are difficult to obtain with the basic central difference method because it is desirable to have numerical stability and accuracy on one hand, and small cumulative errors on the other. For the other two methods, this dilemma does not exist because both  $|C|$  and  $|D|$  diminish, with  $|D|$  at a faster rate, as the value of  $\omega\Delta t$  decreases.

However, the central difference method can be improved by using the computed displacement  $\bar{d}_i$  (rather than the measured displacement  $\hat{d}_i$ ) in the step-by-step computation. If this is the case, the error term containing  $e_i^{dl}$  disappears from Eq. (3.30). This is a significant reduction of cumulative errors when  $\omega\Delta t$  is very small. The use of the computed displacement may not be necessary for the other two methods, but it is still desirable to do so. One argument for proposing the use of the measured displacement is that this can preserve the actual constitutive property of the test specimen, because any error in displacement control can be offset by the corresponding error in force measurement. In reality, this is of no significance in the numerical computations. For example, we can consider the case when displacement control is the sole source of errors, so that  $e_i^{dl} = e_i^{rd} = e_i^{dc}$ , according to Eqs. (2.3), (2.4), and (3.6). By substituting these errors into Eq. (3.30), we can visualize that significant cancellation can occur only if

the factors  $C$  and  $D$  have similar magnitudes and opposite signs. However, according to Fig. 3.1, the magnitude of  $C$  is always several times larger than that of  $D$  whenever  $\omega\Delta t$  is small (from experience it is preferable to have  $\omega\Delta t < 0.5$  in order to achieve numerical accuracy, see Appendix B). Therefore, we can conclude that the use of the measured displacement  $\hat{d}_i$  has no numerical benefit; instead, it is more likely to aggravate the error-propagation problem.

Moreover, because of the existence of other error sources, the interaction of displacement- and force-feedback errors is unpredictable. By eliminating one source of inaccuracy, i.e. the displacement-feedback errors, we are always at a better position to obtain more accurate and predictable experimental results. For these reasons, the use of the computed displacement is recommended for all numerical methods discussed here. If this is the case, then the three methods will have identical error-propagation characteristics, because of the same amplification factor  $D$ . This is assumed in subsequent discussions. However, since the errors  $e_i^{fd}$  are partly contributed by  $e_i^d$ , one must still ensure that the control system is capable of limiting  $e_i^d$ 's to insignificant levels.

### 3.6. Numerical Examples

As an illustrative example, a pseudodynamic test is numerically simulated. Some truncation errors are generated in the simulation using the pseudodynamic testing facilities at Berkeley. Besides a mini-computer, the main testing facilities include a 12-bit word programmable D/A converter for sending analog displacement-control signals to an actuator controller, and a 14-bit word high speed data acquisition system (A/D converter) for collecting and returning the displacement and force measurements to the main computer. In this example, we calibrate the displacement transducer to a maximum range of 0.5 in., such that the D/A converter has a resolution limit of 0.5/2048 in. Displacement values smaller than that are truncated. The resolution limit of the data acquisition system is 0.5/8192 in. Therefore, truncation errors are mainly generated by the D/A converter.

A SDOF model with a period of 0.332 sec is simulated by a computer program to substitute for an actual test specimen. In each step, displacement is computed and sent directly to the data acquisition system through the D/A converter. Consequently, the displacement value returned from the data acquisition system will be slightly different from the computed one, due to the truncations and electrical noises occurring in the data transfer. The returned displacement value is then used to compute the restoring force of the specimen with the simulated stiffness. The computed restoring force and the displacement returned from the data acquisition system are subsequently used to compute the next displacement increment. This process is similar to a real pseudodynamic test, except that a mathematical model is used instead of a real specimen. This simulation has the advantage of eliminating other possible sources of errors which might occur in an actual test. As a result, experimental errors, which will occur mainly in the A/D conversion of displacement-control signals, can be described as  $e_i^d = e_i^{rd}$ .

With the above simulation model, we can obtain the cumulative errors resulting from the basic central difference method and the Newmark explicit method, as shown in Figs. 3.2 and 3.3, respectively. In both cases,  $\Delta t$  is 0.02 sec. Graph (a) of each figure shows the errors  $e_i^d$  (or  $e_i^{rd}$ ), which are obtained by subtracting the computed displacement values from the values returned from the data acquisition system. These errors consist of both random and systematic components. Graph (b) indicates the total cumulative errors  $\bar{e}_i$ , which are directly measured from the difference between the simulation result and the exact numerical solution. Graphs (c) and (d) plot the portions of the total cumulative errors due to  $e_i^d$  and  $e_i^{rd}$ , respectively. They are analytically computed by using Eq. (3.30), with the fact that  $e_i^d$  is equal to  $e_i^{rd}$ . It is apparent that the sum of the values in Graphs (c) and (d) is equal to the curve in Graph (b). This proves the validity of Eq. (3.30), which we mathematically derived. By comparing Graph (b) with Graph (d) in each figure, the advantage of using the computed displacement in the numerical procedure is clearly demonstrated. We can also see that the total cumulative displacement errors in Fig. 3.2 are larger than those in Fig. 3.3 because of the larger  $C$  factor in the basic central difference method.

A similar phenomenon is observed in another example with the same  $\omega$ , but a  $\Delta t$  of 0.01 sec. This should give us a better solution if no experimental error exists. The results obtained with the basic central difference and the Newmark explicit methods are plotted in Figs. 3.4 and 3.5, respectively. Graphs (b) and (c) in both figures show larger cumulative errors than the previous cases. This increase of cumulative error magnitudes can be explained by two facts. The growth of the amplification factor  $C$  with decreasing  $\omega\Delta t$  in the basic central difference method is one of the reason. The other fact is that doubling the number of integration steps doubles the number of input errors. This contributes to the larger cumulative errors in the Newmark explicit method, since the value of  $C$  declines slightly when  $\omega\Delta t$  is reduced. Therefore, the use of the measured displacement is highly undesirable. The cumulative errors in Graph (d) of each figure retain approximately the same magnitudes as before. This indicates that the cumulative errors due to force-feedback errors do not change significantly with step size. This phenomenon will be explained in the next chapter with an idealized model of systematic errors. It will also be shown that the cumulative errors due to force-feedback errors will diminish to zero as  $\omega\Delta t$  decreases if the errors  $e_i^{fd}$  are totally random.



## CHAPTER 4

### ERROR PROPAGATION CHARACTERISTICS IN SDOF LINEAR ELASTIC SYSTEMS

#### 4.1. General Cumulative Error Equation

As illustrated in Chapter 3, using the numerically computed displacement  $\bar{d}_i$  in the step-by-step integration can reduce cumulative error growth in pseudodynamic testing. The error-propagation studies in the following are based on this most desirable computational approach. Consequently, all three numerical methods discussed previously should have identical error-propagation properties; thus no specific method needs to be distinguished in our discussions herein. From Eq. (3.30), the general expression of cumulative displacement errors becomes

$$\bar{e}_{n+1} = D \sum_{i=1}^n e_i^{rd} \sin \bar{\omega} \Delta t (n-i+1) \quad (4.1)$$

in which the value of  $D$  can be determined by Eq. (3.31); and  $\bar{\omega}$  is the numerical natural frequency of a system, as represented by Eq. (3.20b). By returning to the derivation of the above equation in Chapter 3, a numerical analogy can be observed. Eq. (4.1) is developed from Eq. (3.12a), the recursive cumulative error equation, without the  $\mathbf{B} \mathbf{e}_i^{rd}$  term in it. With this term eliminated, Eq. (3.12a) has exactly the same formulation as Eq. (3.5a), which is a recursive numerical solution of the equation of motion. Therefore, the cumulative displacement errors represented by Eq. (4.1) can be considered as the displacement response of a structure to some error excitations  $e_i^r (= \mathbf{S} \mathbf{e}_i^{rd})$ . That becomes obvious if any error in the restoring force  $r_i$  is transferred to the right hand side of the equation of motion (Eq. (3.1)). The error term is then numerically equivalent to a force excitation in addition to  $f_i$ .

Since Eq. (3.12a) is true for any numerical algorithm which can be expressed in terms of Eq. (3.5a), the above analogy holds for any of the numerical methods we are considering. As a result, error-propagation characteristics depend more on the dynamic properties of a structural system than on the numerical method used. Besides that, the error-propagation behavior should be sensitive to the nature or the frequency content of errors  $e_i^{rd}$ , as a dynamic response

is to the frequencies of external excitations.

As mentioned in Chapter 2, two types of experimental errors exist: random and systematic. Systematic errors always tend to oscillate at the same frequency as the system response. If a system oscillates at its numerical natural frequency  $\bar{\omega}$ , a resonance-like effect can be created in error propagation. Resonance is a phenomenon during which the energy in the response motion of a system can grow without bound.

To identify the error-propagation characteristics, we now separately consider the different types of errors. The cumulative error growth due to random errors will first be investigated from a statistical approach. Systematic errors will be studied using an idealized sinusoidal error model. In reality, all experimental errors are composed of these idealized forms. Therefore, the results of these studies provide a realistic picture of error-propagation characteristics in pseudo-dynamic experiments. In addition, they can be used to assess the reliability of test results.

## 4.2. Random Errors

In general, a displacement drift and a symmetrical cumulative error growth can be identified from the results of random errors. The drift effect is usually caused by a constant offset in the error signals.

### 4.2.1. Drift Effect

Experimental errors of constant value can produce a displacement drift about the time axis of a displacement response history. That can be seen when  $e_i^{rd}$  in Eq. (4.1) is replaced by a constant  $e_c$ . If this is the case and  $\omega\Delta t$  is small, we can obtain from Eq. (4.1) the cumulative error expression:

$$\bar{e}_{n+1} \approx 2 e_c C \sin^2 \frac{1}{2} n \bar{\omega} \Delta t \quad (4.2)$$

in which the factor  $C$  is specified by Eq. (3.32). The magnitude of  $C$  is approximately equal to 1 when  $\omega\Delta t$  is small, as shown by Fig. 3.1b. This indicates that cumulative errors are only slightly amplified here (by a factor of 2). Therefore, drift effect is usually negligible when  $e_c$  is small. In reality,  $e_c$  can be a constant offset in random signals, such as a non-zero mean.

#### 4.2.2. Statistical Error Bound

Random errors can be described in terms of their statistical properties. It is reasonable to assume that these properties are invariant with time throughout a test, because they depend mainly on the test apparatus used. In the following studies, we assume that the random errors have a mean equal to zero and a standard deviation of  $S_e$ . We will not lose generality by the zero mean assumption. In general, any random errors are the sum of a random component which has a zero mean, and a constant which is equal to the total error mean. These two components can be treated separately, and their error-propagation behaviors can be superimposed on each other to give the total effect. That is true as long as the response is linear. The constant error produces a drift effect with a small error amplification factor, as discussed in the above section. Therefore, the constant component has no significant influence on the results presented here. Furthermore, we assume that the errors measured at different time steps of a single test are completely uncorrelated to one another. These properties lead to the following expressions:

$$E(e_i^{rd}) = 0$$

$$E(e_i^{rd}e_j^{rd}) = 0 \tag{4.3}$$

$$\text{VAR}(e_i^{rd}) = S_e^2$$

in which  $E(e_i^{rd})$  and  $\text{VAR}(e_i^{rd})$  are the mean (or expectation) and variance of random errors at step  $i$ ; and  $E(e_i^{rd}e_j^{rd})$  is the covariance when the mean is zero.

From Eq. (4.1) and the zero mean condition, the cumulative errors  $\bar{e}_{n+1}$  have a mean equal to zero also. This leads to the fact that  $\text{VAR}(\bar{e}_{n+1})$  is equal to  $E(\bar{e}_{n+1}^2)$ . Using this relation and the conditions in Eq. (4.3), we have the variance of  $\bar{e}_{n+1}$  as

$$\text{VAR}(\bar{e}_{n+1}) = D^2 S_e^2 \sum_{i=1}^n \sin^2 \bar{\omega} \Delta t (n-i+1) \quad (4.4)$$

Since variance is the square of standard deviation, the standard deviation of the cumulative errors is

$$S_{\bar{e}} = |D| S_e \sqrt{\frac{n}{2} - \frac{\sin \bar{\omega} \Delta t n \cos \bar{\omega} \Delta t (n+1)}{2 \sin \bar{\omega} \Delta t}} \quad (4.5)$$

in which the expression under the square root is the summation of the sine square functions in Eq. (4.4).

Since  $\bar{e}_{n+1}$  is a sum of  $n$  terms as shown in Eq. (4.1), and we are usually interested in  $n$  being very large,  $\bar{e}_{n+1}$  can be reasonably considered as a *normally distributed* random variable according to the *central limit theorem*. For a normally distributed random variable, over 95% of its values will be within two standard deviations from the mean. Therefore, we can safely estimate the upper cumulative error bound as

$$|\bar{e}_{n+1}| \leq S_{\bar{e}} J \quad (4.6a)$$

where

$$J = 2 |D| \sqrt{\frac{n}{2} - \frac{\sin \bar{\omega} \Delta t n \cos \bar{\omega} \Delta t (n+1)}{2 \sin \bar{\omega} \Delta t}} \quad (4.6b)$$

Fig. 4.1 shows the values of  $J$  with respect to  $n$  at various  $\omega \Delta t$  values. These are the maximum magnitudes of cumulative errors expected due to a unit standard deviation of random errors. The figure indicates that as  $\omega \Delta t$  increases, the rate of error growth with respect to  $n$  also increases. This rate tends to diminish as  $n$  becomes larger. To obtain more meaningful

information, we have to identify the influence of integration step size,  $\Delta t$ , in error propagation, while  $\omega$  is constant. Consider, for example, points A and B on the curves which have  $\omega\Delta t$  equal to 1 and 0.5, respectively, in Fig. 4.1. Assuming that  $\omega$  and  $t$ , which is the total time of analysis, are constant, we have  $\Delta t_A/\Delta t_B = 2$ , and  $t = 500 \Delta t_A$  or  $1000 \Delta t_B$ . If we go from A to B, the maximum cumulative error at time  $t$ ,  $|\bar{e}_t|_{\max}$ , is reduced by approximately 40%. Therefore, cutting the size of time step is an efficient way to improve accuracy.

More generally, we can show that cumulative errors can always be reduced by decreasing integration step size,  $\Delta t$ , and that the error bound will approach zero in the limit as  $\Delta t$  goes to zero. Letting  $\omega$  and  $t$  be constant as before, and substituting  $t/\Delta t$  for  $n$  in Eq. (4.6), we have

$$\frac{|\bar{e}_{n+1}|_{\max}}{S_v} = 4 \left[ \frac{\omega^2 t \Delta t}{8 - 2 \omega^2 \Delta t^2} - \frac{\sin \bar{\omega} t \cos \bar{\omega}(t+\Delta t)}{2 \left( \frac{4}{\omega^2 \Delta t^2} - 1 \right) \sin \bar{\omega} \Delta t} \right]^{1/2} \quad (4.7)$$

If  $\Delta t$  is small, we can obtain from this equation that

$$|\bar{e}_{n+1}|_{\max} = O(\Delta t^{1/2}) \quad (4.8)$$

This implies that both  $|\bar{e}_{n+1}|_{\max}$  and  $\Delta t$  will approach zero simultaneously.

#### 4.2.3. Example

To check the error-bound estimate in Eq. (4.6), we do a numerical simulation which is similar to the examples in Sec. 3.6. Instead of using truncation, we use rounding-off in the A/D conversion of displacement control signals, such that all the control errors will be random. The results of this simulation are displayed in Fig. 4.2. Fig. 4.2a shows the errors  $e_i^d$  measured during the simulation. These errors are equal to  $e_i^d$  as before. Fig. 4.2b shows the Fourier spectrum of the errors. The randomness of the error signals is illustrated by the approximately uniform frequency contributions in the spectrum. These errors have a standard deviation of  $0.1202 \times 10^{-2}$  in., and a mean of  $0.2581 \times 10^{-4}$  in. Therefore, our zero mean assumption is

valid. Finally, Fig. 4.2c shows the cumulative errors computed by Eq. (4.1) as well as the error bounds estimated by means of Eq. (4.6). The error-bound estimation is conservative.

### 4.3. Systematic Errors

#### 4.3.1. Sinusoidal Errors

From Sec. 2.2, we can observe that systematic errors  $e_i^r$  tend to oscillate at the response frequency of a structure in pseudodynamic testing. A resonance effect can be excited by this type of errors. To investigate the systematic error effect, we assume that errors  $e_i^{rd}$  can be represented by a simple sinusoidal function:

$$e_i^{rd} = A_c \sin \bar{\omega} \Delta t i \quad (4.9)$$

in which  $\bar{\omega}$  is any arbitrary frequency. By substituting this error form into Eq. (4.1), the cumulative errors become

$$\bar{e}_{n+1} = A_c D \sum_{i=1}^n \sin \bar{\omega} \Delta t \beta i \sin \bar{\omega} \Delta t (n-i+1) \quad (4.10)$$

in which  $\beta = \bar{\omega}/\omega$ . By means of trigonometric transformations, Eq. (4.10) can be written as

$$\bar{e}_{n+1} = \frac{1}{2} A_c D \left[ \frac{\sin \frac{1}{2} \bar{\omega} \Delta t (1+\beta) n \cos \frac{1}{2} \bar{\omega} \Delta t (1-\beta) (n+1)}{\sin \frac{1}{2} \bar{\omega} \Delta t (1+\beta)} - \frac{\sin \frac{1}{2} \bar{\omega} \Delta t (1-\beta) \cos \frac{1}{2} \bar{\omega} \Delta t (1+\beta) (n+1)}{\sin \frac{1}{2} \bar{\omega} \Delta t (1-\beta)} \right] \quad (4.11)$$

This equation can be simplified into the form:

$$\bar{e}_{n+1} = \frac{1}{2} A_c D [-\gamma \sin \bar{\omega} \Delta t (n+1) + \rho \sin \bar{\omega} \Delta t (n+1) \beta] \quad (4.12a)$$

in which

$$\gamma = \frac{\sin \bar{\omega} \Delta t \beta}{\cos \bar{\omega} \Delta t \beta - \cos \bar{\omega} \Delta t} \quad (4.12b)$$

$$\rho = \frac{\sin \bar{\omega} \Delta t}{\cos \bar{\omega} \Delta t \beta - \cos \bar{\omega} \Delta t}$$

This equation is similar to a numerical solution of an undamped displacement response of a structural system subjected to a sinusoidal excitation. As  $\beta$  approaches 1, both  $\gamma$  and  $\rho$  will go to infinity. This is the resonance phenomenon.

#### 4.3.2. Resonance Effect and Error Bound

To formulate the resonance phenomenon, we substitute  $\beta = 1$  into Eq. (4.11) and get

$$\bar{e}_{n+1} = -A_c R \sin(\bar{\omega} \Delta t n - \phi) \quad (4.13a)$$

where

$$R = \frac{1}{2} |D| \sqrt{n^2 + 2n + \frac{1}{B^2}} \quad (4.13b)$$

$$\phi = \arctan \left( \frac{n A}{\frac{1}{B} + n B} \right)$$

This is the equation of resonance response due to sinusoidal errors. Without damping, the cumulative errors can grow infinitely as  $n$  increases. It is, therefore, the maximum error-propagation effect which systematic errors can induce.

The resonance effect is not merely an idealistic conception. The response of a structure under earthquake excitations is, very often, dominated by its own natural frequency. Therefore, systematic errors always tend to have a frequency equal to  $\bar{\omega}$ . In addition, the natural frequency of a structure can be excited by the systematic errors themselves, even though when

the structure is not vibrating at that frequency. This is explained in the next section. For these reasons, we can expect the resonance effect to occur whenever input errors are systematic. Consequently, a reliable cumulative error bound can be obtained from Eq. (4.13) for systematic errors:

$$|\bar{e}_{n+1}| \leq A_c R \quad (4.14)$$

In Fig. 4.3, the factor  $R$  is plotted against  $n$  at different  $\omega\Delta t$  values. The curves are almost straight lines. We can also observe that the rate of cumulative error increase is more significant here than in the random error case (i.e.  $R \gg J$ ). In addition, from Eqs. (4.13b) and (4.14), we find that

$$\frac{|\bar{e}_{n+1}|_{\max}}{A_c} = \frac{1}{2} \sqrt{\omega^2 t^2 + 1} + O(\Delta t) \quad (4.15)$$

This error convergence equation is obtained in a similar way as Eq. (4.8). However, Eq. (4.15) shows that the cumulative errors due to systematic errors cannot be completely eliminated by reducing  $\Delta t$ . The cumulative error bound will approach a lower limit of  $A_c \sqrt{\omega^2 t^2 + 1} / 2$  as  $\Delta t$  becomes very small. Furthermore, reducing  $\Delta t$  cannot significantly improve the accuracy of a test result, because the  $O(\Delta t)$  term is small when compared with the square root term in Eq. (4.15). In other words,  $\Delta t$  has a negligible influence on the total cumulative errors. We can illustrate that by moving from point A to point B in Fig. 4.3, assuming  $\omega$  and  $t$  constant. In doing that, the cumulative errors are reduced by approximately 10% only, while a 40% reduction is achieved for random errors. This explains the observations from the numerical simulations in Sec. 3.6. Therefore, systematic errors are highly undesirable.



#### 4.4. General Errors of Mixed Form

##### 4.4.1. Fourier Transformation

In the previous discussions, we assume that errors are either random or of simple harmonic waveform. However, errors in an actual test are not that idealistic. They may consist of many different frequency contributions, such as the natural frequency of a structure and the frequencies of excitations. In addition, since systematic errors are always mixed with random errors, the systematic nature of real error signals may not be readily recognizable. In MDOF systems, the error signals can be even more complicated.

Despite this complexity, resonance phenomenon always dominates error propagation as long as systematic errors exist. To illustrate this fact, we will look at the problem from a more general view point. Errors of any form can be represented by a Fourier series. Since each term of a Fourier series is a simple harmonic function, the total cumulative errors in a test are the sum of all the simple harmonic contributions. The equations developed in the previous section for a sinusoidal error form can be individually applied to each of these terms.

We can re-write Eq. (4.12a), which is derived for sinusoidal errors, in the form as

$$\bar{e}_{n+1} = -A_e H \sin(\bar{\omega}\Delta t(n+1)\beta - \theta) \quad (4.16a)$$

where

$$H = \frac{1}{2} |D| \sqrt{\rho^2 + \gamma^2 - 2\rho\gamma \cos \phi}$$

$$\theta = \arctan \left( \frac{\gamma \sin \phi}{\rho - \gamma \cos \phi} \right) \quad (4.16b)$$

$$\phi = \bar{\omega}\Delta t (n + 1) (1 - \beta)$$

The parameters  $\gamma$  and  $\rho$  are defined in Eq. (4.12b).  $H$  is the amplification factor of the cumulative errors and it is a function of  $\omega\Delta t$ ,  $\beta$ , and  $n$ . In Fig. 4.4,  $H$  is plotted against  $n$  with different  $\beta$  values for an arbitrary case of  $\omega\Delta t = 0.30$ . We can see that  $H$  is an oscillatory function of  $n$ , and that its period and amplitude increase with increasing  $\beta$ . As  $\beta$  approaches 1,  $H$

tends to have infinitely large period and amplitude. It becomes the error amplification factor in the resonance phenomenon, i.e. the factor  $R$  in Eq. (4.13b). Fig. 4.4 also suggests that when the number of integration steps is large, only those sinusoidal errors with  $\beta$  close to unity are significant. The relative significance of other frequency components dies out fast in error propagation, when compared to that of resonance frequency.

To study the general error-propagation problem in terms of a Fourier series, we consider a complex error function:

$$e_m^{rd} = \cos \bar{\omega} \Delta t \beta_j m + i \sin \bar{\omega} \Delta t \beta_j m = e^{i \bar{\omega} \Delta t \beta_j m} \quad (4.17)$$

where  $\beta_j = \bar{\omega}_j / \bar{\omega}$  and  $i = \sqrt{-1}$ . From Eq. (4.16), the cumulative errors corresponding to the complex error function in the above equation are

$$\bar{e}_{n+1} = - H_j e^{i(\bar{\omega} \Delta t \beta_j (n+1) - \theta_j)} \quad (4.18)$$

in which  $H_j$  and  $\theta_j$  are the values of  $H$  and  $\theta$  in Eq. (4.16) when  $\beta$  is equal to  $\beta_j$ .

As a matter of fact, by discrete Fourier transformation, any sequence of error signals consisting of  $M$  points,  $e_0^{rd}$ ,  $e_1^{rd}$ , ..... and  $e_{M-1}^{rd}$ , can be interpolated by a trigonometric exponential polynomial [14,15]:

$$e_m^{rd} = \sum_{j=-k}^{k+\nu} c_j e^{ij \Delta \omega \Delta t m} \quad (4.19a)$$

in which

$$\begin{aligned} \nu = 0 \quad , \quad k = \frac{M-1}{2} \quad & \text{if } M \text{ is odd} \\ \nu = 1 \quad , \quad k = \frac{M-2}{2} \quad & \text{if } M \text{ is even} \end{aligned} \quad (4.19b)$$

$$\Delta \omega = \frac{2 \pi}{\Delta t M}$$

and  $c_j$ 's are the Fourier coefficients which can be computed by

$$c_j = \frac{1}{M} \sum_{m=0}^{M-1} e_m^{rd} e^{-ij\Delta\omega\Delta t m} \quad (4.19c)$$

Applying the results of Eqs. (4.17) and (4.18) into Eq. (4.19), we can express the cumulative errors by the series:

$$\bar{e}_{n+1} = - \sum_{j=-k}^{k+v} H_j c_j e^{j(\bar{\omega}\Delta t\beta_j(n+1)-\theta_j)} \quad (4.20)$$

where  $\beta_j = j\Delta\omega/\bar{\omega}$ . Since  $e_m^{rd}$ 's are real,  $c_j$  and  $c_{-j}$  must be complex conjugates. Consequently, assuming that  $M$  is odd, we can re-write Eqs. (4.19) and (4.20) as

$$e_m^{rd} = c_0 + 2 \sum_{j=1}^k |c_j| \sin(\bar{\omega}\Delta t\beta_j m + \psi_j) \quad (4.21)$$

and

$$\bar{e}_{n+1} = D c_0 \sum_{j=1}^n \sin \bar{\omega}\Delta t(n-j+1) - 2 \sum_{j=1}^k H_j |c_j| \sin(\bar{\omega}\Delta t(n+1)\beta_j - \theta_j + \psi_j) \quad (4.22)$$

where  $\psi_j = \arctan(-\text{Re}[c_j]/\text{Im}[c_j])$ . Eq. (4.21) shows that any experimental errors can be represented as the sum of a series of sinusoidal functions and a constant. Consequently, cumulative errors can be represented by a trigonometric series as well, as shown by Eq. (4.22). The first term on the right hand side of Eq. (4.22) is simply the cumulative errors due to a constant error  $c_0$ . It is negligible in most circumstances as discussed in Sec. 4.2.1. From Eq. (4.21), we can interpret that  $2 |c_j|$  is the amplitude of each contributing sinusoidal error component which has a frequency of  $j\Delta\omega$ . According to Fig. 4.4, most of the frequency components have negligible influences on error propagation. By neglecting these components, we can approximate the cumulative errors as

$$\bar{e}_{n+1} \approx - 2 \sum_j H_j |c_j| \sin(\bar{\omega}\Delta t(n+1)\beta_j - \theta_j + \psi_j) \quad (4.23)$$

in which we only include those frequency components that have  $\beta_j$ 's close to unity. If the input errors are dominated by the frequency  $\bar{\omega}$ , then the  $|c_j|$ 's should be larger in the neighborhood of  $\bar{\omega}$ . In that case, only a few frequencies need to be considered in Eq. (4.23).

#### 4.4.2. Implications of Fourier Spectrum

We can now generalize the error-propagation characteristics previously observed. By means of Fourier transformation, any errors can be represented by a series of trigonometric functions. For completely random errors, the magnitudes of these functions,  $|c_j|$ 's, are approximately uniform in the frequency spectrum (see Fig. 4.2). In addition, the  $|c_j|$ 's are relatively small when compared to the actual magnitude of the errors. Due to this fact, the resulting cumulative errors will be small, according to Eq. (4.23). We can also observe that cumulative errors will be dominated by the natural frequency  $\bar{\omega}$ , because the amplification factors  $H_j$  near that frequency are relatively large. This is consistent with our observations in Sec. 4.2.

However, in the presence of systematic errors, a large narrow spike will appear at  $\bar{\omega}$  in an error spectrum. This means that both the  $|c_j|$ 's and  $H_j$ 's are large when the  $\beta_j$ 's are close to 1. As a result, the cumulative errors due to systematic errors will be much larger than those due to random errors, according to Eq. (4.23). Since the spike is narrow, Eq. (4.23) will approximately give the same error bound as Eq. (4.13), by taking  $A_e \approx 2 \sum_j |c_j|$  and  $H_j \approx R$ . The existence of this narrow spike in an error spectrum can be explained as follows. Due to the resonance phenomenon, Eq. (4.23) represents a filter-like action which amplifies those frequencies near  $\bar{\omega}$  and suppresses the other frequencies. As a result, cumulative errors tend to be dominated by the natural frequency  $\bar{\omega}$ . These cumulative errors will, in turn, enhance the natural frequency in a structural response whether the response is dominated by that frequency or not. Since systematic errors tend to follow the structural response frequency, their frequency content will be enhanced with  $\bar{\omega}$  as well. Through that interaction, systematic errors always tend to be dominated by the frequency  $\bar{\omega}$ . Therefore, resonance is usually the predominant effect in error propagation, as long as systematic errors exist. This implies that the error

bound in Eq. (4.14), which assumes resonance condition, is realistic.

#### 4.4.3. Examples

To illustrate the above discussions, we use the same numerical example as in Sec. 4.2.3. In this case, truncation is used in the A/D conversion of displacement signals to produce systematic errors. The structural system has an angular frequency  $\omega$  of  $18.91 \text{ sec}^{-1}$ . By using  $\Delta t$  of  $0.02 \text{ sec}$ , the corresponding numerical frequency,  $\bar{\omega}$ , becomes  $19.02 \text{ sec}^{-1}$ , according to Eq. (3.20b). Since the maximum displacement calibrated for is  $5 \text{ in.}$  and a 12-bit programmable D/A converter is used, the maximum truncation error expected will be  $0.0024 \text{ in.}$

The results of the simulation are shown in Fig. 4.5. From Fig. 4.5a, we observe that the measured errors,  $e_j^d$ , are random, but with a systematic oscillatory trend. A spectral analysis is performed on these error signals, and the frequency spectrum is shown in Fig. 4.5b. The vertical axis of the spectrum represents the error amplitude,  $2 |c_j|$ , of each frequency component. Due to systematic truncations, a relatively large spike can be observed in the spectrum at frequency  $\bar{\omega}$ . Fig. 4.5c shows the resulting cumulative errors. They are significantly larger than those in Fig. 4.2 (by more than 10 times). The error bounds computed by means of Eq. (4.23) are also shown in Fig. 4.5c. They are very close to the actual error amplitudes. The error-bound computation, as shown in Table 4.1, uses only the two major frequency components indicated in Fig. 4.5b.

In another example,  $\Delta t$  of  $0.01 \text{ sec}$  is used instead. The numerical frequency  $\bar{\omega}$  becomes  $18.94 \text{ sec}^{-1}$ . The results are shown in Fig. 4.6. They are similar to those of the previous example. By comparing Fig. 4.5 with Fig. 4.6, we can see that reducing  $\Delta t$  has no obvious effect on error propagation at all. This is consistent with our error convergence equation (Eq. (4.15)).

In the above examples, due to the dominance of resonance phenomenon in error propagation, the error bounds can also be estimated by means of Eq. (4.14). Since the magnitudes of the above truncation errors are within the range of  $0$  to  $0.0024 \text{ in.}$ , we can take the mean value of  $0.0012 \text{ in.}$  as the error amplitude  $A_e$ . Substituting this value into Eq. (4.14), we obtain the

cumulative error bound for each case. They are also plotted in Figs. 4.5c and 4.6c, respectively. These error estimates are as satisfactory as those based on Fourier spectrum.

#### 4.5. Concluding Remarks

From the above studies, we can see that systematic errors are significantly worse than random errors in error propagation. The cumulative error bounds resulting from systematic errors are comparatively large and they cannot be reduced by decreasing  $\Delta t$ . In the case of random errors, cumulative errors are small and they will diminish as  $\Delta t$  goes to 0. The observations in this chapter can also be correlated with the energy effects of systematic errors observed in Sec. 2.2. The dynamic response of a structure is very sensitive to energy changes. If systematic errors of the energy-addition type exist, the response of a structure can grow without limit as resonance phenomenon. On the other hand, if input errors are energy dissipating, the response will be rapidly damped as if the structural system had a very high viscous damping. Therefore, systematic errors should be minimized by all means in pseudodynamic tests, such as replacing truncation by rounding-off in the A/D conversions of displacement and restoring force signals. As will be shown later, the energy adding errors are highly disastrous in MDOF testing.

Consequently, special precautions should be paid to the error sources discussed in Sec. 2.2, so that they will not detrimentally affect test results. In general, by knowing  $\omega$  and  $\Delta t$ , we can obtain cumulative error bounds using Eq. (4.6) or (4.14). From these, the tolerance limits of various errors can be set to ensure satisfactory test results; and the reliability of pseudodynamic testing can be assessed.

## CHAPTER 5

### ERROR PROPAGATION CHARACTERISTICS IN MDOF LINEAR ELASTIC SYSTEMS

#### 5.1. Cumulative Errors in MDOF Systems

As the number of structural degrees of freedom increases, more experimental errors are introduced into a pseudodynamic test. It is because control and measurement errors exist at each additional degree of freedom. Furthermore, the restoring force developed at each degree of freedom of a structure is influenced by displacement-control errors at all the others. This coupling effect can be observed from the off-diagonal elements of a stiffness matrix. The larger the off-diagonal elements are, the greater will be the extent of couplings. In addition, since the rate of error propagation is proportional to the  $\omega\Delta t$  value, the higher frequencies of a MDOF system will induce more significant cumulative errors. All these considerations lead to the conclusion that the error-propagation problem is more serious in MDOF systems than in the previous SDOF case. In this chapter, we will investigate the MDOF problem from a numerical point of view, using the results developed in Chapters 3 and 4 for SDOF systems. To do that, we first develop the error-propagation equation in MDOF systems by means of modal superposition.

##### 5.1.1. Modal Superposition Method

Modal superposition is a useful technique for MDOF analysis. It will be briefly reviewed here so that it can be applied to the error-propagation studies.

In a MDOF system, the equations of dynamic equilibrium at  $t = i \Delta t$  can be represented by the matrix equation:

$$\mathbf{m} \mathbf{a}_i + \mathbf{c} \mathbf{v}_i + \mathbf{r}_i = \mathbf{f}_i \quad (5.1)$$

where  $\mathbf{m}$  and  $\mathbf{c}$  are the mass and damping matrices of the system; and  $\mathbf{a}_i$ ,  $\mathbf{v}_i$ , and  $\mathbf{r}_i$  are the acceleration, velocity, and restoring force vectors due to the external excitation  $\mathbf{f}_i$ . In linear

elastic systems, the restoring force can be expressed as

$$\mathbf{r}_i = \mathbf{k} \mathbf{d}_i \quad (5.2)$$

in which  $\mathbf{k}$  is the elastic stiffness matrix, and  $\mathbf{d}_i$  is the displacement vector. From the above structural properties, we can define the eigenvector  $\boldsymbol{\phi}_m$  as any vector which satisfies  $\mathbf{k} \boldsymbol{\phi}_m = \omega_m^2 \mathbf{m} \boldsymbol{\phi}_m$ , where  $\omega_m^2$  is the corresponding eigenvalue. The  $\boldsymbol{\phi}_m$ 's and  $\omega_m$ 's can be physically interpreted as the undamped free-vibration mode shapes and frequencies of a MDOF structural system. For a  $N$ -degree-of-freedom system, we can always have a set of  $N$  linearly independent eigenvectors which satisfy the following orthogonality conditions [16]:

$$\boldsymbol{\phi}_m^T \mathbf{m} \boldsymbol{\phi}_n = 0 \quad (5.3a)$$

$$\boldsymbol{\phi}_m^T \mathbf{k} \boldsymbol{\phi}_n = 0 \quad (5.3b)$$

for  $m \neq n$ . In addition, with proper assumptions on the damping matrix  $\mathbf{c}$ , the eigenvectors can also be orthogonal with respect to damping:

$$\boldsymbol{\phi}_m^T \mathbf{c} \boldsymbol{\phi}_n = 0 \quad (5.3c)$$

From the above orthogonality conditions, the eigenvectors are linearly independent. Therefore, we can express system responses as linear combinations of the eigenvectors:

$$\mathbf{d}_i = \sum_{m=1}^N \boldsymbol{\phi}_m D_{mi} \quad (5.4a)$$

$$\mathbf{v}_i = \sum_{m=1}^N \boldsymbol{\phi}_m \dot{D}_{mi} \quad (5.4b)$$

$$\mathbf{a}_i = \sum_{m=1}^N \boldsymbol{\phi}_m \ddot{D}_{mi} \quad (5.4c)$$

By substituting these expressions into Eq. (5.1), and using the conditions in Eq. (5.3), we can obtain a system of  $N$  uncoupled equations of motion:



$$M_m \ddot{D}_{mi} + C_m \dot{D}_{mi} + K_m D_{mi} = F_{mi} \quad (5.5)$$

for  $m = 1, 2, \dots, N$ . These are the modal equilibrium equations, and  $D_{mi}$  is the modal displacement response in the *generalized* coordinates. Correspondingly,  $K_m$ ,  $M_m$ , and  $C_m$  are the generalized stiffness, mass, and damping, which can be obtained by

$$\begin{aligned} K_m &= \boldsymbol{\phi}_m^T \mathbf{k} \boldsymbol{\phi}_m \\ M_m &= \boldsymbol{\phi}_m^T \mathbf{m} \boldsymbol{\phi}_m \\ C_m &= \boldsymbol{\phi}_m^T \mathbf{c} \boldsymbol{\phi}_m \end{aligned} \quad (5.6)$$

Similarly, the modal restoring force and excitation are represented by

$$\begin{aligned} R_{mi} &= \boldsymbol{\phi}_m^T \mathbf{r}_i = K_m D_{mi} \\ F_{mi} &= \boldsymbol{\phi}_m^T \mathbf{f}_i \end{aligned} \quad (5.7)$$

From Eq. (5.6), and the definition of the eigenvectors and eigenvalues, we know that  $\omega_m$  is equal to  $(K_m/M_m)^{1/2}$ , which is the frequency of the vibration mode  $m$ . Consequently, a  $N$ -degree-of-freedom system has  $N$  vibration modes with frequencies:  $\omega_1, \omega_2, \dots$ , and  $\omega_N$ . Furthermore, according to Eq. (5.4), the dynamic responses of a  $N$ -degree-of-freedom system are linear combinations of the  $N$  uncoupled modal responses, which are governed by Eq. (5.5). The step-by-step numerical integration, which is used to solve Eq. (5.1) in a pseudodynamic test, can be similarly applied to Eq. (5.5) for each individual mode. Therefore, instead of direct numerical computation, the solution of Eq. (5.1) can be equivalently obtained by superimposing the individual modal solutions.

### 5.1.2. Cumulative Errors by Modal Superposition

Using the modal superposition method, error-propagation behavior in MDOF systems can be formulated from the results of SDOF systems. Similar to system responses, the total cumulative errors in MDOF systems can be considered as a linear combination of all the modal cumulative errors. Consequently, the error-propagation problem here is equivalent to a set of uncoupled SDOF cases.

In MDOF systems, the displacement- and force-feedback errors can be represented by error vectors  $\mathbf{e}_i^d$  and  $\mathbf{e}_i^f$ , respectively. Similar to Eq. (3.6), we can also define the equivalent displacement error  $\mathbf{e}_i^{rd}$  as  $\mathbf{k}^{-1} \mathbf{e}_i^f$ . To use the modal superposition approach, we must first express these errors in their corresponding modal forms. According to the development in the previous section, the modal errors can be obtained by the following transformations:

$$E_{mi}^d = \frac{1}{M_m} \boldsymbol{\phi}_m^T \mathbf{m} \mathbf{e}_i^d \quad (5.8a)$$

$$E_{mi}^r = \boldsymbol{\phi}_m^T \mathbf{e}_i^f \quad (5.8b)$$

$$E_{mi}^{rd} = K_m^{-1} E_{mi}^r \quad (5.8c)$$

where  $E_{mi}^d$ ,  $E_{mi}^r$ , and  $E_{mi}^{rd}$  are the corresponding modal forms of  $\mathbf{e}_i^d$ ,  $\mathbf{e}_i^f$ , and  $\mathbf{e}_i^{rd}$ , respectively. By substituting  $E_{mi}^{rd}$  for  $\mathbf{e}_i^{rd}$  in Eq. (4.1), we obtain the cumulative error equation for each individual mode as

$$\bar{E}_{m(n+1)} = D_m \sum_{i=1}^n E_{mi}^{rd} \sin \bar{\omega}_m \Delta t (n-i+1) \quad (5.9)$$

in which  $D_m$  and  $\bar{\omega}_m$  are the values of  $D$  and  $\bar{\omega}$  when  $\omega$  is equal to  $\omega_m$  in Eq. (3.31). According to Eq. (5.4a), the total cumulative errors in the *geometric* coordinates can be obtained by

$$\bar{\mathbf{e}}_{n+1} = \sum_{m=1}^N \boldsymbol{\phi}_m \bar{E}_{m(n+1)} \quad (5.10)$$

By substituting Eq. (5.9) into Eq. (5.10), and using the results of Eqs. (5.8b) and (5.8c), we have

$$\bar{\mathbf{e}}_{n+1} = \sum_{m=1}^N D_m \mathbf{F}_m \sum_{i=1}^n \mathbf{e}_i^{rd} \sin \bar{\omega}_m \Delta t (n-i+1) \quad (5.11a)$$

in which

$$\mathbf{F}_m = \frac{\boldsymbol{\phi}_m \boldsymbol{\phi}_m^T \mathbf{k}}{\boldsymbol{\phi}_m^T \mathbf{k} \boldsymbol{\phi}_m} \quad (5.11b)$$

This is the equation of cumulative displacement errors in MDOF systems. It is similar to Eq. (4.1), except that the cumulative error vector here is a linear combination of all the modal contributions. By means of Eq. (5.11), we can study the general error-propagation characteristics in MDOF testing.

## 5.2. Random Errors

### 5.2.1. Preliminary Considerations

To study the propagation of random errors in MDOF testing, a statistical approach similar to that in Sec. 4.2.2 is used. The statistical properties of the errors  $\mathbf{e}_i^{rd}$  are similar to those of the SDOF case, although some additional assumptions are required to simplify the problem. The errors have a zero mean at each degree of freedom, and a uniform standard deviation of  $S_e$ . In addition, we assume that the errors at each degree of freedom are completely uncorrelated to one another, and to those at any other degrees of freedom. These properties can be mathematically expressed as

$$\begin{aligned} E(\mathbf{e}_i^{rd}) &= 0 \\ E(\mathbf{e}_i^{rd} \mathbf{e}_j^{rd T}) &= 0 \end{aligned} \quad (5.12)$$

$$E(\mathbf{e}_i^{rd} \mathbf{e}_j^{rd T}) = S_e^2 \mathbf{I}$$

for  $i \neq j$ . In the above equations, 0 is a zero vector or matrix, and  $\mathbf{I}$  is an identity matrix.

For simplicity, we also assume that the structural system considered has a uniform mass distribution:

$$\mathbf{m} = \hat{m} \mathbf{I} \quad (5.13)$$

where  $\hat{m}$  is the mass lumped at each degree of freedom. Furthermore, the eigenvectors of the system are normalized such that

$$\boldsymbol{\phi}_m^T \boldsymbol{\phi}_m = 1 \quad (5.14)$$

for  $m = 1, 2, \dots, N$ .

With these assumptions, the cumulative error bound at each degree of freedom can be individually estimated using the same statistical criterion as before, i.e. the magnitude of cumulative errors is most probably within twice their standard deviation from the mean. The variance and the standard deviation of cumulative errors at each degree of freedom can be obtained from Eq. (5.11). To assist matrix operations, we define the following vector notations. For any arbitrary vector  $\mathbf{x}$ , which is  $\{x_1, x_2, \dots, x_m\}^T$ , we define

$$\begin{aligned} \sqrt{\mathbf{x}} &= \{x_1^{1/2}, x_2^{1/2}, \dots, x_m^{1/2}\}^T \\ \{\mathbf{x}\}^2 &= \{x_1^2, x_2^2, \dots, x_m^2\}^T \\ |\mathbf{x}| &= \{|x_1|, |x_2|, \dots, |x_m|\}^T \end{aligned} \quad (5.15)$$

### 5.2.2. Statistical Error Bounds

From Eq. (5.11), we have the product of the cumulative error vector and its transpose as

$$\begin{aligned} \bar{\mathbf{e}}_{n+1} \bar{\mathbf{e}}_{n+1}^T &= \sum_{m=1}^N \sum_{p=1}^N D_m D_p \mathbf{F}_m \\ &\times \left[ \sum_{i=1}^n \sum_{j=1}^n \mathbf{e}_i^{td} \mathbf{e}_j^{td T} \sin \bar{\omega}_m \Delta t (n-i+1) \sin \bar{\omega}_p \Delta t (n-j+1) \right] \mathbf{F}_p^T \end{aligned} \quad (5.16)$$

By applying the statistical properties described in Eq. (5.12), we can obtain from Eq. (5.16) a matrix average:

$$E(\bar{\mathbf{e}}_{n+1} \bar{\mathbf{e}}_{n+1}^T) = S_e^2 \sum_{m=1}^N \sum_{p=1}^N D_m D_p \mathbf{F}_m \mathbf{F}_p^T \sum_{i=1}^n \sin \bar{\omega}_m \Delta t (n-i+1) \sin \bar{\omega}_p \Delta t (n-i+1) \quad (5.17)$$

The above equation can be further simplified to

$$E(\bar{\mathbf{e}}_{n+1} \bar{\mathbf{e}}_{n+1}^T) = S_e^2 \sum_{m=1}^N \boldsymbol{\phi}_m \boldsymbol{\phi}_m^T D_m^2 \sum_{i=1}^n \sin^2 \bar{\omega}_m \Delta t (n-i+1) \quad (5.18)$$

by means of the orthogonality conditions in Eq. (5.3), and the simplifying assumptions in Eqs. (5.13) and (5.14). The diagonal elements of the matrix  $E(\bar{\mathbf{e}}_{n+1} \bar{\mathbf{e}}_{n+1}^T)$  are the variances of cumulative errors at various degrees of freedom of a structure. Using the notations defined in Eq. (5.15), we can store the variances in a vector  $\{\mathbf{S}_{\bar{e}}\}^2$ . Consequently, according to Eq. (5.18), we have

$$\mathbf{S}_{\bar{e}} = S_e \sqrt{\sum_{m=1}^N \{\boldsymbol{\phi}_m\}^2 D_m^2 \sum_{i=1}^n \sin^2 \bar{\omega}_m \Delta t (n-i+1)} \quad (5.19)$$

where each element of  $\mathbf{S}_{\bar{e}}$  represents the standard deviation of cumulative errors at each degree of freedom. Finally, by finding the summation of the sine square functions in the above equation as in Eq. (4.5), and applying the statistical error bound criterion, we have cumulative error bounds as

$$|\bar{e}_{n+1}| \leq S_e \sqrt{\sum_{m=1}^N \{\phi_m\}^2 J_m^2} \quad (5.20a)$$

where

$$J_m = 2 |D_m| \sqrt{\frac{n}{2} - \frac{\sin \bar{\omega}_m \Delta t n \cos \bar{\omega}_m \Delta t (n+1)}{2 \sin \bar{\omega}_m \Delta t}} \quad (5.20b)$$

### 5.2.3. Implications of the Error Bounds

Eq. (5.20) is similar to Eq. (4.6), which is derived for SDOF systems, except that it has multiple modal contributions. Since Eq. (5.20b) is exactly identical to Eq. (4.6b), the values of  $J_m$  at various  $m$  can be obtained from Fig. 4.1 by taking  $\omega = \omega_m$ . From Eq. (5.20), we can observe that the cumulative error bound at each degree of freedom is a root-sum-square combination of all the participating modes. The amount of cumulative errors contributed by each mode depends on the factor  $J_m$  and eigenvector  $\phi_m$ . In Fig. 4.1, the magnitude of  $J_m$  increases rapidly as  $\omega_m \Delta t$  increases. Therefore, the higher the modal frequency is, the greater will be the contribution to error propagation. On the other hand, the displacement response of a structure is usually dominated by its fundamental frequency. Due to these facts, cumulative errors can usually be identified as high frequency noises in MDOF pseudodynamic responses. This is a highly undesirable phenomenon. According to variation of mode shapes  $\phi_m$ , the higher frequency modes may be more significant than the fundamental mode at some degrees of freedom of a structure. At these degrees of freedom, the high frequency noises may totally overwhelm the relatively small fundamental frequency responses with large error-amplification factors  $J_m$ . For example, we can consider a cantilever structure, where displacement responses are relatively small at the lower stories, due to the dominance of the fundamental mode shape. In that case, the lower-story responses can be easily wiped out by some high frequency errors. Therefore, the existence of high frequency components is the major limitation to MDOF testing. In general, the larger the number of degrees of freedom is, the more likely will be the existence of

high frequency components.

The above observations warn against the idea that the higher-mode effects can be neglected in pseudodynamic tests, as long as the stability requirement of the integration algorithm is satisfied. This conception is generally valid in pure analytical problems, where the rounding-off errors introduced by floating-point computations in a digital computer are extremely small. In that situation, the approximation errors introduced by numerical integration are more significant. The adverse effect of the numerical errors on the higher modes is usually negligible, if the numerical method is stable and the higher mode participations are small. However, in pseudodynamic testing, experimental errors are usually so large that the higher mode excitation becomes the predominant factor in accuracy considerations.

### **5.3. Influence of Structural Characteristics on Error Propagation**

To illustrate the cumulative effects of random errors in MDOF systems, and to see how it is related to structural characteristics, we will look at two different six-degree-of-freedom structural systems. One is designed to have a more coupled stiffness matrix than the other. Using the results in the previous section, we can investigate the problems quantitatively.

#### **5.3.1. K-Braced Steel Frame**

A K-braced steel frame, shown in Fig. 5.1a, is first considered here. It is a complete bay of a six-story steel structure preliminarily proposed for pseudodynamic testing in the U.S.-Japan Cooperative Research Program. The horizontal and vertical members of the frame are assumed to be relatively rigid in axial deformation. As a result, the frame has a total of thirty degrees of freedom, as shown in Fig. 5.1b. Mass is lumped at each story level. Assuming that the structure is subjected to a horizontal base excitation, we will only consider the six lateral degrees of freedom of the frame in a pseudodynamic test.

With the member sizes shown in Fig. 5.1a, the  $30 \times 30$  stiffness matrix of the frame is first assembled using the direct stiffness method. It is subsequently reduced to a  $6 \times 6$  matrix,

for the six lateral degrees of freedom, by means of static condensation. All computations are carried out with the aid of a computer program [17]. The resulting stiffness matrix is shown in Table 5.1. The off-diagonal terms of the stiffness matrix are significantly smaller than the diagonal ones. Therefore, only a very limited degree of couplings exists between the story displacements and restoring forces on different levels.

A unit mass is lumped at each story, such that  $\mathbf{m} = \mathbf{I}$ . By solving the eigenvalue problem, we obtain all the participating frequencies and mode shapes of the structure. They are listed in Tables 5.2 and 5.3, respectively. An integration time step  $\Delta t$  of 0.01 sec is used. As a result,  $\omega_1 \Delta t$  is 0.078, which is small enough to obtain an accurate numerical result; and  $\omega_6 \Delta t$  is within the stability limit. These are ideal conditions from an analytical viewpoint. To consider the cumulative error growth during pseudodynamic testing, the values of  $|\phi_m J_m|$  are evaluated at  $n = 2000$  (i.e.  $t = 20$  sec) for all the participating modes. They are listed in Table 5.4. By means of Eq. (5.20), the root-sum-square cumulative error effect is computed and shown in the last column of the table. From this table, we can see that the higher frequencies have greater contributions to error propagation, and that the largest cumulative errors will occur at the two bottom stories, which have error bounds approximately equal to  $33S_p$ . For an equivalent SDOF system which has  $\omega \Delta t$  equal to 0.078, the maximum possible error is  $4.9S_p$ . Compared with this, the six-degree-of-freedom system has a maximum potential error of more than six times.

### 5.3.2. Reinforced Concrete Shear-Wall Structure

The second example is a six-story reinforced concrete structure with a shear wall, as shown in Fig. 5.2. It is similar in design to a seven-story structure [6] which was tested at BRI in Japan. However, as in the case with the steel frame, only the six lateral degrees of freedom are considered here. The stiffness matrix of the six-story structure, shown in Table 5.5, is obtained by fixing the lateral displacement at the bottom story of the seven-story structure, the stiffness of which was experimentally measured at BRI. From Table 5.5, we can observe that the off-diagonal elements of the stiffness matrix are relatively large. This means that the restoring force



developed at each story is significantly influenced by the displacements at the other stories. The system is, therefore, highly coupled. The mass selected for each story is taken as 3.9 kip sec<sup>2</sup>/in, so that the fundamental frequency of this structure will be identical with that of the steel frame discussed previously.

The frequencies and mode shapes obtained from the structure are shown in Tables 5.6 and 5.7, respectively. The highest frequency of the structure is about 40 times the fundamental frequency. To achieve numerical stability, integration time step  $\Delta t$  of 0.005 sec is selected. As a result,  $\omega_1 \Delta t$  is 0.039, which is half of the value for the previous frame; whereas,  $\omega_6 \Delta t$  is 1.561, which is close to the stability limit. Again, this is adequate for analytical purpose. For error-propagation studies, the values of  $|\phi_m J_m|$  at  $n = 4000$  (i.e.  $t = 20$  sec) are listed in Table 5.8. The root-sum-square effect is shown in the last column of the table. By comparing these results with Table 5.4, we can observe that the cumulative error bounds here are significantly larger than those in the steel frame. This is because of the greater higher-mode frequencies of the shear-wall frame. In this case, the maximum error can be  $159S_e$ . This means that if displacement-control errors have a standard deviation of 0.1% of the maximum structural displacement, the resulting cumulative errors can be as large as 16%. Therefore, the structure is extremely sensitive to experimental errors.

### 5.3.3. Comparisons and Comments

Due to the existence of high frequency components, the cumulative errors in the above structural systems are more significant than those in a SDOF system. By comparing the two structural examples, we observe that the highly coupled system experiences a more severe error-propagation problem because of its wider frequency span.

In the above discussions, idealized mass distribution and error properties are assumed. However, the basic phenomena observed are valid for more general conditions. For example, since error propagation depends on the frequency composition of a structure, a variation of mass distribution can affect the rate of cumulative error growth. In the cases where mass

distributions are not uniform and errors vary among the degrees of freedom, an accurate error-propagation behavior can be modelled by means of direct simulation using Eq. (5.11). In any case, to achieve the best pseudodynamic result, errors at all degrees of freedom of a system should be minimized. According to Eq. (5.11), errors at any degree of freedom can affect the overall reliability of test results.

#### 5.4. Systematic Errors

As observed in SDOF systems, systematic errors tend to oscillate at the natural frequency of a structure. However, a MDOF system has numerous frequency components. To investigate this problem from a more general aspect, we express the errors  $\mathbf{e}_i^{rd}$  in terms of a trigonometric exponential series by Fourier transformation, as in Sec. 4.4. This series is identical to the one in Eq. (4.19), which is for SDOF systems, except that the Fourier coefficients are now in a vector form, i.e.

$$\mathbf{e}_i^{rd} = \sum_{j=-k}^{k+\nu} \mathbf{c}_j e^{ij\Delta\omega\Delta t} \quad (5.21a)$$

in which the Fourier coefficient vectors are

$$\mathbf{c}_j = \frac{1}{M} \sum_{l=0}^{M-1} \mathbf{e}_i^{rd} e^{-ij\Delta\omega\Delta t l} \quad (5.21b)$$

By substituting Eq. (5.21a) into Eq. (5.11), and expressing the cumulative errors due to each frequency component in terms of Eq. (4.18), we have

$$\bar{\mathbf{e}}_{n+1} = \sum_{m=1}^N \mathbf{F}_m \sum_{j=-k}^{k+\nu} H_{jm} \mathbf{c}_j e^{i(\bar{\omega}_m \Delta t \beta_{jm} (n+1) - \theta_{jm})} \quad (5.22)$$

in which  $\beta_{jm}$  is equal to  $j\Delta\omega/\bar{\omega}_m$ ; and  $H_{jm}$  and  $\theta_{jm}$  are the values of  $H$  and  $\theta$  defined by Eq. (4.16b), corresponding to the vibration mode  $m$  and excitation frequency  $j\Delta\omega$ . Eq. (5.22) is clearly analogous to Eq. (4.20), the cumulative error equation for SDOF systems, except that it

is a linear combination of all the modal cumulative errors. Therefore, the development here is parallel to that of Sec. 4.4. By transforming the exponential series in Eq. (5.22) into an appropriate sinusoidal series, as in Eq. (4.22), and knowing that the error signals are dominated by the natural frequencies, we can approximate the cumulative errors as

$$\bar{e}_{n+1} \approx \sum_{m=1}^N F_m A_m R_m \sin(\bar{\omega}_m \Delta t n + \zeta_m) \quad (5.23)$$

in which  $R_m$  is the error-amplification factor defined by Eq. (4.13) for mode  $m$ ;  $\zeta_m$  is a phase shift which depends on the modal frequency and the phase differences of input errors; and  $A_m \approx 2 \sum_j |c_j|$ , where the  $j$ 's are those for which the  $\beta_{jm}$ 's are close to unity. This is reasonable because the  $H_{jm}$ 's approach the  $R_m$ 's, and the sine functions overlap one another as the  $\beta_{jm}$ 's go to 1. The values of  $R_m$  at various  $\omega_m \Delta t$  can be obtained from Fig. 4.3.

From Eq. (5.23), the cumulative error bounds can be conservatively estimated as

$$|\bar{e}_{n+1}| \leq \sum_{m=1}^N |F_m A_m R_m| \quad (5.24)$$

This may be an over-conservative estimation because all the peak errors usually do not occur simultaneously. However, when the natural frequencies of a structure cluster together, the sine functions in Eq. (5.23) will be only slightly off-phased. In that case, Eq. (5.24) gives a good estimate of the maximum cumulative errors. On the other hand, if the frequencies are wide apart, the  $R_m$ 's will be much greater for the higher frequencies, according to Fig. 4.3. Under that condition, two possible cases exist. First, if the errors are energy dissipating, then the higher frequency modes, which have low participations in the actual vibration response, will be readily damped out, without significant adverse effects on the overall accuracy. Consequently, only a few lower frequency modes need to be considered in Eq. (4.24). The inclusion of the higher frequency effects will be over-conservative. Second, if the errors are of the energy-addition type, then the high frequency components will dominate error propagation because of the large  $R_m$ 's. In that case, Eq. (5.24) is satisfactory because the lower frequencies have

negligible influences here. Therefore, energy-adding systematic errors are highly undesirable. As in the random error situation, the accuracy of test results is severely limited by the higher frequencies present in the system. Furthermore, when errors are systematic, error propagation cannot be suppressed by reducing  $\Delta t$ .

### 5.5. Numerical Simulations

To illustrate the previous discussions, simulations similar to those in the SDOF case are performed. The structural model used here has two degrees of freedom with mass lumped at each story level. The system properties are shown in Fig. 5.3a. It has a fundamental frequency,  $\omega_1$ , of  $10.90 \text{ sec}^{-1}$ , and a second mode frequency,  $\omega_2$ , of  $72.54 \text{ sec}^{-1}$ . This wide frequency gap provides an appropriate example to illustrate potential error-propagation problems in MDOF systems. With  $\Delta t$  equal to 0.02 sec, the corresponding numerical frequencies,  $\bar{\omega}_1$  and  $\bar{\omega}_2$ , are 10.92 and 81.16  $\text{sec}^{-1}$ , respectively. The value of  $\omega_1 \Delta t$  is 0.218, which is sufficiently small to compute an accurate first mode response; while  $\omega_2 \Delta t$  is within the stability limit. Using this integration step, the structural response to the El Centro 1940 (NS), 0.02g excitation is obtained. The displacement histories of both degrees of freedom are shown in Fig. 5.3b. They are the exact numerical solutions without experimental errors. The time histories indicate that the response is dominated by the fundamental frequency. Consequently, the  $\Delta t$  chosen is adequate for this analytical purpose, where the numerical accuracy of the higher mode response is not important.

In the simulations here, a 12-bit programmable D/A converter is used to transfer displacement control signals. Displacement is calibrated to a 5 in. range for each degree of freedom. However, the actual displacements shown in Fig. 5.3 will never exceed 0.5 in. This will produce relatively significant A/D conversion errors.

In the first simulation, rounding-off is used in the A/D conversion, such that displacement control errors generated are totally random in nature. They are shown in Fig. 5.4. The resulting displacement response and cumulative errors are displayed in Fig. 5.5. The cumulative

errors are extremely noisy. We can see that the second mode has a significant contribution to the cumulative errors because of the relatively large  $J_2$  factor. The cumulative errors at the second degree of freedom are larger than those at the first, although the actual displacement response at the latter is smaller. This is attributed to the variation of mode shapes, as discussed in Sec. 5.2.3. Using the measured standard deviation  $S_e$  of 0.00161 in., we can compute the error bounds by means of Eq. (5.20). The computed values are close to the actual cumulative error amplitudes, as shown in Fig. 5.5b. By comparing these results with those of the SDOF simulation in Fig. 4.2, we can observe the increased cumulative error growth in this two-degree-of-freedom system.

In the second simulation, truncation is used instead of rounding-off. As a result, systematic errors of the energy-addition type are generated. These signals, together with their Fourier spectra, are shown in Fig. 5.6. From the Fourier spectra, it is clear that the second mode frequency dominates the error signals. This is because the second mode effect in the cumulative errors grows so rapidly that it overwhelms the first mode displacement response, and arouses the resonance effect. This second mode excitation induces a severe error-propagation problem as shown in Fig. 5.7a. The response at the second degree of freedom is completely wiped out by the higher frequency errors. Fig. 5.7b illustrates the cumulative errors which are dominated by the higher frequency. Since both  $A_1$  and  $R_1$  are negligibly small, only the second mode effect needs to be considered in estimating the error bounds. By estimating  $A_2$  from the Fourier spectra, we can compute the error bounds with Eq. (5.24). The results obtained are extremely accurate, as shown in Fig. 5.7b. This example illustrates a very unstable condition where a high frequency component is concurrent with energy-addition errors.

### 5.6. Force, Velocity, and Acceleration Errors

Up to this point, all the attention has been directed to the accuracy of displacement response in pseudodynamic testing. However, restoring forces developed by a structure are equally important and critical to the survival of the structure. In addition, velocity and acceleration responses may also be considered by some researchers. These quantities have the same order of accuracy as displacement response in SDOF testing. In MDOF tests, the experimental results of these quantities can be totally misleading, even though the displacement response is reasonably accurate. This is due to the existence of high frequency components.

In considering the accuracy of restoring forces, we can compute the cumulative force errors from

$$\bar{e}_{n+1}^f = \mathbf{k} \bar{e}_{n+1} \quad (5.25)$$

By substituting Eq. (5.10) into this equation, and knowing that  $\mathbf{k} \phi_m = \omega_m^2 \mathbf{m} \phi_m$ , we have

$$\bar{e}_{n+1}^f = \mathbf{m} \sum_{m=1}^N \omega_m^2 \phi_m \bar{E}_{m(n+1)} \quad (5.26)$$

The comparison of the above equation with Eq. (5.10) indicates that cumulative force errors are more significantly dominated by the higher modes than cumulative displacement errors, due to the  $\omega_m^2$  factors. Therefore, restoring forces have more severe error propagation in pseudodynamic testing, especially when an extremely high frequency is present. This will be illustrated by an example in Chapter 7 (see Fig. 7.3). Because of this fact, unrealistically large forces can be developed in a structure during pseudodynamic experiments; and the structure may suffer premature yielding or failure.

Similarly, velocity and acceleration responses have more significant higher frequency errors than displacement response. In these cases, modal contributions will be amplified by factors of  $\omega_m$  and  $\omega_m^2$ , respectively. Thus, acceleration suffers the same order of inaccuracy as restoring forces.

### 5.7. Summary

Because of the higher mode effect, cumulative errors can grow rapidly in MDOF systems. In the cases where errors are random, or systematic with an energy-addition effect, the highest structural frequency is always the dominating factor in error propagation. Consequently, highly coupled, stiff structures which have relatively wide frequency spans can experience a severe error-propagation problem. The systematic errors which dissipate energy are less undesirable, because they rapidly damp away insignificant higher mode responses, and moderately affect the lower frequency modes. Therefore, the removal or suppression of high frequency components is highly recommended for MDOF testing. The methods to achieve that include the use of high frequency filters and frequency proportional numerical damping. The latter will be discussed in Chapter 7.

## CHAPTER 6

### ERROR PROPAGATION IN INELASTIC SYSTEMS

#### 6.1. Introduction

In the previous chapters, analytical methods were developed to predict the growth of cumulative errors in pseudodynamic testing of linear elastic systems. However, as inelastic deformations occur, the error-propagation characteristics will change because of the variation of structural stiffness in the inelastic range. Consequently, the results previously obtained for linear elastic systems will no longer be applicable. In this chapter, we extend our investigation of error propagation to inelastic systems. The inelastic error-propagation behavior will be formulated using an idealized SDOF elasto-plastic model. With the supplement of numerical simulations, the idealized model will be used to identify the basic error-propagation mechanisms in inelastic systems. Furthermore, parametric studies by means of numerical experiments are carried out to gain a more thorough understanding of cumulative error growth in inelastic systems under various conditions. By comparing the results of these studies with those of linear elastic systems, some criteria for assessing the reliability of the pseudodynamic method in testing inelastic structures will be established.

#### 6.2. SDOF Elasto-Plastic Systems

In the subsequent studies, a SDOF elasto-plastic model, shown in Fig. 6.1, will be used. This model is an idealized representation of general inelastic material behavior. As we will see in the following simulations, the error-propagation behavior in inelastic systems depends on various factors, such as the characteristics and magnitudes of external excitations, the inelastic deformations developed, and the dynamic properties of a structure. Therefore, the exact error-propagation behavior will vary from case to case. For this reason, only qualitative evaluations and relative comparisons of the simulation results are possible. An elasto-plastic model well suits these objectives.



### 6.2.1. Cumulative Error Equation

The equation for cumulative displacement errors in elasto-plastic systems can be developed from Eq. (3.3), the recursive step-by-step integration formulation, as in linear elastic systems. For the elasto-plastic case,  $r_{i+\nu}$  is the inelastic restoring force, which can be modelled as

$$r_i = k (d_i - d_i^r) \quad (6.1a)$$

or

$$r_i = \mathbf{S} (\mathbf{x}_i - \mathbf{x}_i^r) \quad (6.1b)$$

in which  $k$  is the linear stiffness of the elastic region;  $d_i^r$  is the residual displacement in step  $i$ , as shown in Fig. 6.1; and  $\mathbf{x}_i^r$  is a residual vector which contains  $d_i^r$ . By substituting Eq. (6.1b) into Eq. (3.3), and introducing the error terms as in Sec. 3.2, we can obtain

$$\bar{\mathbf{e}}_{i+1} = \mathbf{A} \bar{\mathbf{e}}_i + \mathbf{B} \mathbf{e}_i^{rd} - \mathbf{L} \mathbf{S} (\mathbf{e}_{i+\nu}^{rd} - \bar{\mathbf{x}}_{i+\nu}^r + \mathbf{x}_{i+\nu}^r) \quad (6.2)$$

in which  $e_{i+\nu}^{rd}$  is the equivalent displacement error defined by Eq. (3.6) with the linear elastic stiffness  $k$ ; and vector  $\bar{\mathbf{x}}_{i+\nu}^r$  contains the computed residual displacement  $\bar{d}_{i+\nu}^r$  under the influence of experimental errors, while  $\mathbf{x}_{i+\nu}^r$  is the exact residual vector. Finally, by going through the same procedure as in Chapter 3, and by taking out the displacement-feedback error term, we can get the cumulative error equation:

$$\bar{e}_{n+1} = \bar{e}_{n+1}^e + \bar{e}_{n+1}^i \quad (6.3a)$$

in which

$$\bar{e}_{n+1}^e = D \sum_{i=1}^n e_i^{rd} \sin \bar{\omega} \Delta t (n-i+1) \quad (6.3b)$$

$$\bar{e}_{n+1}^i = D \sum_{i=1}^n (d_i^r - \bar{d}_i^r) \sin \bar{\omega} \Delta t (n-i+1) \quad (6.3c)$$

Eq. (6.3b) has the identical form as Eq. (3.30), which is the cumulative error equation for linear elastic systems. Therefore, the term  $\bar{e}_{n+1}^e$  can be considered as the elastic cumulative error component. The additional error term  $\bar{e}_{n+1}^i$  is due to inelastic or residual deformations, as indicated by the expression  $(d_i^r - \bar{d}_i^r)$  in Eq. (6.3c). In a similar way, the numerical formulation of inelastic displacement response can be decomposed into two components:

$$d_{n+1} = d_{n+1}^e + d_{n+1}^i \quad (6.4a)$$

in which

$$d_{n+1}^i = -D \sum_{i=1}^n d_i^r \sin \bar{\omega} \Delta t (n-i+1) \quad (6.4b)$$

The  $d_{n+1}^e$  term is the linear elastic displacement component which would be the total response if a structure remained elastic, while  $d_{n+1}^i$  is the additional inelastic displacement component due to structural yielding. By analogy, the inelastic component can be numerically conceived as a displacement response induced by a series of impulse loadings. These fictitious loadings result from the sudden stiffness change at the moment of yielding. Therefore, the inelastic component contains displacement drifts which we can often observe from inelastic structural responses. Similar observation can be made from the inelastic cumulative error component.

Eqs. (6.3) and (6.4) are the "linearized" equations of error propagation and displacement response, respectively, for an elasto-plastic system. The values of  $D$  and  $\bar{\omega}$  are based on the linear elastic stiffness of the system. As a result, we can identify and compare the inelastic mechanisms in error propagation.

### 6.2.2. Equivalent Displacement Errors

In the above cumulative error equation, the equivalent displacement errors  $e_i^{rd}$  and other parameters are defined in terms of the linear elastic stiffness. Therefore, according to Eqs. (2.4) and (3.6), the equivalent displacement errors in inelastic systems are

$$e_i^{rd} = \frac{k_i}{k} e_i^{dc} + \frac{1}{k} e_i^{rm} \quad (6.5)$$

in which  $k_i$  is the tangent stiffness. In an elasto-plastic model,  $k_i$  is equal to zero during progressive yielding, and to the linear elastic stiffness during loading or unloading. As a result, the  $e_i^{rd}$ 's in elasto-plastic systems are always smaller than or equal to those in linear elastic cases, for the same magnitudes of errors  $e_i^{dc}$  and  $e_i^{rm}$ . For this reason, the conclusions of the following studies, using simulated force-measurement errors  $e_i^{rm}$ , can be conservatively extended to cover other forms of errors.

### 6.3. Numerical Simulations using the Elasto-Plastic Model

#### 6.3.1. System Description and Numerical Results

The error-propagation mechanisms in elasto-plastic systems can be investigated by means of numerical simulations. In the following simulations, we use a SDOF elasto-plastic model which has a linear elastic stiffness of 3.702 kips/in. and a mass of 0.01035 kip sec<sup>2</sup>/in. Thus, the system has an initial period of  $\omega = 18.91 \text{ sec}^{-1}$ . The yield strength  $r_y$  is 0.36 kip. The El Centro 1940 (NS) accelerogram with a peak acceleration of 0.1g is used to develop reasonable inelastic deformations in the system. To study the error-propagation behavior, we introduce force-measurement errors into the simulations. These errors are modelled by

$$e_i^r = e_i^{rm} = e \frac{\Delta \bar{d}_i}{|\Delta \bar{d}_i|} \quad (6.6)$$

which means that if  $e$  is positive, the errors are of the energy-dissipation type. We select  $e$  to be positive and be 10% of  $r_y$ .

An integration step of 0.02 sec is used in the numerical computations. The results are illustrated in Fig. 6.2. The first graph in the figure shows the displacement response histories with and without errors. The energy-dissipation effect of the errors can be observed from the

reduced amplitudes of the erroneous response. The second graph illustrates the decomposed cumulative error components as formulated by Eq. (6.3). The elastic component  $\bar{e}_{n+1}^e$ , which is represented by a solid line, is similar to the error-propagation behavior observed from linear elastic systems. It has a symmetrical oscillatory growth. The inelastic component  $\bar{e}_{n+1}^i$  is about 180 degrees out-of-phase with  $\bar{e}_{n+1}^e$ . It offsets  $\bar{e}_{n+1}^e$  during early cycles, and drifts away from the time axis at later ones. This contributes to the drift phenomenon in the total cumulative errors, which are shown by the last graph of Fig. 6.2. A comparison of the inelastic displacement component  $d_{n+1}^i$  and the inelastic error component  $\bar{e}_{n+1}^i$  is shown by the first graph of Fig. 6.3. These inelastic components have similar behaviors. They tend to drift away from the time axis with different magnitudes. The corresponding residual displacement  $d_i^r$  and residual error ( $d_i^r - \bar{d}_i^r$ ) are shown in the second graph.

For the purpose of comparison, a linear elastic simulation is performed with the same elastic period and force errors as the previous one. The results are shown by Fig. 6.4. The cumulative errors  $\bar{e}_{n+1}$  observed here are much greater than those in Fig. 6.2. The system response is drastically damped by the energy-dissipating errors. Although  $\bar{e}_{n+1}^e$  in the previous case has the same formulation as  $\bar{e}_{n+1}$  in the linear elastic system, the magnitude of  $\bar{e}_{n+1}^e$  observed is smaller.

The last simulation is performed with inelastic deformations and a peak ground acceleration of 0.15g. This increased excitation level produces a very different inelastic response history as illustrated in Fig. 6.5. However, the error-propagation behavior is similar to the previous results. The inelastic component  $\bar{e}_{n+1}^i$  tends to offset  $\bar{e}_{n+1}^e$  at some places, and causes a displacement drift at others.

### 6.3.2. Implications Regarding Inelastic Error Propagation

Due to the inelastic component  $\bar{e}_{n+1}^i$ , the error-propagation behavior in the elasto-plastic model is very different from that in linear elastic systems. In the latter, cumulative errors are of the oscillatory type. They are dominated by the resonance phenomenon provided that input

errors are systematic. The linear elastic error propagation does not depend on the magnitude or characteristics of external excitations; instead, it is a function of  $\omega\Delta t$  and  $n$ . On the other hand, the cumulative errors in elasto-plastic systems produce a drift effect, with a slow oscillatory growth. The resonance phenomenon in error propagation is suppressed by the frequency changes during inelastic deformations. The oscillatory growth of cumulative errors is also offset or damped by an inelastic drift mechanism. Since the  $d'_{n+1}$  and  $\bar{e}'_{n+1}$  components are of the same nature, the estimation of inelastic cumulative error growth would be as difficult as the prediction of inelastic structural response. The magnitude of  $\bar{e}'_{n+1}$  is dependent on inelastic deformations developed.

In general pseudodynamic testing, we can expect that cumulative errors will start with an oscillatory growth in the elastic range. As soon as inelastic deformations occur, the oscillatory growth of cumulative errors will be suppressed and a displacement drift is produced. If inelastic deformations are small, error propagation will remain similar to that in linear elastic systems, i.e.  $\bar{e}''_{n+1}$  will dominate. If inelastic deformations are severe, the less predictable  $\bar{e}'_{n+1}$  component will dominate. Therefore, error propagation in inelastic systems varies under different conditions.

#### 6.4. Parametric Studies of Error Propagation

To identify the basic error-propagation characteristics in inelastic systems, we study a series of error spectra for various parameters using the SDOF elasto-plastic model. From the simulations in the previous section, we observe that error-propagation behavior varies with the level of inelastic deformations. The maximum inelastic deformation developed in a SDOF system can be expressed by a dimensionless quantity  $\mu_d$ , which is called the displacement ductility and is defined as the ratio of the maximum displacement developed over the yield displacement, i.e.  $\mu_d = d_{\max}/d_y$ . If an elasto-plastic structure is subjected to a ground excitation, the displacement ductility  $\mu_d$  developed can be determined in terms of a dimensionless coefficient  $\eta$  [18]. This coefficient is a measure of structural resistance to the intensity of a specific ground

excitation, and is defined as

$$\eta = \frac{r_y}{m \{a_g\}_{\max}} \quad (6.7)$$

in which  $\{a_g\}_{\max}$  is the peak ground acceleration of the record. In general, the smaller the value of  $\eta$  is, the larger will be the displacement ductility. For this reason, various values of  $\eta$  will be included in each error spectrum to study the influence of  $\mu_d$  in error propagation. Each spectrum has a period range of 0.1 to 1.0 sec at 0.1 sec intervals. The errors  $e_i^{rd}$  used to generate the spectra are again modelled by Eq. (6.6). The error magnitude  $e/k$  in each spectrum is specified as a fraction of the yield displacement  $d_y$ . In addition, the maximum cumulative errors obtained in the following studies are normalized to dimensionless quantities. Consequently, the results presented here indicate general characteristics of the elasto-plastic model under certain specific excitation records.

#### 6.4.1. Error Ratio Spectra

A series of error ratio spectra is generated using 15 seconds of the El Centro 1940 (NS) record with zero damping. The magnitudes of the earthquake are determined by the selected  $\eta$  values, which are 0.9, 0.8, 0.6, 0.4 and 0.3, respectively. These will yield a wide range of displacement ductilities. The results are shown in Fig. 6.6. The error ratio is defined here as the ratio of the maximum cumulative error developed in an inelastic simulation over the maximum error expected for the corresponding linear elastic system of the same period. The maximum expected error is computed by means of Eq. (4.14). The magnitudes of the input errors  $e_i^{rd}$  are  $0.001d_y$ ,  $0.01d_y$ ,  $0.05d_y$  and  $0.1d_y$ , respectively. Integration time step  $\Delta t$  of 0.02 sec is used throughout the computations. From Fig. 6.6, we can observe that the maximum cumulative errors in elasto-plastic systems are, in most cases, less than those expected for the corresponding linear elastic systems. This is probably due to the suppression of resonance effect in error propagation by inelastic deformations. A general trend can be observed from the spectra here. The larger  $\eta$  values tend to have smaller error ratios. This indicates that cumulative errors tend

to be larger when higher displacement ductilities are developed. At period equal to 0.1 sec and  $\eta$  equal to 0.3, the error ratios observed are large, occasionally exceeding 1. This is due to the extremely large displacement ductilities developed at that period. Furthermore, the error ratios tend to be smaller in spectra which have larger magnitudes of  $e_i^{rd}$ . This means that cumulative errors in elasto-plastic systems do not increase as fast as those in linear elastic systems as the magnitude of input errors increases.

#### 6.4.2. Relative Error Spectra

The accuracy of a pseudodynamic test does not depend on the magnitude of cumulative errors alone. It also depends on the displacement ductility developed. Therefore, we are more concerned with the relative magnitudes of cumulative errors, rather than the absolute values. To find the influence of displacement ductility on the accuracy of pseudodynamic results, relative error spectra are generated using the same excitation record as before. They are shown in Fig. 6.7. The relative error is defined as the ratio of the maximum cumulative error over the maximum displacement response developed in a system. By comparing Fig. 6.7 to Fig. 6.6, we note that although relatively large error ratios are produced at the 0.1 sec period, the corresponding relative errors are small. This can be explained by the large displacement ductilities at 0.1 sec period. The general trend observed from Fig. 6.7 is that the smaller the value of  $\eta$  is, the smaller will be the relative error. Therefore, pseudodynamic results will be more accurate if larger ductilities are developed in a system. This is a reasonable phenomenon because the energy effects produced by systematic errors become less significant as inelastic hysteretic energy dissipation increases.

#### 6.4.3. Error Spectra under Various Conditions

To check whether the previous results are consistent, error spectra generated under various conditions are shown in Fig. 6.8. The magnitude of the input errors is  $0.01d_y$  for all spectra. The integration time step is reduced to 0.01 sec. In the first row of Fig. 6.8, the error ratio and

relative error spectra are generated with the El Centro 1940 record. The second row contains the spectra produced by the Miyagi Oki 1978 ground acceleration record. Finally, the spectra in the third row are again generated by the El Centro ground motion, but with an energy-addition type of  $e_1^{rd}$ .

Although the distributions and magnitudes of the spectral values differ under various conditions, the basic characteristics remain the same. The Miyagi Oki record shows larger error ratios than the El Centro record, but most of the values still remain under 1. Error ratios always tend to be larger at higher displacement ductility levels, and the reverse is true for relative errors. In addition, the change of  $\Delta t$  does not significantly affect the spectral values. This is the characteristic observed from systematic errors in linear elastic systems.

#### 6.4.4. Commentary

In general, error-propagation characteristics of elasto-plastic systems vary under different conditions, such as the ground excitations used and the displacement ductility developed. However, several basic characteristics remain unchanged. Cumulative errors in inelastic models are usually smaller than those in linear elastic systems. However, cumulative errors will grow as displacement ductilities increase; and they may exceed those in linear elastic systems when extremely high ductilities are developed. In any case, they are usually relatively small when compared to the maximum displacement response developed, as long as the input errors are reasonably small. Most often, the larger the displacement ductility is, the smaller is the relative error and the more accurate is the result. In addition, the magnitude of cumulative errors in linear elastic systems is proportional to the size of input errors, while cumulative errors are less sensitive to input errors in the inelastic model. Finally, we can conclude that the development of inelastic deformation may or may not increase the magnitudes of cumulative errors, depending on the inelastic deformation developed. In any case, inelastic deformation is not detrimental to pseudodynamic testing, since any increase in cumulative errors is usually offset by a greater increase in inelastic displacement.



### 6.5. Reliability Criteria in Inelastic Pseudodynamic Testing

From the parametric studies, we observe that cumulative error growth in inelastic systems is less predictable than that in linear elastic cases. To assess the reliability of inelastic pseudodynamic testing, we summarize the results of the parametric studies in a more revealing form, and compare them with linear elastic error propagation. To do that, some of the relative errors obtained in the previous section are normalized and plotted against displacement ductilities in Fig. 6.9. They are normalized with respect to an *elastic criterion*, which is defined here as the ratio of the maximum cumulative errors expected for the corresponding linear elastic system to the yield displacement  $d_y$ . Consequently, a normalized relative error can also be written as (error ratio)/ $\mu_d$ , according to the previous definitions. The elastic criterion is a measure of the accuracy of a pseudodynamic testing if a structure deforms up to its elastic limit. It can be obtained from the results of Chapter 4. By this normalization, the reliability criteria of inelastic testing can be established with respect to those of linear elastic tests.

From the scattered data points in Fig. 6.9, we can observe that the normalized relative errors are approximately inversely proportional to the ductility level. Therefore, a pseudodynamic test is generally more accurate if a higher displacement ductility is developed. For comparison purpose,  $1/\mu_d$  is plotted against  $\mu_d$  as a solid line in the same figure. This curve indicates the corresponding reduction of relative errors if a structure remained elastic at displacements beyond  $d_y$ . It is, therefore, the curve of normalized relative errors for linear elastic systems. Within the ductility range of 40, we can see from the figure that most of the points from the inelastic simulations lie below the solid curve. Only at large ductility levels (beyond 10), are a few points slightly above the curve. As a result, Fig. 6.9 confirms that inelastic pseudodynamic testing is usually more accurate than linear elastic tests. Furthermore, an inelastic pseudodynamic test can be reasonably accurate, even though the accuracy within the elastic limit is poor.

Under the absence of more reliable information, the curve in Fig. 6.9 can serve as a conservative assessment of the accuracy of inelastic testing. For example, if a ductility of 20 is

expected from a pseudodynamic test, the curve indicates that the normalized relative error will be approximately 0.05. If the tolerance limit of cumulative errors is set to be 10% of the maximum displacement, then the maximum cumulative error within the elastic range should be less than  $2d_y$ . In general, the yield displacement  $d_y$  and the ductility  $\mu_d$  are difficult to define in realistic inelastic systems, especially when a system has multiple degrees of freedom. However, according to the above discussions, we can use the error-propagation criteria for linear elastic systems to assess the reliability of inelastic testing. These criteria may become unconservative only if severe inelastic deformations take place.

## CHAPTER 7

### ERROR COMPENSATION AND NOISE REMOVAL METHODS FOR PSEUDODYNAMIC TESTING

#### 7.1. Introduction

Experimental errors in pseudodynamic testing have been discussed in Chapter 2 of this report. From the error-propagation studies, we observe that the errors which are most detrimental to pseudodynamic testing are of the systematic nature. The problems of these systematic errors can be summarized as: (i) causing an erroneous apparent stiffness of a test structure, e.g. by mis-calibration of measurement transducers; (ii) inputting extra energy into response motions, e.g. due to truncation errors in the A/D conversions; or (iii) dissipating energy from structural responses, e.g. due to frictional forces.

In reality, the elastic stiffness of a structure may vary from case to case, even though exactly the same material and member sizes are used for fabrication. Stiffness can be influenced by many factors, such as types of member connections used, imperfect geometric configurations, and base support conditions, especially. For this reason, the actual stiffness of a structure often differs from the analytically predicted stiffness. Under normal circumstances, this discrepancy is substantially greater than the influence of experimental errors. Therefore, the problem in (i) is usually insignificant, and can be neglected. Furthermore, since the frequencies of a structure can always be manipulated through the assumed mass distribution in a pseudodynamic test, a small stiffness error introduced under experimental conditions can be easily compensated for in most cases.

The energy changes due to experimental errors are manifested in a form of force-deformation hysteresis. These energy effects can be of significant influence on pseudodynamic results. For example, large frictional forces in a system or systematic overshooting of displacements can induce unduly large damping effect on response motions. On the other hand, energy addition by systematic truncation errors or undershooting of displacements will excite spurious high frequency modes, which cause stability problems in pseudodynamic testing of MDOF

systems. In the worst case, both phenomena can co-exist, such that the higher frequency modes grow rapidly, while the more realistic fundamental mode is damped out. These energy effects are most undesirable, and can be cited as the major problems from previous experience. Pseudodynamic results will not be reliable if these energy changing errors are not eliminated or properly compensated for.

In this chapter, two numerical methods are proposed to solve the above problems. The first method uses equivalent hysteretic energy compensation, which can cancel out the energy changes introduced by systematic errors. This method, assuming a constant magnitude force correction at each degree of freedom, is especially efficient for correcting force measurement errors, such as those due to friction. The second method is a modified Newmark explicit algorithm which has an adjustable numerical damping. By using this modified integration algorithm, the higher mode effect can be damped out without significant influence on the lower modes. These two methods can be used simultaneously to achieve a stable and reliable pseudodynamic test result.

## **7.2. Equivalent Hysteretic Energy Compensation**

As mentioned in Chapter 2, systematic errors often introduce energy adding or dissipating hystereses into the force-deformation relations of linear elastic SDOF systems. These hystereses can be easily measured in most SDOF experiments. They can be numerically compensated for by correcting the restoring force feedback, as shown in Fig. 7.1. Similar phenomenon exists in MDOF systems. However, due to the couplings among the structural degrees of freedom, the hysteretic energy behavior is difficult to measure. It involves  $N^2$  inter-relations in a  $N$ -degree-of-freedom system. Under this condition, numerical compensation is difficult. Since the higher modes are more sensitive to errors, an inadequate correction may aggravate the problem. To compensate for the erroneous energy effects in MDOF systems, and to avoid the difficulties mentioned above, an iterative correction process which uses an equivalent hysteretic energy concept is developed here.

### 7.2.1. Theoretical Basis

To reduce the complexity of the error compensation problem, we assume that force-feedback errors at each degree of freedom are of constant magnitude throughout a pseudo-dynamic test. The signs of these errors are determined by the direction of force variation. In this way, we can approximately simulate the energy changing hysteretic behavior caused by systematic errors. Using these assumptions, the equations of undamped motion of a linear elastic MDOF system can be represented as

$$\mathbf{m} \ddot{\mathbf{d}} + \mathbf{k} \mathbf{d} + \left\{ \tilde{e}_i^f \frac{\dot{r}_i}{|\dot{r}_i|} \right\} = \mathbf{f} \quad (7.1)$$

in which the last term on the left hand side is a vector of force-feedback errors;  $\tilde{e}_i^f$  is a constant magnitude error at degree of freedom  $i$ ; and  $\dot{r}_i$  is the corresponding rate of force variation. Therefore, the  $\tilde{e}_i^f$  term is positive if it is energy dissipating, and negative otherwise. Applying the *conservation of energy principle* to Eq. (7.1), we obtain

$$\frac{1}{2} \dot{\mathbf{d}}^T \mathbf{m} \dot{\mathbf{d}} + \frac{1}{2} \mathbf{d}^T \mathbf{k} \mathbf{d} + \int_0^t \dot{\mathbf{d}}^T \left\{ \tilde{e}_i^f \frac{\dot{r}_i}{|\dot{r}_i|} \right\} dt = \int_0^t \dot{\mathbf{d}}^T \mathbf{f} dt \quad (7.2)$$

in which the first term on the left hand side is the kinetic energy of the system, the second term is the strain energy stored, and the third is the work done by the force errors. The sum of these three terms is equal to the total energy input by the external force  $\mathbf{f}$ . If a system is excited by a horizontal base acceleration, then

$$\int_0^t \dot{\mathbf{d}}^T \mathbf{f} dt = - \int_0^t \dot{\mathbf{d}}^T \mathbf{m} \{1\} a_g dt \quad (7.3)$$

where  $a_g$  is the base acceleration, and  $\{1\}$  is a unit vector with all elements equal to 1. By transforming Eq. (7.2) into a system of modal energy equations, we can obtain the error  $\tilde{e}_i^f$  at each degree of freedom of a system. To do this, we substitute Eq. (5.4) into Eqs. (7.2) and (7.3), and utilize the orthogonality conditions of the eigenvectors. Consequently, we obtain

$$\sum_{m=1}^N \left[ \frac{1}{2} M_m \dot{D}_m^2 + \frac{1}{2} K_m D_m^2 + \int_0^t \dot{D}_m \phi_m^T \left\{ \tilde{e}_i^T \frac{\dot{r}_i}{|\dot{r}_i|} \right\} dt \right] \quad (7.4)$$

$$= - \sum_{m=1}^N \int_0^t \dot{D}_m \phi_m^T \mathbf{m} \{1\} a_g dt$$

for a  $N$ -degree-of-freedom system. The quantities  $M_m$  and  $K_m$  are the generalized mass and stiffness for mode  $m$ , as defined by Eq. (5.6). The above equation implies that the sum of the energy in all participating modes is conserved. Since energy can be neither gained nor lost at each mode in a closed system, Eq. (7.4) can be equivalently expressed as a system of  $N$  equations:

$$\frac{1}{2} M_m \dot{D}_m^2 + \frac{1}{2} K_m D_m^2 + \int_0^t \dot{D}_m \phi_m^T \left\{ \tilde{e}_i^T \frac{\dot{r}_i}{|\dot{r}_i|} \right\} dt = - \int_0^t \dot{D}_m \phi_m^T \mathbf{m} \{1\} a_g dt \quad (7.5)$$

for  $m = 1, 2, \dots, N$ . These equations, enforcing the conservation of energy at each mode, can be further transformed to

$$\frac{1}{2} M_m \dot{D}_m^2 + \frac{1}{2} K_m D_m^2 + \sum_{i=1}^N \phi_{mi} \tilde{e}_i^T \int_0^t \dot{D}_m \frac{\dot{r}_i}{|\dot{r}_i|} dt = - \int_0^t \dot{D}_m a_g dt \sum_{i=1}^N \phi_{mi} m_i \quad (7.6)$$

for  $m = 1, 2, \dots, N$ . The quantity  $\phi_{mi}$  is the  $i$ th element of the eigenvector  $\phi_m$ , and  $m_i$  is the mass at degree of freedom  $i$ . Consequently, the  $\tilde{e}_i^T$ 's can be found by solving the system of linear equations:

$$\mathbf{A} \tilde{\mathbf{e}}^T = \mathbf{b} \quad (7.7a)$$

where matrix  $\mathbf{A}$  has elements represented by

$$a_{mi} = \phi_{mi} \int_0^t \dot{D}_m \frac{\dot{r}_i}{|\dot{r}_i|} dt \quad (7.7b)$$

and vector  $\mathbf{b}$  has elements:

$$b_m = -\frac{1}{2} M_m \dot{D}_m^2 - \frac{1}{2} K_m D_m^2 - \int_0^t \dot{D}_m a_g dt \sum_{i=1}^N \phi_{mi} m_i \quad (7.7c)$$

Therefore, if force errors in a pseudodynamic system are of the idealized form, they can be easily computed by obtaining  $\mathbf{A}$  and  $\mathbf{b}$  from a trial pseudodynamic test.

### 7.2.2. Application

Errors in real experiments are more irregular than what we have assumed. The  $\bar{e}_i^f$ 's found from the equivalent energy approach are constant magnitude force errors, which have the same amount of energy effect as the actual experimental errors. These equivalent energy errors can serve for two useful purposes. They can be used as error indices for pseudodynamic results. In addition, they represent the amount of compensation required to correct the force-feedback values. If the actual errors in a pseudodynamic system are of the idealized form as in Eq. (7.1), then all the erroneous energy effects can be eliminated by adding an error compensation vector of  $-\{\bar{e}_i^f \dot{r}_i / |\dot{r}_i|\}$  to the restoring force feedback. Unfortunately, this is usually not the case. Displacement control errors may vary with displacement levels. Force errors will vary accordingly, with contribution from every other degree of freedom of a system. Under these circumstances, a single compensation may not lead us to a correct result, and an iterative correction is recommended. The  $\bar{e}_i^f$ 's found at each iterative trial can be accumulated to the error compensation vector until they become satisfactorily small. The convergence of the iterative correction cannot be formally proved here, but conceptually it should approach a better result after every trial. The closer the actual errors to the idealized form are, the less number of iterations will be needed. For this reason, this method is especially useful for correcting force-measurement errors, such as those due to frictional forces, which are approximately constant throughout a test.

### 7.2.3. Examples

To illustrate the validity of the energy compensation method, it is applied to a two-degree-of-freedom simulation. This system has the same properties as the one used in Sec. 5.5. The fundamental frequency  $\omega_1$  is  $10.92 \text{ sec}^{-1}$ , and  $\omega_2$  is  $81.16 \text{ sec}^{-1}$ , such that the second mode is very sensitive to experimental errors. The correct response of the system, when subjected to the El Centro 1940 (NS),  $0.02g$  ground acceleration, is shown in Fig. 7.2. The integration step used is  $0.01 \text{ sec}$ . From the figure, we can observe no obvious second mode participation in the displacement response. However, the force history contains a moderate amount of second mode effect.

To simulate a bad experimental setup, three types of errors are introduced into the system. First, constant magnitude frictional forces of  $0.002 \text{ kip}$  are simulated to influence the force-feedback values at both degrees of freedom. Secondly, the jack displacements at the first and second degrees of freedom are deliberately mis-calibrated by  $1.5\%$  and  $2.0\%$ , respectively, such that some energy will be dissipated by the inconsistent jack motions. Finally, truncation is used to convert analog displacement values computed to digital signals; and displacement measurements are calibrated to  $0.5$  and  $5.0 \text{ in.}$  ranges for DOF 1 and 2, respectively. Therefore, relatively large truncation errors, which add energy into response motions, will occur at the second degree of freedom. With these assumptions, the response of the system is numerically computed, and shown in Fig. 7.3. We can see that the second mode is significantly excited in the displacement and force responses by truncation errors. Furthermore, the force response is totally overwhelmed by the high frequency noise, such that the maximum force experienced by the structure becomes ten times greater than what would actually be developed. The result is, therefore, unacceptable.

Subsequently, the equivalent energy method is used to correct the above situation. By using this method, we achieve a satisfactory result with eight iterative corrections, in each of which we take five samples of  $\bar{e}_i^j$  at equal time intervals. The averages of these samples are added to the cumulative force compensation vector. At the end of corrections, the average



values of  $\tilde{e}_1^f$  and  $\tilde{e}_2^f$  are reduced from 0.0072 and -0.0123 kip to 0.0026 and -0.0017 kip, respectively. The correction procedure is shown in Table 7.1. The final results are shown in Fig. 7.4, from which we can observe that most of the high frequency errors are removed, and the correct response is closely restored.

However, the rate of convergence in this example is slow. We can show that the number of iterations required depends on the selection of compensation values at each trial. Due to the existence of high frequency modes, adding energy into a system has a more drastic effect than taking energy away from it. With this idea, we can increase the convergence rate in the previous example, but avoid additional excitation on the second mode at the same time. This is done in the following way. Instead of taking the averages of five samples as compensation values, we select the maximum energy-addition errors and the minimum dissipative errors at each trial. In this way, the undesirable growth of the second mode is rapidly eliminated, but the energy dissipation is only gradually compensated for. Using this approach, we can obtain the same level of accuracy as the previous example with five trials. The rates of these two approaches are compared in Fig. 7.5.

### 7.3. Noise Removal by Numerical Damping

Some implicit integration algorithms, like the Newmark family of methods, Wilson's  $\theta$ -method, and Houbolt's method [12], are highly desirable for the analysis of structural systems which have large numbers of degrees of freedom. Besides the fact that they are unconditionally stable, they also have a numerical damping property, which can suppress the spurious growth of higher frequency modes. Hilber's  $\alpha$ -method [13] has the additional advantages that the numerical dissipation can be controlled by a parameter other than the time step, and that the lower frequency modes are only moderately affected by the dissipative property.

Numerical damping is extremely helpful in pseudodynamic testing for two reasons. First, it can be conveniently included to model the damping property of a structural system, both in the elastic and inelastic ranges. Further, since the spurious growth of the higher modes due to

experimental errors is the main source of system instability, the suppression of the higher frequencies by numerical damping can ensure good experimental results. For these reasons, it is desirable to use a dissipative explicit integration algorithm in pseudodynamic experiments.

### 7.3.1. Orthogonal Viscous Damping

In the analysis of linear elastic MDOF systems, damping ratios  $\xi_i$  of all vibration modes can be specified by a damping matrix of the form [16]:

$$\mathbf{c} = \mathbf{m} \sum_b a_b [\mathbf{m}^{-1} \mathbf{k}]^b \quad (7.8a)$$

in which the values of  $a_b$ 's are determined by the equation:

$$\xi_n = \frac{1}{2 \omega_n} \sum_b a_b \omega_n^{2b} \quad (7.8b)$$

This damping matrix has the orthogonality property with the eigenvectors of the structural system, as described by Eq. (5.3c). By means of Eq. (7.8b), we can select appropriate parameters  $a_b$ 's for suppressing the higher frequency responses with severe dampings, while keeping the lower modes reasonably damped. To illustrate that, we take the two-degree-of-freedom example with truncation errors in Sec. 5.5 (Fig. 5.7). In this case, damping can be introduced by a specific form of Eq. (7.8a):

$$\mathbf{c} = a_0 \mathbf{m} + a_1 \mathbf{k} \quad (7.9)$$

which has  $b$ 's equal to 0 and 1, respectively. This is the conventional Rayleigh damping. To suppress the spurious growth of the second mode, we specify  $\xi_1$  and  $\xi_2$  to be 0.005 and 1.0, respectively. The parameters  $a_0$  and  $a_1$  are then determined by solving Eq. (7.8b). Using the same excitation record and numerical procedure as in Sec. 5.5, we perform a simulation with the Rayleigh damping. The result is shown in Fig. 7.6. By comparing that with Fig. 5.7, we can see substantial improvement in the simulation results. The high frequency noise is suppressed.

However, problem arises when a structure becomes nonlinear. Since the orthogonal damping matrix depends on the stiffness of a structure, it has to be re-computed as the stiffness changes. The sensitivity of this damping to the nonlinear stiffness effect is not known. Based on Eq. (7.8b), it is clear that the effective damping ratio can vary radically with frequency and, in some cases, give negative values. In other words, the parameters  $a_b$ 's determined for a specific system may not be appropriate for a system with a different stiffness. Since we cannot directly monitor stiffness changes during pseudodynamic testing, we have a problem of determining an adequate damping matrix for nonlinear structures. For this reason, an explicit integration algorithm which has numerical damping is proposed here. The advantage of the new algorithm lies in the fact that numerical damping ratios are approximately frequency-proportional. The higher the frequency is, the larger will be the damping. As a result, the damping ratios of the participating modes are automatically re-adjusted by the algorithm as frequencies are changed by nonlinear deformations. Explicit knowledge of the structural stiffness is no longer necessary.

### 7.3.2. Dissipative Explicit Algorithm

The new dissipative algorithm proposed here is a modified Newmark explicit method. Rayleigh damping is incorporated into the algorithm by modifying the equilibrium equation in the Newmark explicit formulation, such that

$$m a_{i+1} + \left[ (1 + \alpha) k + \frac{\rho}{\Delta t^2} m \right] d_{i+1} = f_{i+1} + \left[ \alpha k + \frac{\rho}{\Delta t^2} m \right] d_i$$

$$d_{i+1} = d_i + \Delta t v_i + \frac{\Delta t^2}{2} a_i \quad (7.10)$$

$$v_{i+1} = v_i + \frac{\Delta t}{2} [a_i + a_{i+1}]$$

By rearranging the equilibrium equation, we can see that the numerical damping in the modified algorithm is approximately  $k$ - and  $m$ - proportional. This is similar to Rayleigh

damping. By letting both  $\alpha$  and  $\rho$  equal to zero, we have the familiar Newmark explicit method, which has no dissipative property. When only  $\rho$  is equal to zero, we have the explicit  $\alpha$ -dissipation method [13]. When compared with the  $\alpha$ -dissipation method, the mass proportional damping in the modified algorithm provides additional freedom to adjust the distribution of damping ratios among the vibration modes. The advantage of this will be discussed later in this section. To obtain larger damping on the higher modes, we have to assume that  $\alpha$  is positive and  $\rho$  is less than or equal to zero. With these assumptions, the algorithm has the following numerical properties.

*Stability.* A numerical method is stable if a free-vibration response given by it will not grow without limit under any arbitrary initial conditions. The modified integration method is stable under the following conditions:

(i) For  $\alpha > 0$  and  $\rho \leq 0$ ,

$$\sqrt{-\frac{\rho}{\alpha}} \leq \Omega \leq \frac{1 + \sqrt{1 - (1 + \alpha)\rho}}{1 + \alpha} \quad (7.11a)$$

(ii) For  $\alpha = 0$  and  $\rho = 0$ ,

$$0 < \Omega \leq 2 \quad (7.11b)$$

in which  $\Omega = \omega \Delta t$ . The method is unstable if  $\alpha = 0$  and  $\rho < 0$ . Eq. (7.11b) is the stability condition for the Newmark Explicit Method. We will see next that for  $\Omega < \sqrt{-\rho/\alpha}$ , damping is negative and energy will be added into the response motion. For this reason, the method will be unstable. The derivation of the stability conditions can be found in Appendix D.

*Numerical Damping.* Numerical damping of the integration algorithm can be found by means of Eq. (3.20). Using the information in Appendix D, we obtain the following damping ratio equation and parameters:

$$\bar{\xi} = - \frac{\ln (1 - \alpha \Omega^2 - \rho)}{2 \Omega} \quad (7.12)$$

where

$$\bar{\Omega} = \arctan \left( \frac{B}{A} \right)$$

$$A = 1 - (1 + \alpha) \frac{\Omega^2}{2} - \frac{\rho}{2}$$

$$B = \left\{ \Omega^2 - \left[ (1 + \alpha) \frac{\Omega^2}{2} + \frac{\rho}{2} \right]^2 \right\}^{1/2}$$

From this equation, we know that damping is zero at  $\Omega = \sqrt{-\rho/\alpha}$ . For  $\Omega < \sqrt{-\rho/\alpha}$ , damping is negative and the solution becomes unstable. Thus,  $\sqrt{-\rho/\alpha}$  is the lower stability bound. By a proper combination of  $\alpha$  and  $\rho$ , we can specify an optimal frequency-damping relationship. See Fig. 7.7 for an illustration. The figure shows two sample curves governed by Eq. (7.12). Both curves have  $\sqrt{-\rho/\alpha}$  equal to 0.1, but have  $\alpha$  equal to 0.1 and 0.5, respectively. We can see that damping increases with increasing  $\alpha$ . In addition, by bringing  $\sqrt{-\rho/\alpha}$  closer to  $\omega_1 \Delta t$ , we can have a larger  $\bar{\xi}_n/\bar{\xi}_1$  ratio. With a larger  $\bar{\xi}_n/\bar{\xi}_1$  ratio, we can impose more severe dampings on the higher frequency modes, while leaving the fundamental frequency undamped or slightly damped.

The other property which may be of interest to the user is the period distortion caused by the algorithm. As shown in Appendix B, the Newmark explicit method will only have a small period shrinkage when  $\omega \Delta t$  is small. At low damping values, the modified algorithm is basically the same as the Newmark explicit method. The period distortion increases as damping increases. However, response becomes insignificant when large damping values are used.

### 7.3.3. Examples

In the first example, we try to further improve the two-degree-of-freedom simulation in Sec. 7.2.2, using numerical damping. After the equivalent energy compensation, significant high frequency noise can still be observed in the first few seconds of the force history, as

shown in Fig. 7.3. This may cause premature yielding or failure of the structure in a real test. Therefore, in addition to the energy compensation, we impose a large second mode damping to reduce the noise. By selecting  $\alpha$  and  $\rho$  to be 0.4208 and -0.005, respectively, we have  $\sqrt{-\rho/\alpha}$  equal to  $\omega_1 \Delta t$ . As a result,  $\bar{\xi}_1$  is 0 and  $\bar{\xi}_2$  is 15.6%. The result of this simulation is shown in Fig. 7.8. It indicates further removal of the high frequency noise. However, the displacement response, which is basically at the fundamental frequency, is reduced also, even though  $\bar{\xi}_1$  is equal to zero. This can be explained by the fact that the energy compensation in the previous example becomes excessive when the response is changed by numerical damping. We have to re-adjust the force correction vector to improve the result. Numerical damping can also be included in the equivalent hysteretic energy compensation, as long as the energy change caused by the damping is taken into account in the energy equation. This may be a better approach than doing them separately.

The second example is a two-story shear building which is inelastically deformed. The inelastic inter-story shear deformation relationships are modelled by the Menegotto-Pinto relation. The properties of the structure are shown in Fig. 7.9. Under mild deformations (i.e. when the structure is approximately linear elastic),  $\omega_1 \approx 11.2 \text{ sec}^{-1}$  and  $\omega_2 \approx 35.7 \text{ sec}^{-1}$ . A high frequency noise is introduced into the displacement response by simulated force errors of the energy-addition type. The comparison of the erroneous response with the correct one is shown in Fig. 7.10. We see that the response at the second degree of freedom is severely contaminated by the high frequency noise. The resulting hysteretic behavior becomes very different from the actual, as indicated by the lower graphs of Fig. 7.10. Integration step used is 0.02 sec. Finally, by letting  $\alpha$  and  $\rho$  be 0.4 and -0.016, respectively, we have  $\bar{\xi}_1 = 0.9\%$  and  $\bar{\xi}_2 = 13.6\%$ . The significantly improved result with these damping values is shown in Fig. 7.11. The displacement response observed is slightly larger than the correct response because of the remaining energy effect of the simulated errors, as the first mode damping is small.

#### 7.4. Comments

The equivalent hysteretic energy compensation method is designed to correct the systematic error effects. By this method, energy can be freely taken out from or added into any of the participating modes until the correct structural response is restored. The smaller or more consistent the errors are, the faster and easier will be the correction. Therefore, this method is efficient for correcting force-measurement errors which are caused by frictional forces. When errors are more irregular, compensation performed for one displacement history may not be adequate for the others. In that case, good judgment and many trials are required to decide upon the best force correction vector.

Numerical damping introduced into the Newmark explicit method is helpful for suppressing the spurious growth of high frequency responses. It is complementary to the energy compensation method. The number of iterations required in energy compensation may be reduced if high frequency noises are removed beforehand. However, care should be taken in selecting  $\sqrt{-\rho/\alpha}$ , which should not exceed  $\omega_1 \Delta t$ , as  $\omega_1$  decreases when a structure becomes nonlinear. When used with the energy compensation method, the energy dissipation due to numerical damping should also be included in the energy computation.

By using these correction methods, the error-propagation problems observed in the previous chapters can be significantly reduced. In addition, pseudodynamic testing of MDOF systems under adverse experimental conditions becomes more stable and reliable.

## CHAPTER 8

### CONCLUSIONS AND RECOMMENDATIONS

#### 8.1. Summary

Experimental error propagation in pseudodynamic testing has been thoroughly investigated in this report. The major sources of experimental errors are discussed. The errors are classified according to the sources, occurrence patterns, and their influences on experimental results. Three integration methods which were previously recommended for pseudodynamic testing are studied here in terms of their error-propagation behavior. They are the basic central difference method, the Newmark explicit method, and the summed form of the central difference method. Based on the error-propagation behavior, the reliability of the pseudodynamic method in testing linear elastic and inelastic structures is evaluated. The additional problems in MDOF testing are also identified. Analytical methods are developed for estimating error bounds in linear elastic testing. Furthermore, two numerical methods are proposed to improve experimental results and to prevent numerical instability in MDOF testing. They are the equivalent hysteretic energy compensation and the modified Newmark explicit algorithm which has adjustable numerical damping. The modified algorithm is recommended for all MDOF pseudodynamic tests.

From the results of this investigation, the characteristics of experimental errors and of their cumulative growth in pseudodynamic experiments can be summarized as follows:

- (1) According to the sources, experimental errors can be classified into three general categories: (i) displacement-control errors  $e_i^{dc}$ , (ii) displacement-measurement errors  $e_i^{dm}$ , and (iii) force-measurement errors  $e_i^{fm}$ . These errors amount to the total displacement- and force-feedback errors,  $e_i^d$  and  $e_i^f$ , which can be introduced into numerical computations. Displacement-feedback errors  $e_i^d$  can be avoided by using the computed displacement in the numerical algorithm instead of the measured one. This procedure has been analytically proved to be the more accurate approach for all three numerical algorithms studied. Force-feedback errors, which are contributed by  $e_i^{dc}$  and  $e_i^{fm}$ , are always



introduced into numerical computations. Therefore, they are totally responsible for the cumulative error growth in pseudodynamic experiments.

- (2) Two types of force-feedback errors can be identified: random and systematic errors. Systematic errors often result from poor performance of experimental equipment, inadequate instrumentation, or improper testing technique. They often have persistent energy changing effects. They can either dissipate energy from or add energy into a response motion, such that a pseudodynamic response can appear to be significantly damped or have unlimited growth (instability). No physical interpretation can usually be associated with random errors, except that they also cause some undesirable excitations during pseudodynamic testing.
- (3) Under the influence of force-feedback errors, the three numerical methods studied have identical error-propagation properties. Error propagation due to systematic errors is much more significant than that due to random errors. This is because of a resonance-like phenomenon associated with systematic errors. Generally, significant cumulative errors can occur in experimental results even though only relatively small systematic feedback errors are present. The cumulative growth of random errors can always be minimized by reducing integration time step  $\Delta t$ . However, the rate of systematic error growth with respect to time is not sensitive to  $\Delta t$ .
- (4) For both random and systematic errors, the rate of cumulative growth with respect to the number of integration steps depends on  $\omega\Delta t$ . The larger the  $\omega\Delta t$  is, the faster will be the cumulative error growth. Therefore, the higher frequencies of a MDOF structure are more susceptible to error propagation than the lower frequencies. If systematic errors of the energy-addition type are present, the high frequency modes of a system can be significantly excited so that numerical computations become unstable. Consequently, MDOF testing presents more severe error-propagation problems than SDOF tests. In general, the wider the frequency span of a system is, the more severe will be error propagation.

- (5) Error propagation in inelastic structural testing is studied with a simple elasto-plastic model. Inelastic deformations of this type do not impose additional problems on pseudodynamic testing. Instead, pseudodynamic results tend to be more accurate in inelastic testing. Accuracy increases with increasing displacement ductility. Therefore, the reliability criteria for linear elastic tests can be conservatively used to assess the accuracy of inelastic testing, as long as inelastic deformations are within reasonable range.

## 8.2. Recommendations for Pseudodynamic Testing

Pseudodynamic results can be significantly influenced by the cumulative effects of experimental feedback errors. Overall experimental results can be rendered totally unreliable, and numerical computations can become unstable if the feedback errors are not properly controlled. Fortunately, most of the systematic errors can be eliminated or reduced to insignificant levels by using appropriate instrumentations with proper calibration, reliable test apparatus, and good experimental techniques. To assess the significance of these errors prior to testing and mitigate their effects during testing, the following precautions and improvement methods are recommended.

### 8.2.1. Preliminary System Check

Possible sources of experimental errors must be first identified before any test. Some of these are discussed in Chapter 2 of this report. Generally, the presence of any significant systematic errors can be easily detected with some preliminary tests. The following checks can be carried out to assess the accuracy of the pseudodynamic system:

- (1) Force-feedback errors are contributed by both displacement-control errors  $e_i^{dc}$  and force-measurement errors  $e_i^{fm}$ . Most of the displacement-control errors, especially those of the energy-addition type, can be observed from the discrepancy between the computed and the measured displacements. This discrepancy can be monitored during some trial pseudodynamic tests. By computing the Fourier spectrum for the monitored error signals,

systematic errors can be identified by peaks located at the natural frequencies of the structural system. The accuracy of displacement control can also be checked by imposing a series of simple displacement increments with the pseudodynamic control system. Generally, most of the displacement-control errors and instability sources can be identified before any major test.

- (2) Preliminary pseudodynamic testing within the linear elastic range is always recommended before any destructive test. Linear elastic pseudodynamic results should closely match analytical results obtained with appropriate structural models. Significant discrepancy between the two indicates the presence of experimental errors. It must be noted that poor experimental results in the elastic range do not always imply poor results in inelastic testing. Relative errors are approximately inversely proportional to structural displacements developed. The larger the inelastic displacement is, the more accurate will be the result. If results are accurate within the elastic range, then any further inelastic testing should be reliable as well, as far as experimental error propagation is concerned.
- (3) During preliminary testing, measurement of the equivalent hysteretic energy errors, as described in Chapter 7, is desirable. It provides quantitative information about error magnitudes and the amount of compensation required to improve the result.

Most experimental inaccuracies can be detected with the above precautions. It should be noted, however, that a small amount of energy dissipation is usually expected because of local yielding or frictional damping in a test structure. Prior to any test, all systematic errors should be reduced as much as possible by adjustment of test equipment, modification of testing techniques, or use of different apparatus if necessary.

### **8.2.2. Improvement Methods**

Experimental error effects which remain after the preliminary checks and corrections can be compensated for or eliminated by the two numerical methods discussed in Chapter 7:

- (1) The equivalent hysteretic energy compensation can be used to correct persistent energy modification effects. It is especially recommended for correcting exceedingly large energy dissipation due to frictional damping. However, erroneous high frequency oscillations can be suppressed more efficiently by using numerical dissipation.
- (2) The spurious growth of the high frequency modes of a MDOF system can be conveniently suppressed by means of the modified Newmark explicit algorithm, which has numerical dissipation. The numerical damping can be adjusted in such a way that the high frequency modes are severely damped, while the lower frequency modes are only moderately affected.

### 8.3. Concluding Remarks

Pseudodynamic testing is a feasible experimental method from both theoretical and practical viewpoints. Reliable pseudodynamic results can be obtained by means of good instrumentations and appropriate test apparatus, as well as efficient error compensation or removal techniques. From our investigation, we can conclude that the propagation of experimental errors through numerical computations is a major problem in pseudodynamic testing.

Additional studies of error propagation in MDOF inelastic systems should be done (though not expected to be a problem). Verification tests should also be performed to compare pseudodynamic test results with shaking table test results. Furthermore, the efficiency of the error control methods in actual testing should be evaluated, and other alternatives should be studied. Therefore, identification of experimental errors in complicated pseudodynamic testing, improvement of instrumentation techniques, selection of good performance equipments, and refinements of numerical schemes should be the main objectives of future researches.

## REFERENCES

1. Shing, P. B. and Mahin, S. A., " Pseudodynamic Test Method for Seismic Performance Evaluation: Theory and Implementation," Earthquake Engineering Research Center, University of California, Berkeley. (in preparation)
2. Takanashi, K., et al., " Nonlinear Earthquake Response Analysis of Structures by a Computer-Actuator On-line System," *Bull. of Earthquake Resistant Structure Research Center*, Institute of Industrial Science, University of Tokyo, No. 8, 1975.
3. Takanashi, K., et al., " Inelastic Response of H-Shaped Columns to Two Dimensional Earthquake Motions," *Bull. of Earthquake Resistant Structure Research Center*, Institute of Industrial Science, University of Tokyo, No. 13, 1980.
4. Okada, T., et al., " Nonlinear Earthquake Response of Equipment System Anchored on R/C Building Floor," *Bull. of Earthquake Resistant Structure Research Center*, Institute of Industrial Science, University of Tokyo, No. 13, 1980.
5. Watabe, M., et al., " Feasibility of Pseudo-Dynamic Testing System," *Progress Report on U.S.-Japan Large Scale Aseismic Experiments for Building Structures*, Building Research Institute, Ministry of Construction, Thirteenth Joint Meeting, U.S.-Japan Panel on Wind and Seismic Effects, Tsukuba, 1981.
6. Okamoto, S., et al., " A Progress report on the Full-Scale Seismic Experiment of A Seven Story Reinforced Concrete Building," Building Research Institute, Ministry of Construction, Tsukuba, 1982.
7. Mahin, S. A. and Williams, M. E., " Computer Controlled Seismic Performance Testing," *Second ASCE-EMD Specialty Conference on Dynamic Response of Structures*, Atlanta, Ga., Jan. 1981.
8. Powers, W. F., " Preliminary Analysis of the Computer-Actuator On-Line System Difference Equation," University of Michigan, Ann Arbor, June 1979.
9. McClamroch, N. H., Serakos, J., and Hanson, R. D., " Design and Analysis of the Pseudo-Dynamic Test Method," *UMEE 81R3*, University of Michigan, Ann Arbor, Sept. 1981.
10. Okada, T., " Computer-Actuator On-Line System at Institute of Industrial Science, University of Tokyo, with Emphasis on Numerical Integration Methods," *A Brief Note Submitted to Session 2, First Planning Group Meeting, U.S.-Japan Cooperative Research Program Utilizing Large-Scale Testing*, Sept. 1977.
11. Newmark, N. M., " A Method of Computation for Structural Dynamics," *Journal of the Engineering Mechanics Division, ASCE*, No. EM3, Vol. 85, July 1959.
12. Bathe, K. and Wilson, E. L., *Numerical Methods in Finite Element Analysis*, Prentice Hall, 1976.

13. Hilber, H. M., Hughes, T. J. R., and Taylor, R., L., " Improved Numerical Dissipation for Time Integration Algorithms in Structural Dynamics," *Earthquake Engineering and Structural Dynamics*, Vol. 5, 283-292, 1977.
14. Dahlquist, G., Björck A., and Anderson, N., *Numerical Methods*, Prentice Hall, 1974.
15. Conte, S. D. and de Boor, C., *Elementary Numerical Analysis*, McGraw Hill, Third Edition, 1980.
16. Clough, R. W. and Penzien, J., *Dynamics of Structures*, McGraw Hill, 1975.
17. Wilson, E. L., " CAL 78," *Report No. UC SESM 79-1*, University of California, Berkeley, Nov. 1978.
18. Bertero, V. V., Mahin, S. A., and Herrera, R. A., "Aseismic Design Implications of Near-Fault San Fernando Earthquake Records," *Earthquake Engineering and Structural Dynamics*, Vol. 6, 31-42, 1978.

	Basic Central Difference	Newmark Explicit	Summed-Form Central Difference
$\nu$	0	1	1
$\mathbf{x}_i$	$\{d_i, d_{i-1}\}^T$	$\{d_i, v_i, a_i\}^T$	$\{d_i, z_i\}^T$
$\mathbf{D}$	$\begin{bmatrix} 2 & -1 \\ 1 & 0 \end{bmatrix}$	$\begin{bmatrix} 1 & \Delta t & \frac{\Delta t^2}{2} \\ 0 & 1 & \frac{\Delta t}{2} \\ 0 & 0 & 0 \end{bmatrix}$	$\begin{bmatrix} 1 & \Delta t \\ 0 & 1 \end{bmatrix}$
$\mathbf{S}$	$\{\omega^2 m, 0\}$	$\{\omega^2 m, 0, 0\}$	$\{\omega^2 m, 0\}$
$\mathbf{l} = \mathbf{L}$	$\{\frac{\Delta t^2}{m}, 0\}^T$	$\{0, \frac{\Delta t}{2m}, \frac{1}{m}\}^T$	$\{0, \frac{\Delta t}{m}\}^T$
$\mathbf{A}$	$\begin{bmatrix} 2-\omega^2\Delta t^2 & -1 \\ 1 & 0 \end{bmatrix}$	$\begin{bmatrix} 1 & \Delta t & \frac{\Delta t^2}{2} \\ -\frac{\omega^2\Delta t}{2} & 1-\frac{\omega^2\Delta t^2}{2} & \frac{\Delta t-\omega^2\Delta t^3}{2} \\ -\omega^2 & -\omega^2\Delta t & -\frac{\omega^2\Delta t^2}{2} \end{bmatrix}$	$\begin{bmatrix} 1 & \Delta t \\ -\omega^2\Delta t & 1-\omega^2\Delta t^2 \end{bmatrix}$

Table 3.1 Characteristic Matrices and Vectors of the Explicit Integration Algorithms

	Basic Central Difference	Summed-Form Central Difference & Newmark Explicit
$a_{1i}$	$2 e_i^d$	$e_i^d$
$a_{2i}$	$\frac{2 A - 1}{B} e_i^d$	$\frac{A - 1}{B} e_i^d$
$b_{1i}$	$2 (1 - A) e_i^{rd}$	0
$b_{2i}$	$\frac{2 (1 - A) A}{B} e_i^{rd}$	$\frac{2 (1 - A)}{B} e_i^{rd}$

Table 3.2 The Parameters for the Error-Propagation Equations of the Explicit Integration Algorithms



No. of Steps $n$	Harmonic Error Amplification Factor $H_j$		Cumulative Error Bound by Each Harmonic (in) $2  c_j  H_j$		Total Cumulative Error Bound (in) $2 \sum  c_j  H_j$
	$\beta_j=0.991$	$\beta_j=1.013$	$\beta_j=0.991$	$\beta_j=1.013$	
0	0	0	0	0	0
100	19.4	19.3	0.016	0.023	0.039
200	38.0	37.1	0.031	0.044	0.075
300	55.4	52.8	0.045	0.062	0.107
400	71.3	65.2	0.058	0.077	0.135
500	85.1	73.6	0.069	0.087	0.156
600	96.4	77.6	0.078	0.092	0.170
700	104.8	76.8	0.085	0.091	0.176

Table 4.1 Cumulative Error Bound due to Two Major Harmonics Near Resonance Frequency  
( $\omega = 18.91 \text{ sec}^{-1}$ ,  $\Delta t = 0.02 \text{ sec}$ , the example in Fig. 4.5)

Stiffness Matrix **k**  
(kips/in)

759.3	-770.0	13.03	-2.683	0.5259	-0.1135
-770.0	1550	-799.5	23.10	-4.499	0.9682
13.03	-799.5	1754	-997.4	36.15	-7.753
-26.83	23.10	-997.4	2116	-1179	47.43
0.5259	-4.499	36.15	-1179	2556	-1457
-0.1135	0.9682	-7.753	47.43	-1457	2504

Table 5.1 Stiffness Matrix of a Six-Story K-Braced Steel Frame

Vibration Modes $m$	Frequencies $\omega$ (sec <sup>-1</sup> )	$\omega \Delta t$ ( $\Delta t = 0.01$ sec)
1	7.76	0.078
2	21.0	0.210
3	34.4	0.344
4	45.8	0.458
5	54.9	0.549
6	66.7	0.667

Table 5.2 Modal Frequencies of a Six-Story K-Braced Steel Frame

Normalized Mode Shapes $\phi_m$ ( $\phi_m^T \phi_m = 1$ )					
$m = 1$	$m = 2$	$m = 3$	$m = 4$	$m = 5$	$m = 6$
-0.5784	0.5398	0.4613	0.3731	-0.1478	0.0141
-0.5315	0.2193	-0.2625	-0.6476	0.4210	-0.0622
-0.4421	-0.2277	-0.5698	0.0968	-0.6172	0.1943
-0.3398	-0.4837	-0.0989	0.4904	0.4500	-0.4448
-0.2328	-0.5046	0.4161	-0.1042	0.1702	0.6915
-0.1335	-0.3465	0.4591	-0.4250	-0.4342	-0.5312

Table 5.3 Normalized Mode Shapes of a Six-Story K-Braced Steel Frame

Random Error Amplification Factor for Each Mode $m$ $ \phi_m J_m $						Root-Sum-Square Factor $= \frac{ \bar{e}_n _{\max}}{S_e}$
$m = 1$	$m = 2$	$m = 3$	$m = 4$	$m = 5$	$m = 6$	
2.86	7.21	10.2	11.1	5.34	0.630	17.8
2.63	2.93	5.80	19.3	15.2	2.78	25.7
2.19	3.04	12.6	2.88	22.3	8.70	27.4
1.68	6.46	2.18	14.6	16.3	19.9	30.3
1.15	6.74	9.19	3.10	6.15	31.0	33.7
0.660	4.63	10.1	12.6	15.7	23.8	33.1

Table 5.4 Modal Contributions of Cumulative Errors in a Six-Story K-Braced Steel Frame  
(at  $t = 20$  sec,  $\Delta t = 0.01$  sec)

Stiffness Matrix **k**  
(10<sup>4</sup> kips/in)

4.195	-8.848	5.291	-2.429	3.795	-2.240
-8.848	19.74	-12.55	5.133	-7.472	4.029
5.291	-12.55	9.339	-4.344	4.250	-1.567
-2.429	5.133	-4.344	4.382	-3.693	0.5780
3.795	-7.472	4.250	-3.693	6.511	-4.435
-2.240	4.029	-15.67	0.5780	-4.435	7.435

Table 5.5 Stiffness Matrix of a Six-Story Reinforced Concrete Structure

Vibration Modes $m$	Frequencies $\omega$ (sec <sup>-1</sup> )	$\omega\Delta t$ ( $\Delta t = 0.005$ sec)
1	7.76	0.039
2	26.1	0.131
3	57.6	0.288
4	98.9	0.494
5	144	0.721
6	312	1.561

Table 5.6 Modal Frequencies of a Six-Story Reinforced Concrete Structure

Normalized Mode Shapes $\phi_m$ ( $\phi_m^T \phi_m = 1$ )					
m = 1	m = 2	m = 3	m = 4	m = 5	m = 6
0.6509	-0.5981	-0.3219	-0.112	0.0051	-0.3203
0.5303	-0.0039	0.2545	0.3502	-0.1872	0.7045
0.4115	0.3541	0.6324	0.0085	0.3080	-0.4587
0.2925	0.4660	-0.2388	-0.7633	-0.0759	0.2279
0.1830	0.5184	-0.4440	0.4716	-0.4192	-0.3203
0.0821	0.1758	-0.4214	0.2449	0.8299	0.1901

Table 5.7 Normalized Mode Shapes of a Six-Story Reinforced Concrete Frame

Random Error Amplification Factor for Each Mode $m$ $ \phi_m J_m $						Root-Sum-Square Factor $= \frac{ \bar{e}_n _{\max}}{S_e}$
m = 1	m = 2	m = 3	m = 4	m = 5	m = 6	
2.27	7.02	8.38	5.07	0.353	71.5	72.6
1.85	0.05	6.63	16.0	12.9	157.	159.
1.44	4.16	16.5	0.388	21.3	102.	106
1.02	5.47	6.22	34.8	5.25	50.9	62.5
0.64	6.09	11.6	21.5	29.0	71.5	81.2
0.29	2.06	11.0	11.2	57.4	42.5	73.1

Table 5.8 Modal Contributions of Cumulative Errors in a Six-Story Reinforced Concrete Structure  
(at  $t = 20$  sec,  $\Delta t = 0.005$  sec)

Trial # $N$	DOF $i$	$\bar{e}_i^f$ Samples					Average Errors $E(\bar{e}_i^f)$	Cumulative Corrections $-\sum_N E(\bar{e}_i^f)$
		1	2	3	4	5		
0	1	0.0006	0.0064	0.0083	0.0094	0.0113	0.0072	-0.0072
	2	-0.0217	-0.0137	-0.0107	-0.0076	-0.0075	-0.0122	0.0122
1	1	-0.0014	0.0007	0.0052	0.0009	0.0047	0.0020	-0.0092
	2	-0.0218	-0.0122	-0.0095	-0.0049	-0.0050	-0.0107	0.0229
2	1	-0.0302	0.0053	-0.0057	-0.0062	-0.0056	-0.0085	-0.0007
	2	-0.0125	-0.0141	-0.0041	-0.0037	-0.0017	-0.0072	0.0301
3	1	0.0002	0.0005	-0.0000	0.0005	0.0020	0.0006	-0.0013
	2	-0.0132	-0.0035	-0.0033	-0.0026	-0.0036	-0.0052	0.0353
4	1	-0.0030	-0.0023	-0.0018	-0.0016	-0.0005	-0.0018	0.0005
	2	-0.0091	-0.0023	-0.0026	-0.0028	-0.0012	-0.0036	0.0389
5	1	0.0010	0.0022	0.0003	0.0010	0.0016	0.0012	-0.0007
	2	-0.0118	-0.0069	-0.0033	-0.0017	-0.0003	-0.0048	0.0437
6	1	-0.0093	-0.0078	-0.0039	-0.0031	-0.0054	-0.0059	0.0052
	2	-0.0085	-0.0025	-0.0016	0.0009	0.0002	-0.0023	0.0460
7	1	-0.0044	-0.0043	0.0056	0.0062	0.0065	0.0036	0.0016
	2	-0.0015	-0.0016	-0.0018	-0.0022	-0.0026	-0.0019	-0.0479
8	1	0.0019	0.0039	0.0031	0.0023	0.0017	0.0026	STOP
	2	-0.0016	-0.0029	-0.0014	-0.0011	-0.0015	-0.0017	

Table 7.1 Iterative Correction in a Two-Degree-of-Freedom System  
by the Equivalent Hysteretic Energy Compensation Method



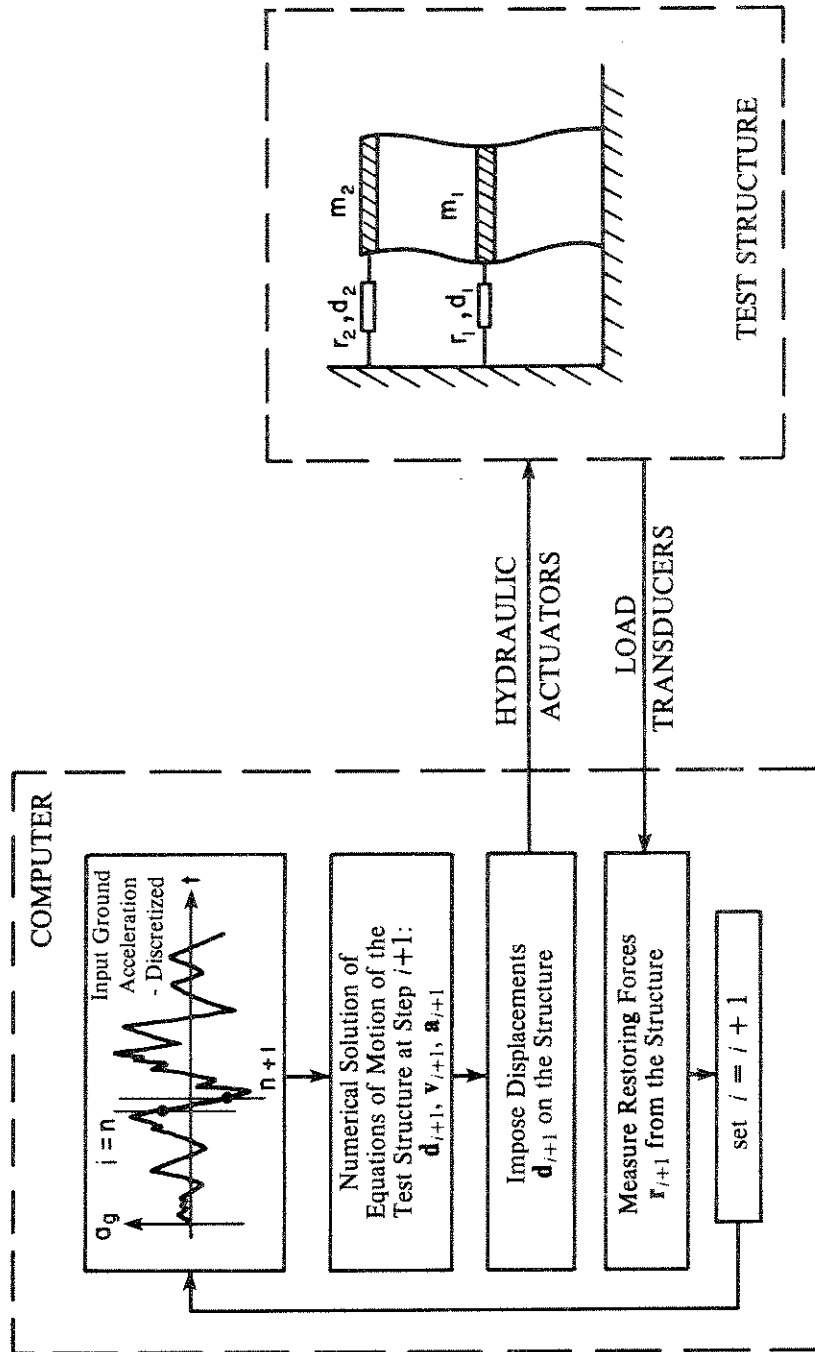


Fig. 1.1 Basic Experimental Scheme of the Pseudodynamic Method

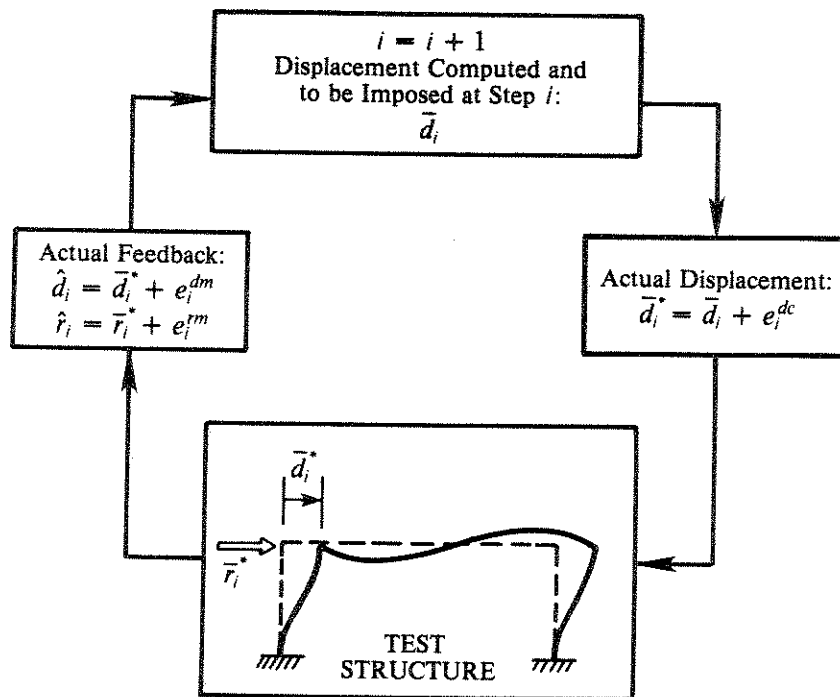


Fig. 2.1 Sources of Experimental Errors in Pseudodynamic Testing

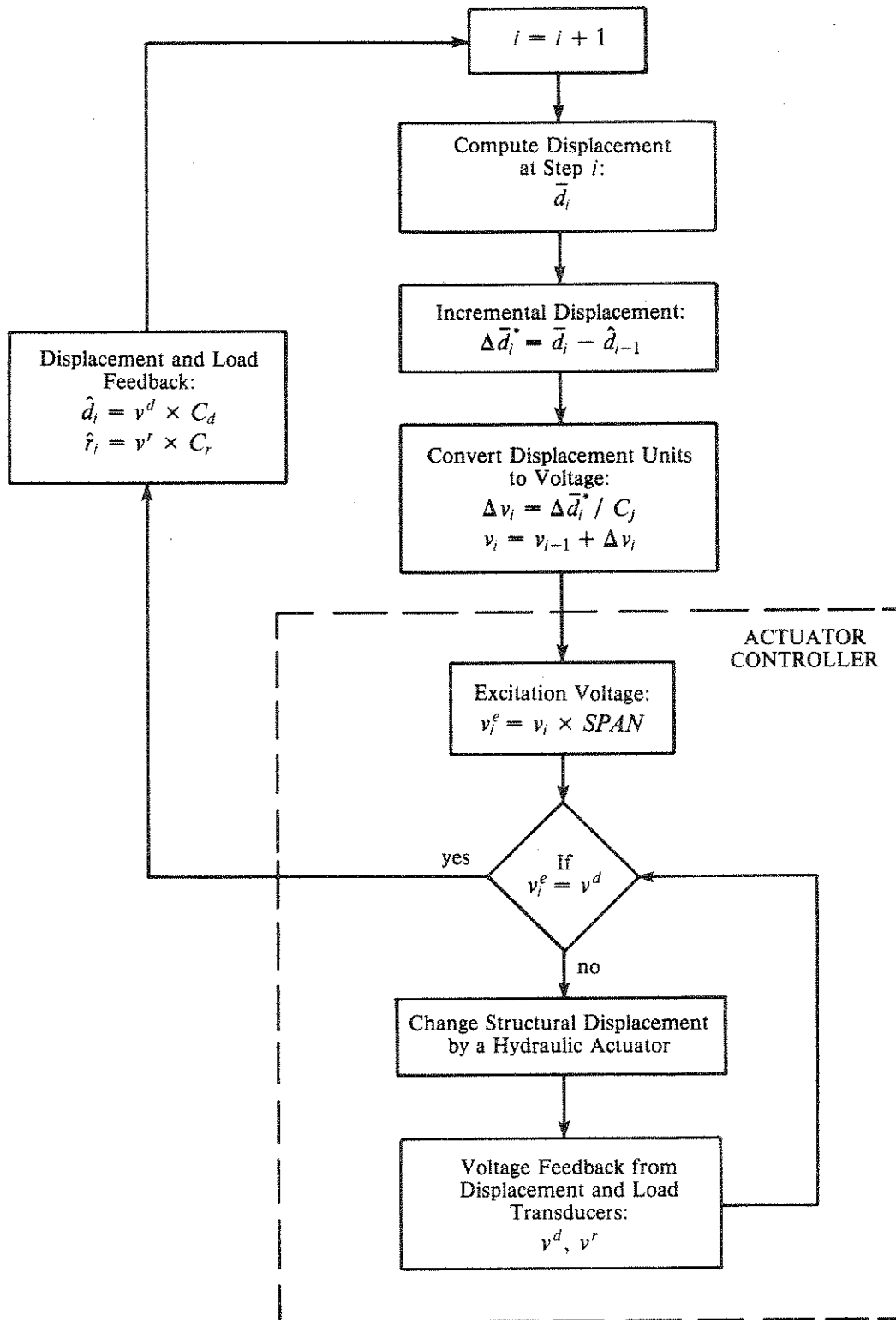
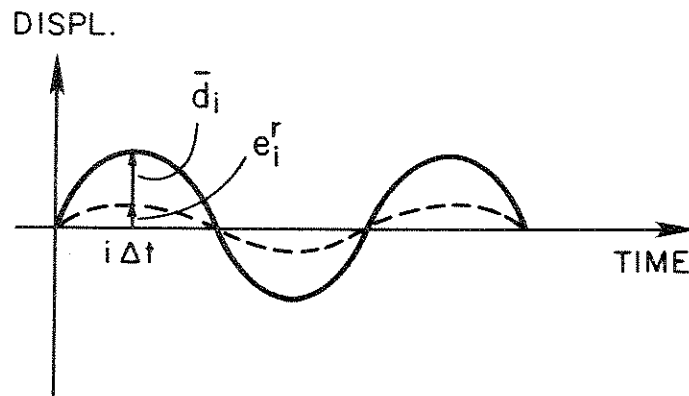
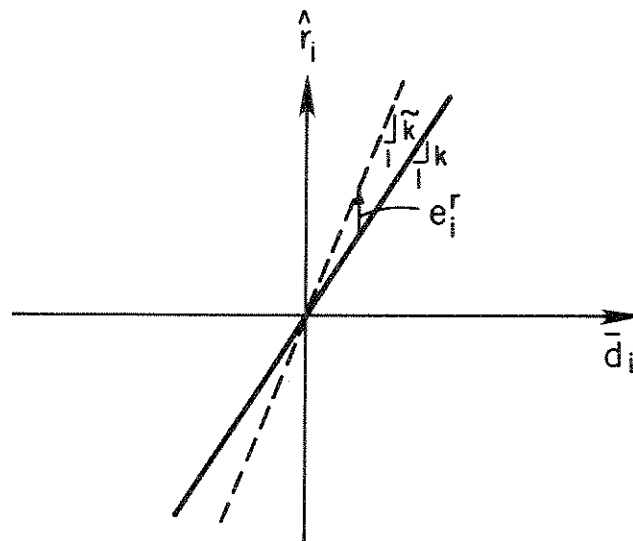


Fig. 2.2 Displacement Control Diagram of the Pseudodynamic System at Berkeley ( $C_j$ : actuator displ. calib.,  $C_d$ : displ. transducer calib., and  $C_r$ : load transducer calib.;  $C_j = C_d \times SPAN$ )

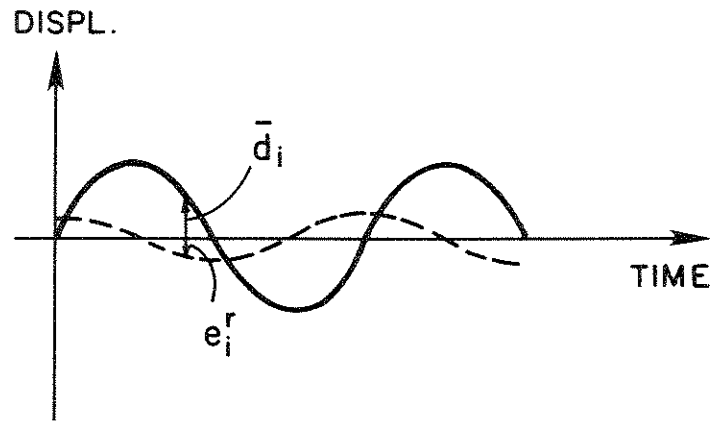


(a) Relation of Force-Feedback Errors ( $e_i^r$ ) with Computed Displacements ( $\bar{d}_i$ )

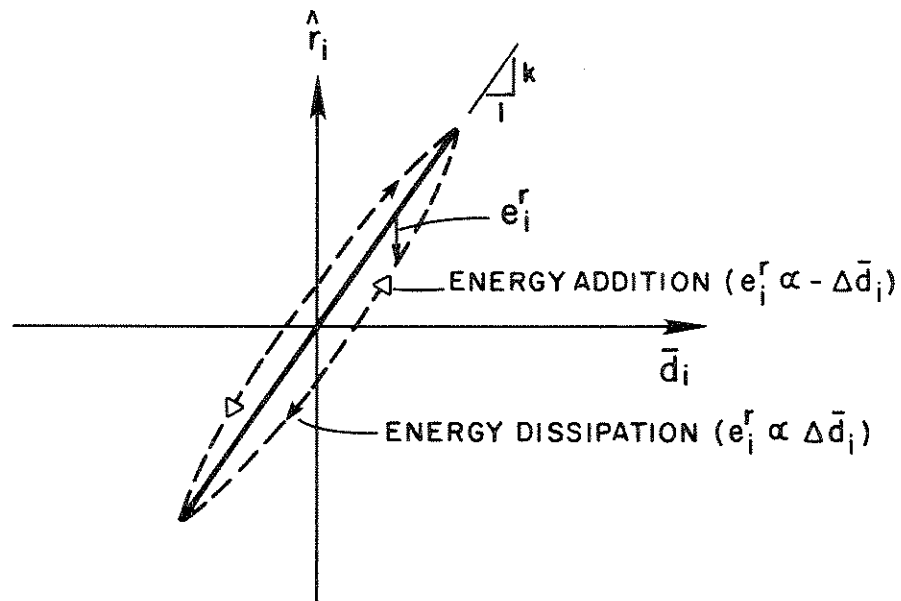


(b) Apparent Stiffness ( $\tilde{k}$ ) vs Actual Stiffness ( $k$ ) of a System

Fig. 2.3 Systematic Error Effects due to Mis-Calibration of Control and Measurement Transducers

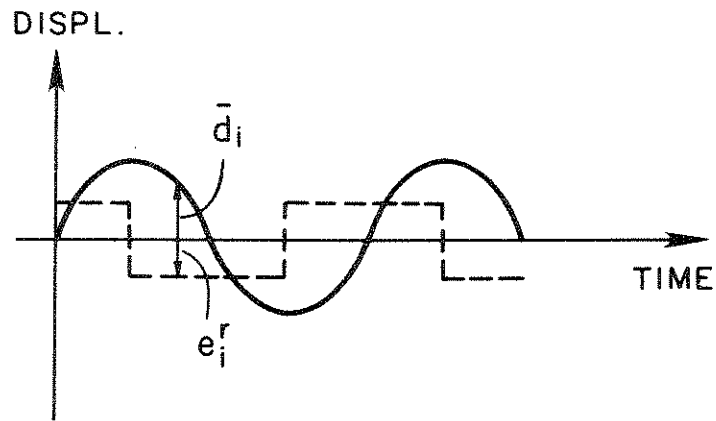


(a) Relation of Force-Feedback Errors ( $e_i^r$ ) with Computed Displacements ( $\bar{d}_i$ )

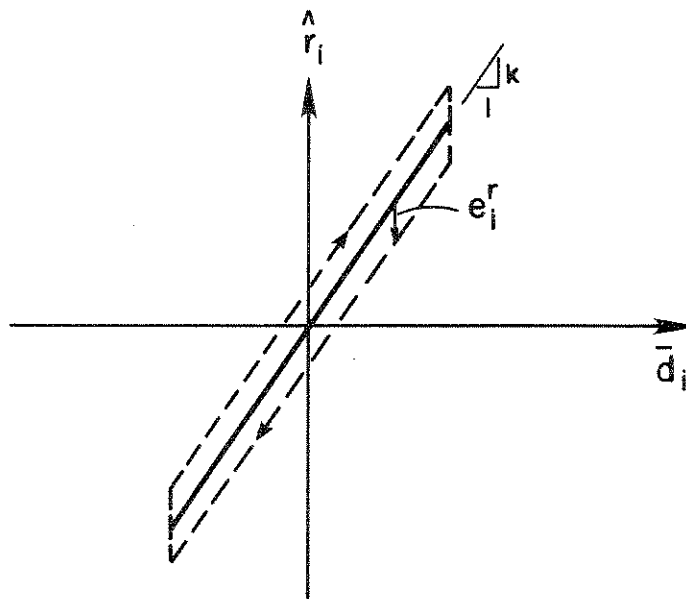


(b) Apparent Energy-Changing Force-Deformation Hysteresis

Fig. 2.4 Systematic Error Effects due to Mis-Calibration of Actuator Displacement

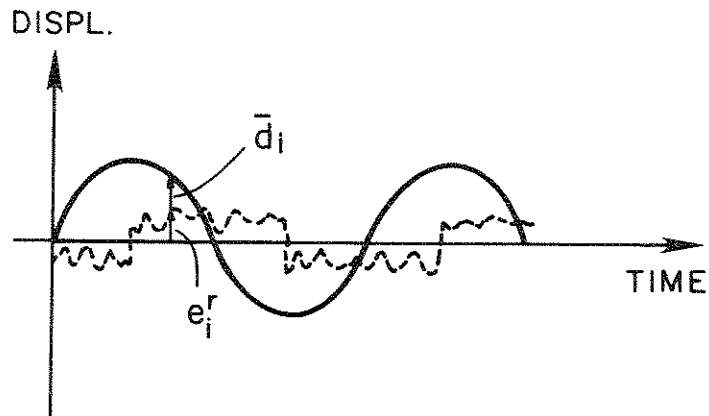


(a) Relation of Force-Feedback Errors ( $e_i^r$ ) with Computed Displacements ( $\bar{d}_i$ )

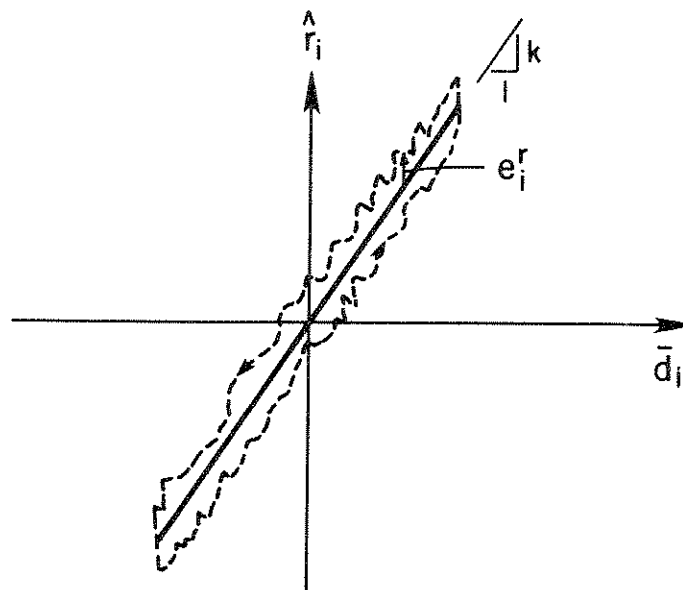


(b) Apparent Energy-Dissipating Force-Deformation Hysteresis

Fig. 2.5 Systematic Error Effects due to a Constant Frictional Influence on Force Feedback

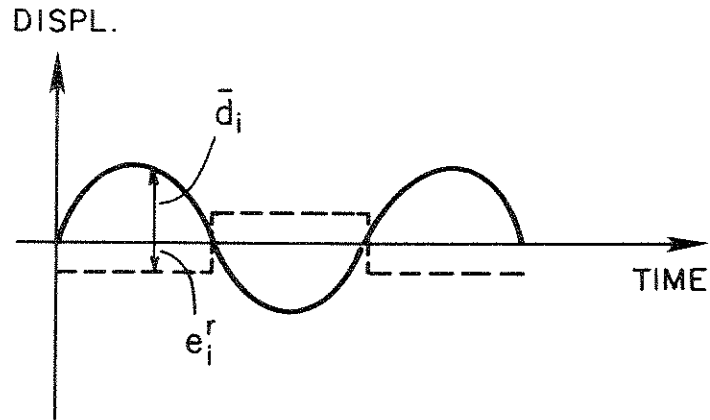


(a) Relation of Force-Feedback Errors ( $e_i^r$ ) with Computed Displacements ( $\bar{d}_i$ )

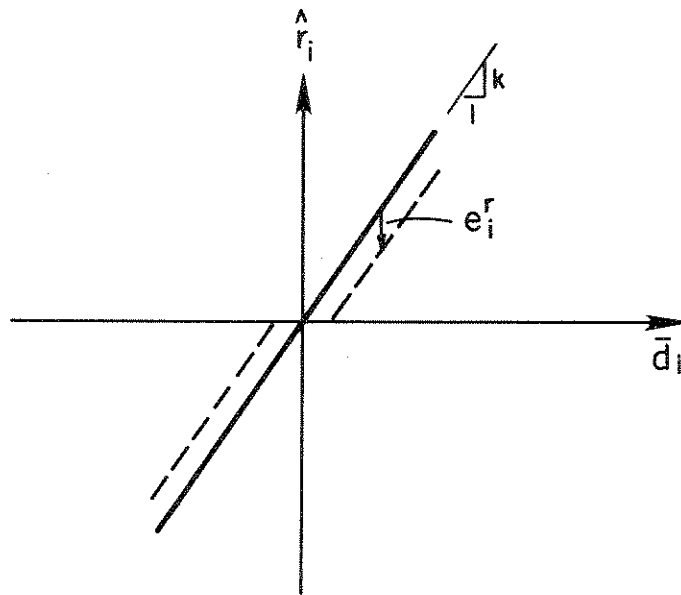


(b) Apparent Energy-Adding Force-Deformation Hysteresis

Fig. 2.6 Systematic Error Effects due to Truncation Errors in the A/D Conversions of Displacement-Control Signals



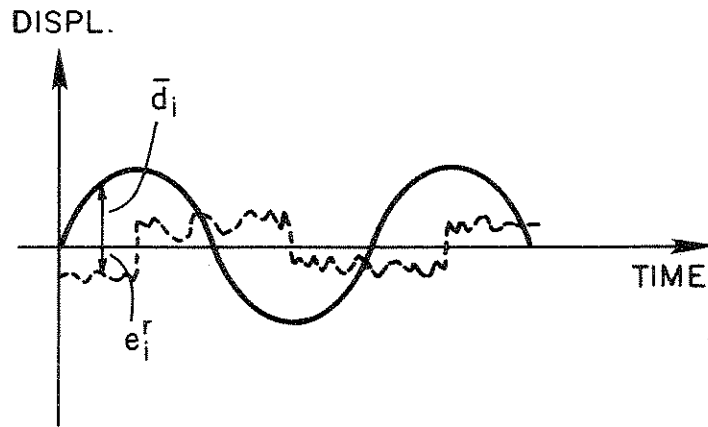
(a) Relation of Force-Feedback Errors ( $e_i^r$ ) with Computed Displacements ( $\bar{d}_i$ )



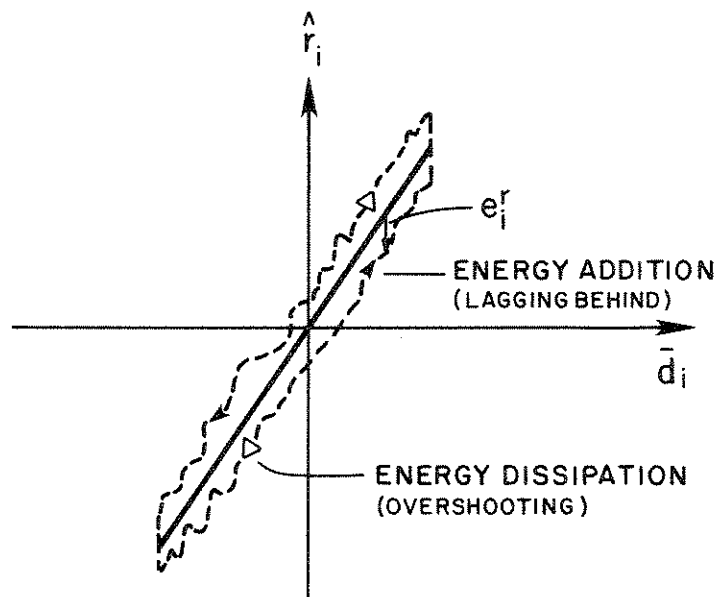
(b) Apparent Discontinuity of Stiffness

Fig. 2.7 Systematic Error Effects due to Idealized Slip Movement of System Support at Load Reversal



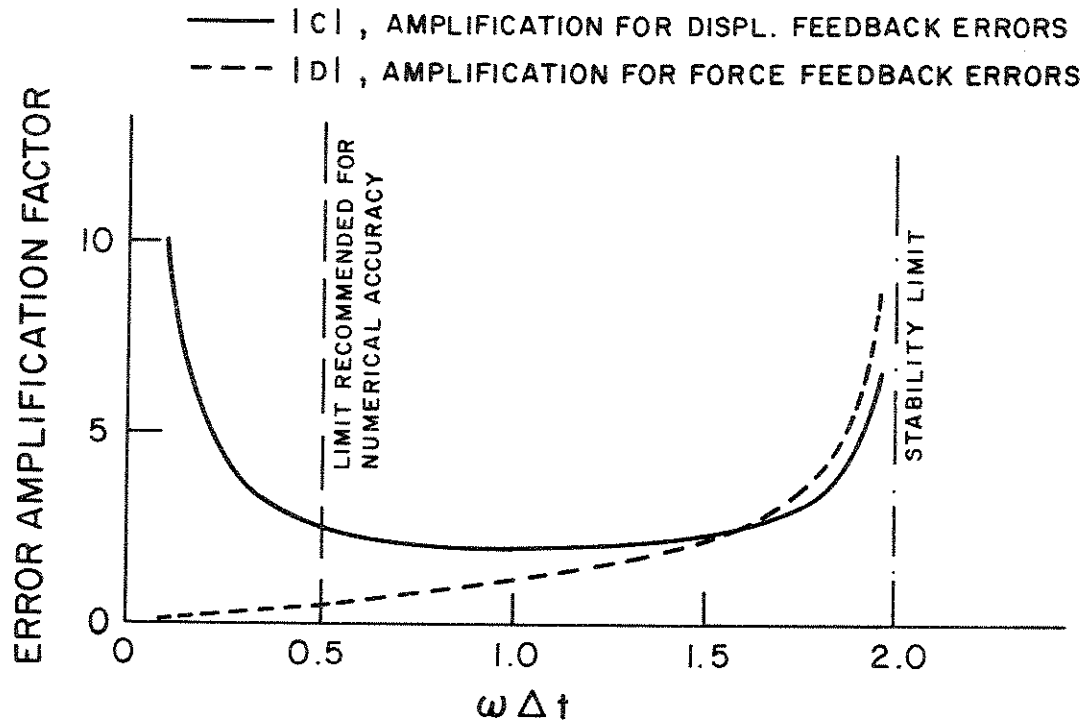


(a) Relation of Force-Feedback Errors ( $e_i^r$ ) with Computed Displacements ( $\bar{d}_i$ )

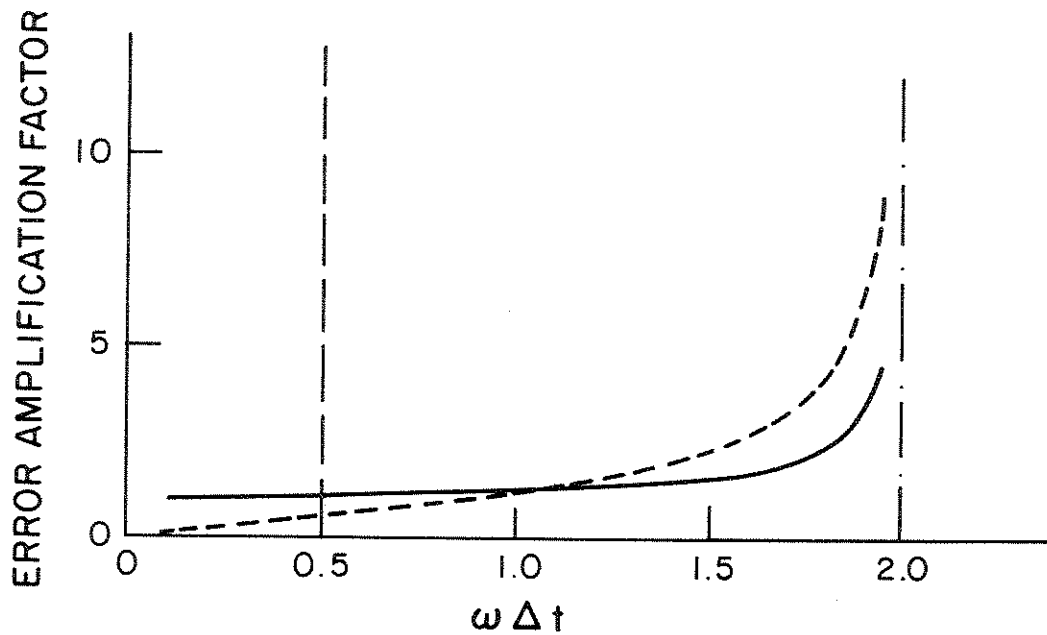


(b) Apparent Energy-Changing Force-Deformation Hysteresis

Fig. 2.8 Systematic Error Effects due to Persistent Overshooting or Lagging-Behind of Actuator Motion



(a) Basic Central Difference Method



(b) Summed-Form Central Difference  
and Newmark Explicit Methods

Fig. 3.1 Comparisons of Cumulative Error Growth Among  
Different Integration Methods

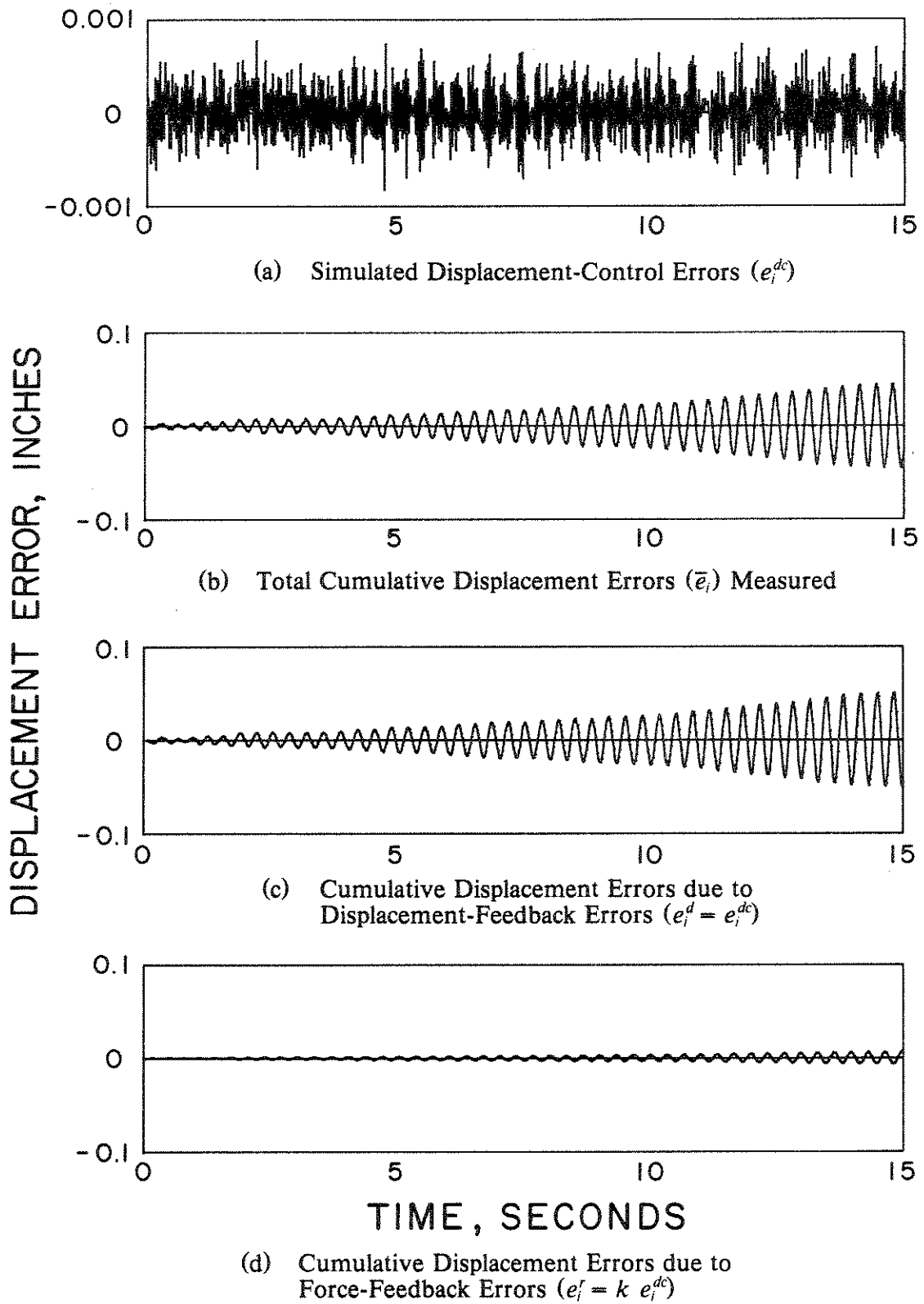


Fig. 3.2 Error Propagation in the Basic Central Difference Method  
 $(\omega = 18.91 \text{ sec}^{-1}, \Delta t = 0.02 \text{ sec})$

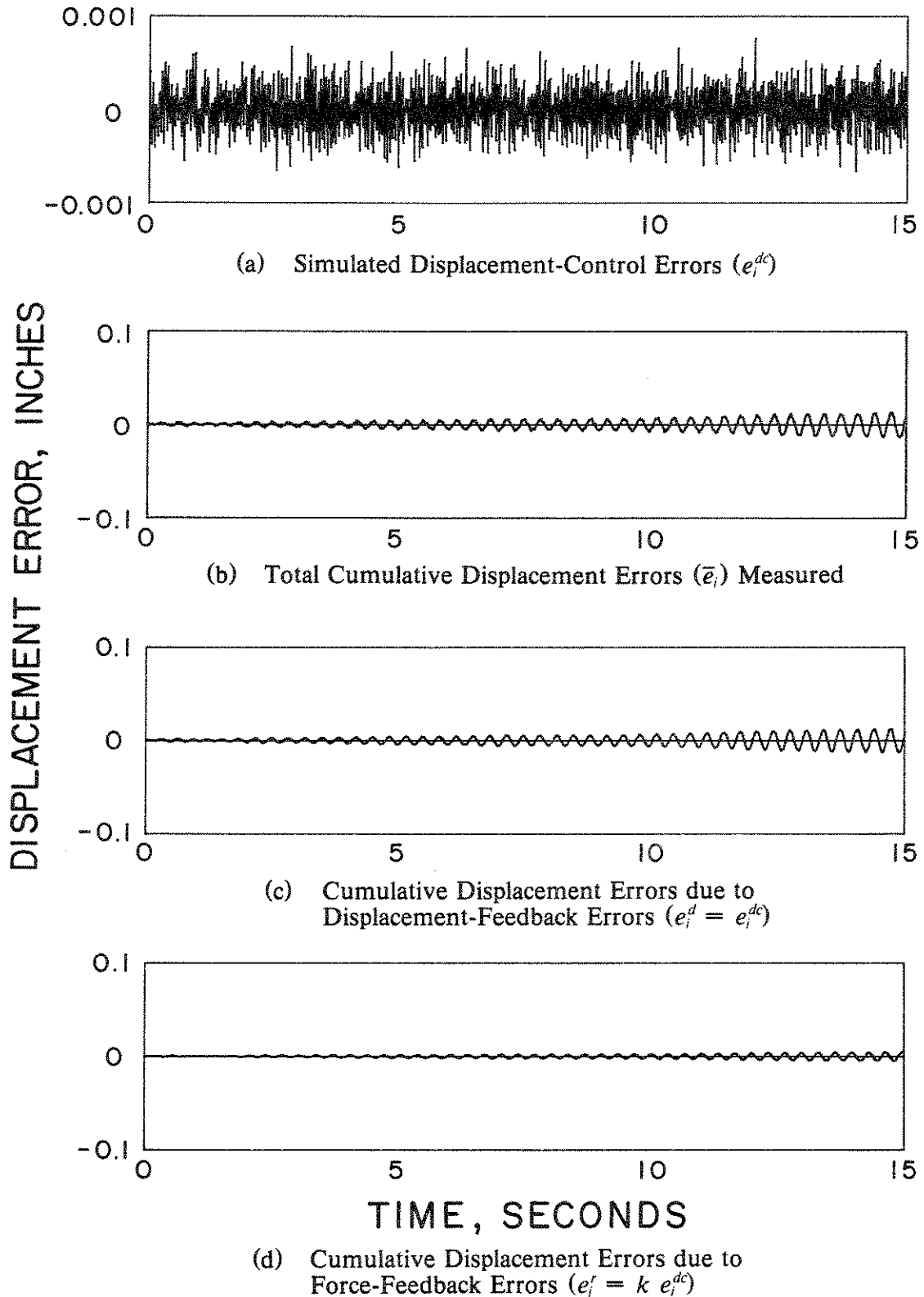


Fig. 3.3 Error Propagation in the Newmark Explicit Method  
 $(\omega = 18.91 \text{ sec}^{-1}, \Delta t = 0.02 \text{ sec})$

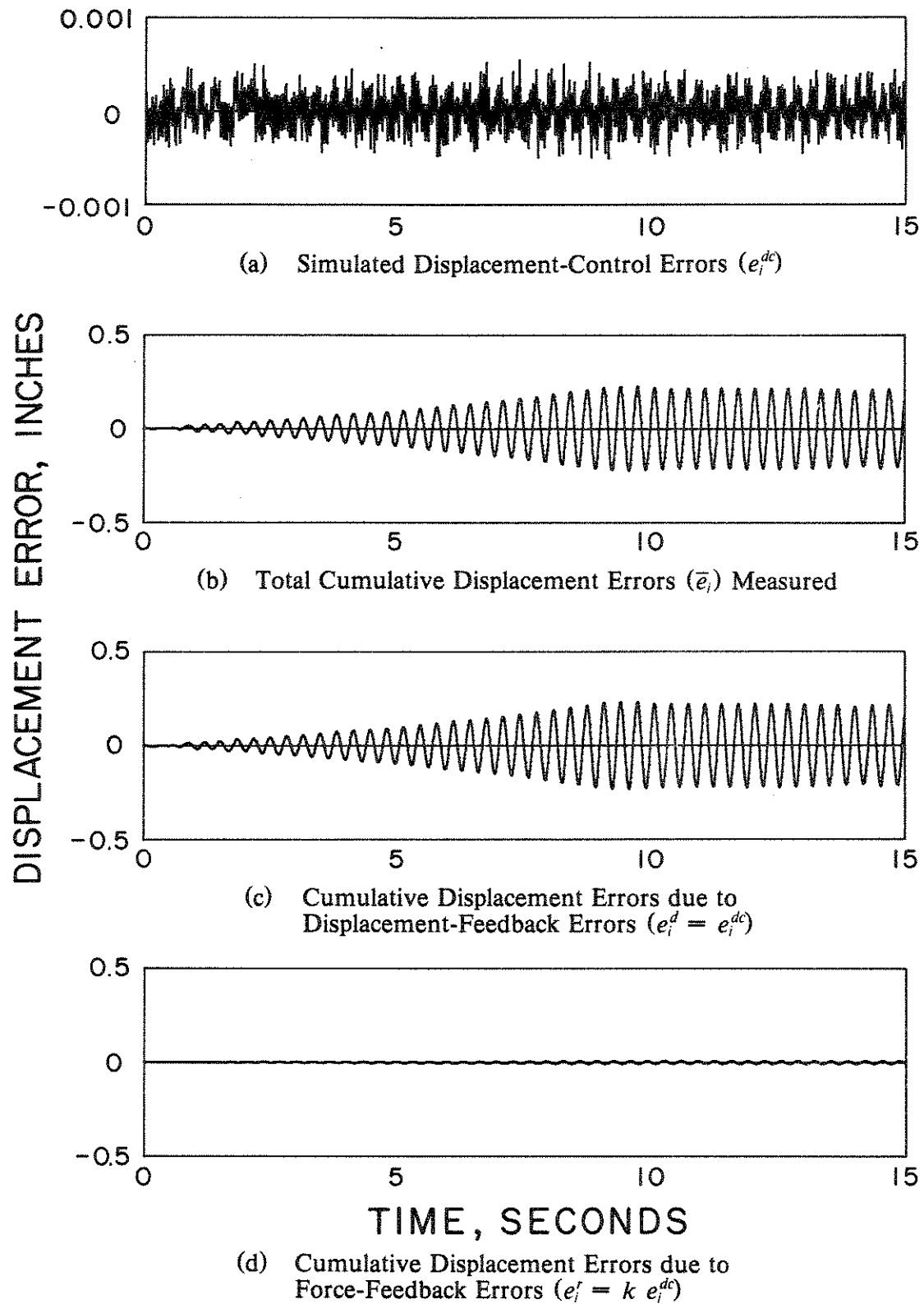


Fig. 3.4 Error Propagation in the Basic Central Difference Method  
 $(\omega = 18.91 \text{ sec}^{-1}, \text{ and } \Delta t = 0.01 \text{ sec})$

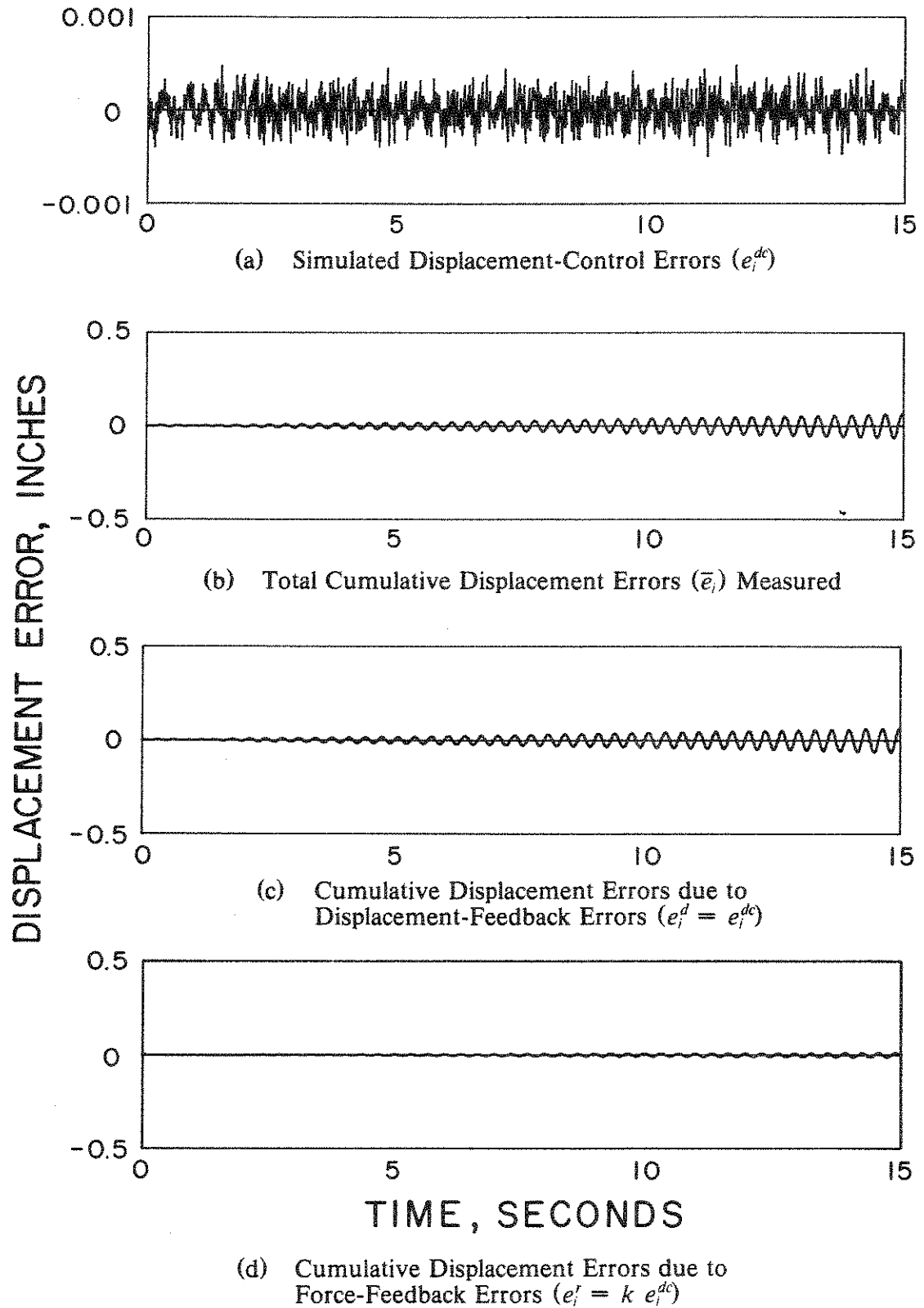


Fig. 3.5 Error Propagation in the Newmark Explicit Method  
 $(\omega = 18.91 \text{ sec}^{-1}, \Delta t = 0.01 \text{ sec})$

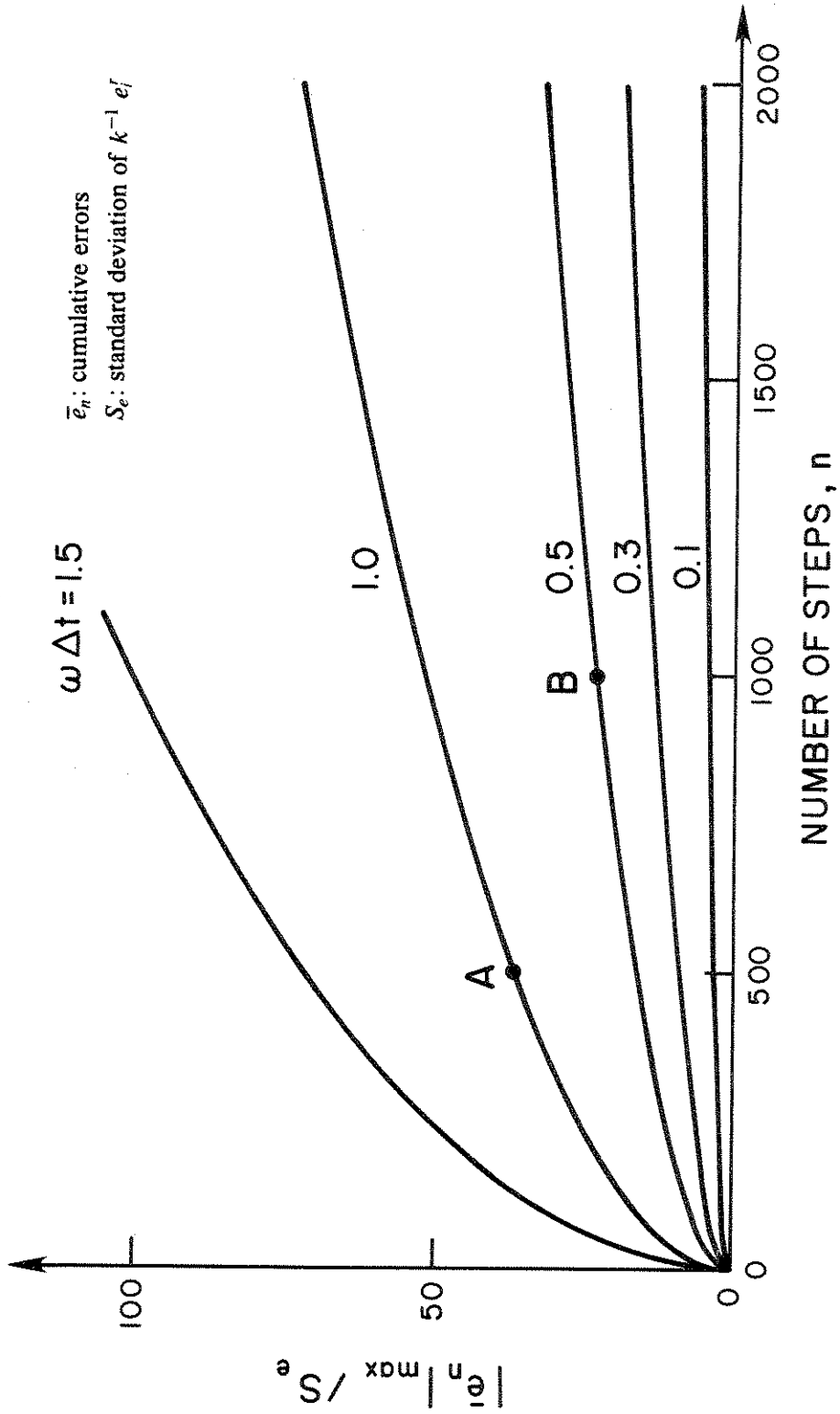
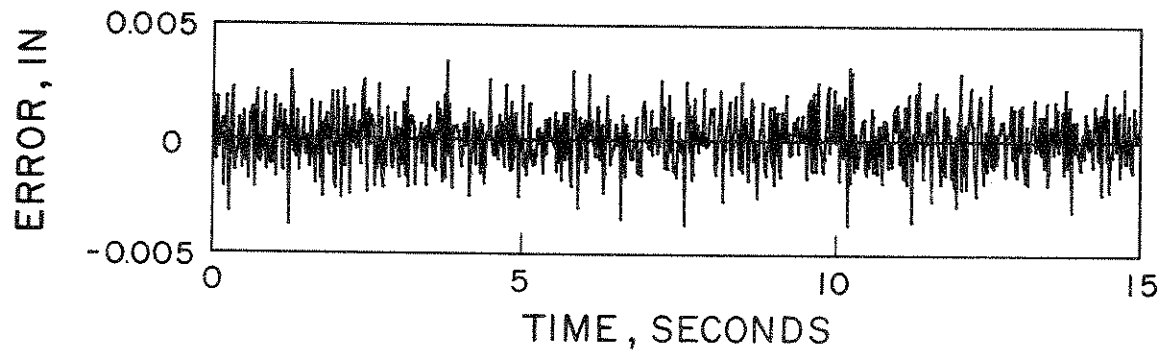
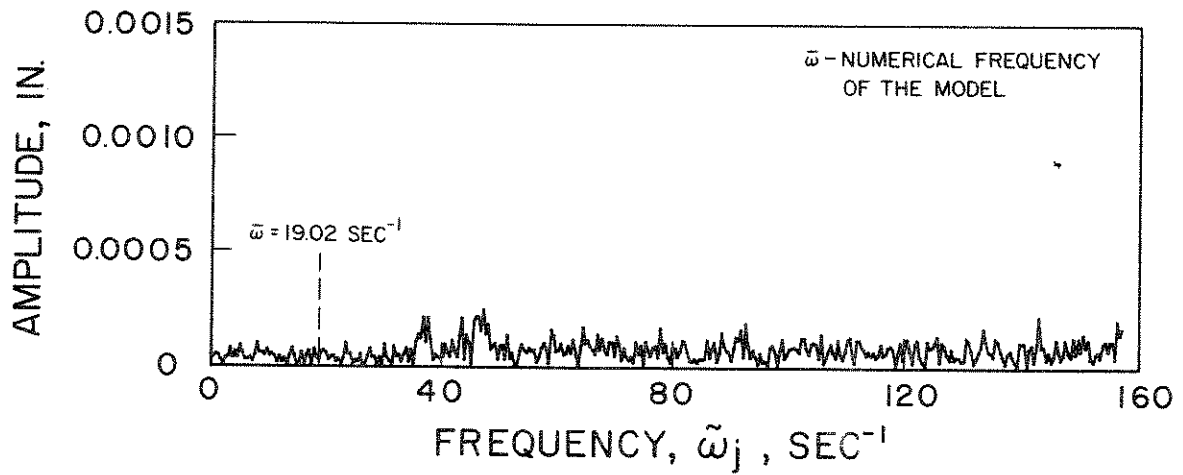


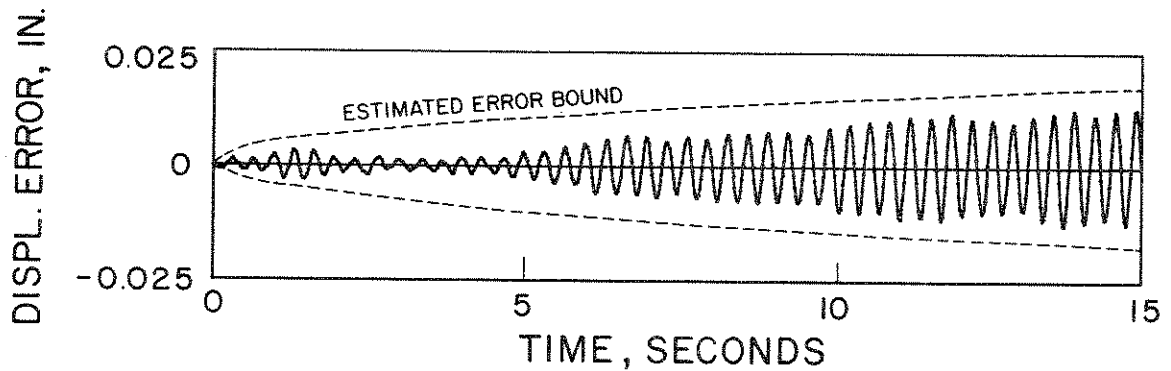
Fig. 4.1 Cumulative Error Bounds due to Random Force-Feedback Errors ( $e_f$ )



(a) Simulated Random Displacement-Control Errors ( $e_i^{dc}$ )



(b) Fourier Spectrum of  $e_i^{dc}$



(c) Cumulative Displacement Errors ( $\bar{e}_i$ ) due to Force-Feedback Errors ( $e_i^f = k e_i^{dc}$ )

Fig. 4.2 Propagation of Random Errors in a Pseudodynamic Response ( $\omega = 18.91 \text{ sec}^{-1}$ ,  $\Delta t = 0.02 \text{ sec}$ )



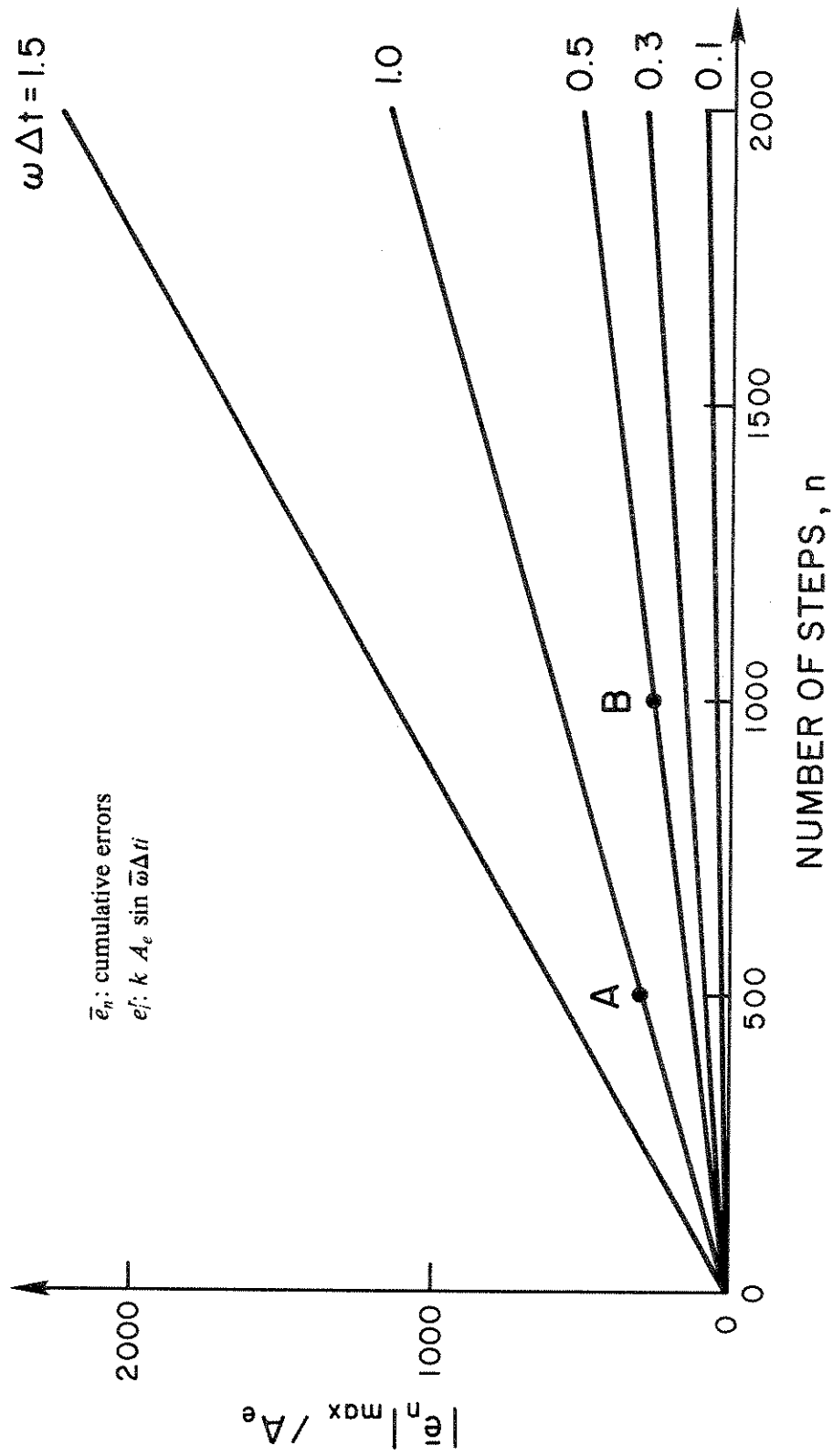


Fig. 4.3 Cumulative Error Bounds due to Sinusoidal Force-Feedback Errors ( $e_f$ ) at Resonance Frequency ( $\bar{\omega}$ )

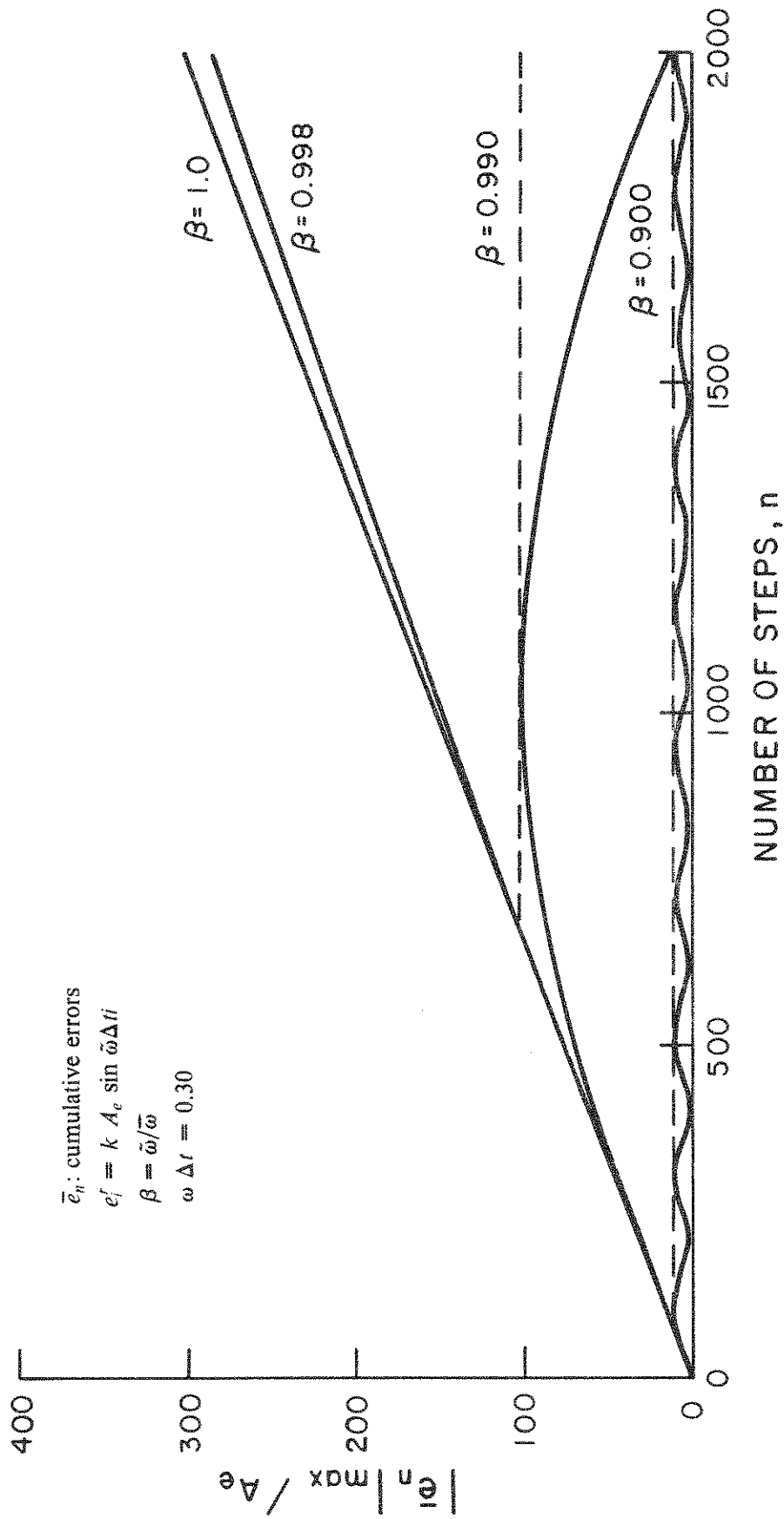
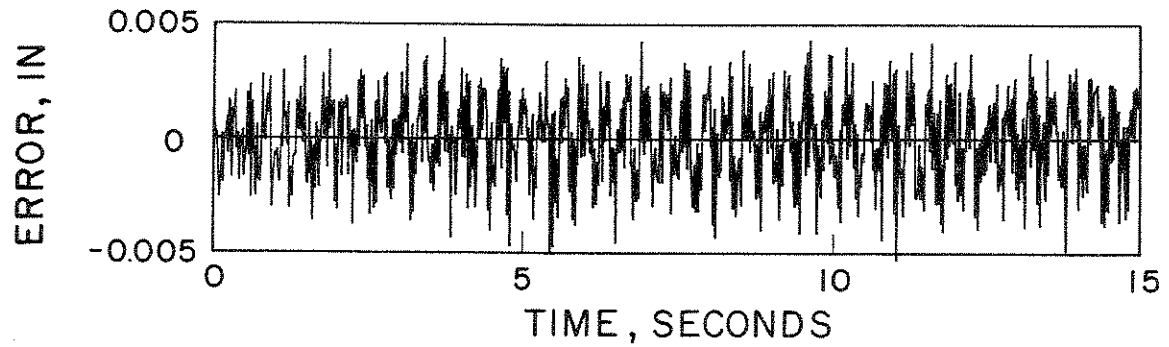
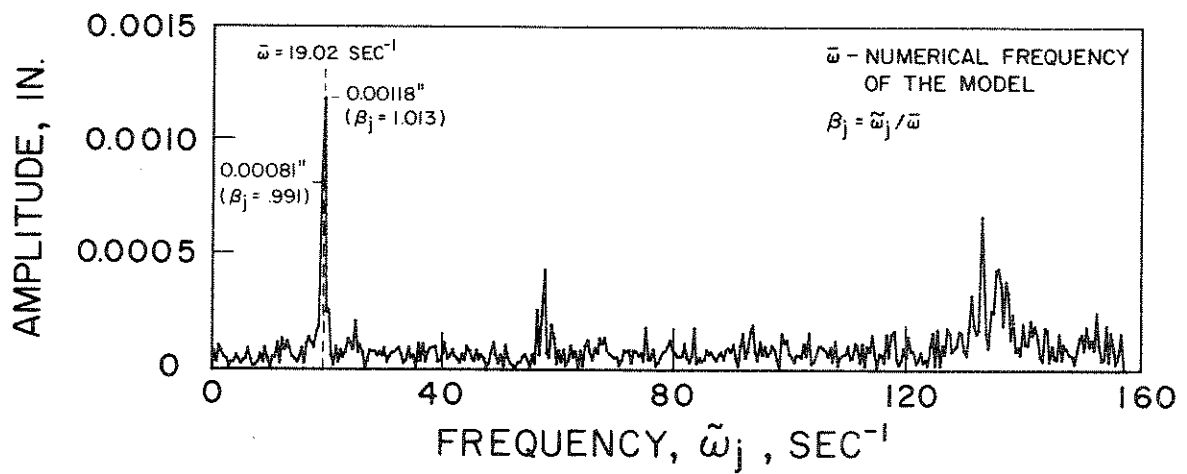


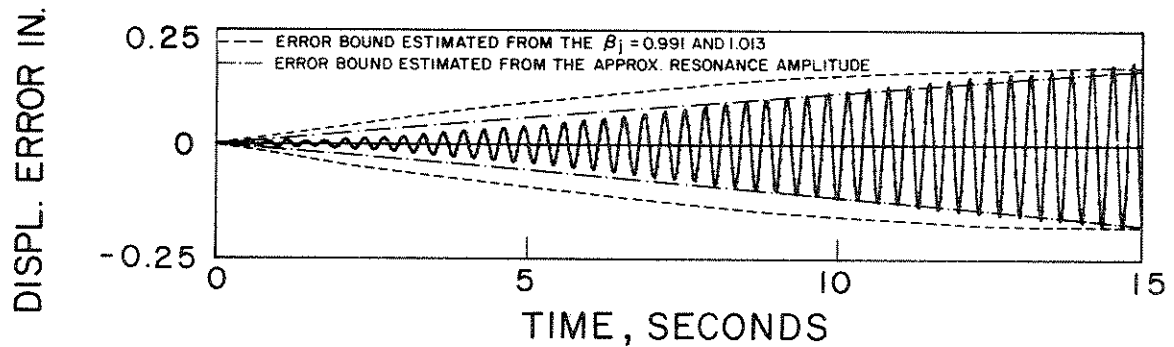
Fig. 4.4 Cumulative Error Bounds due to General Sinusoidal Force-Feedback Errors ( $e_f$ )



(a) Simulated Systematic Displacement-Control Errors ( $e_i^{dc}$ )

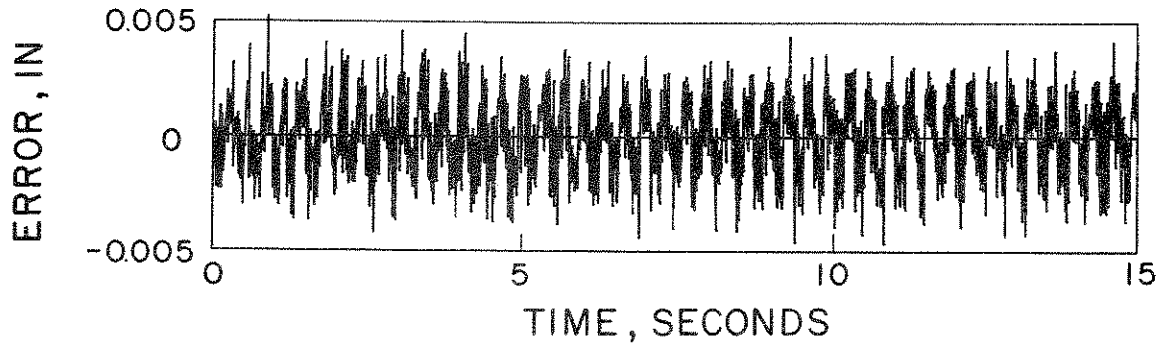


(b) Fourier Spectrum of  $e_i^{dc}$

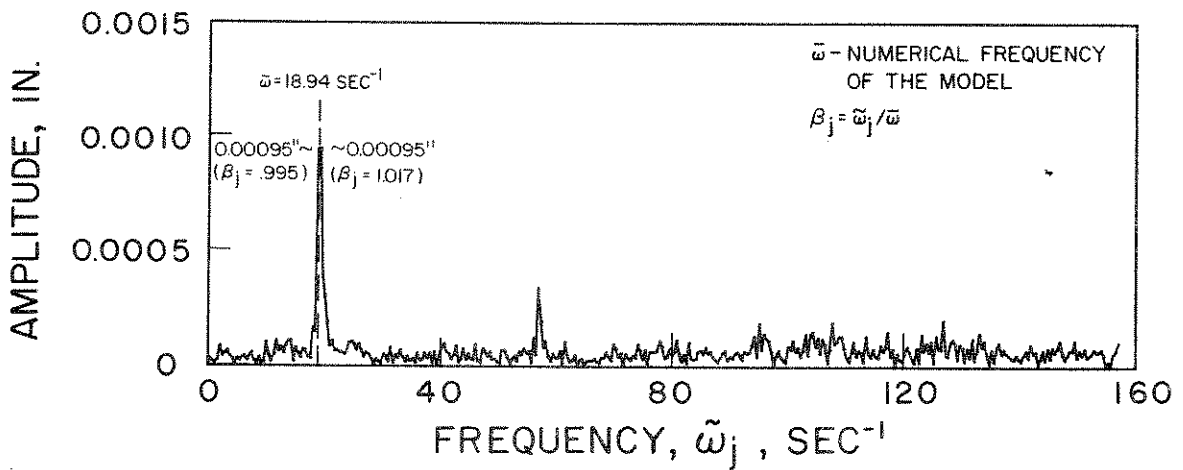


(c) Cumulative Displacement Errors ( $\bar{e}_i$ ) due to Force-Feedback Errors ( $e_i' = k e_i^{dc}$ )

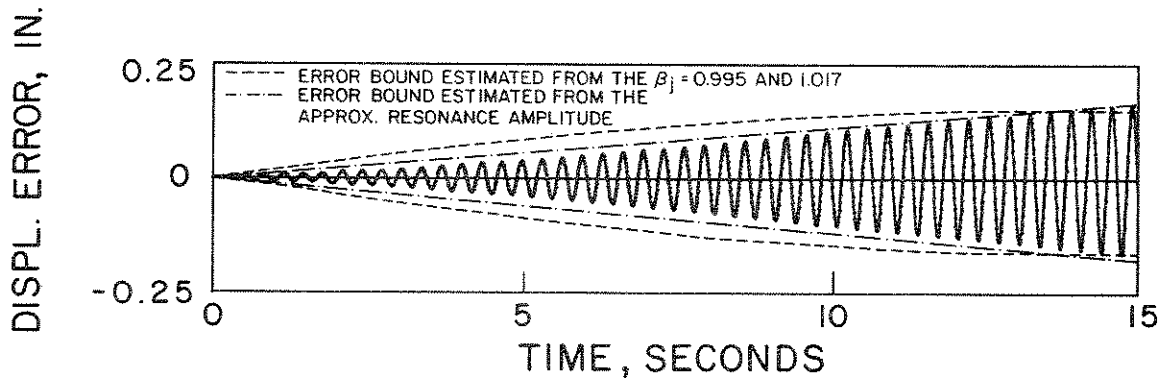
Fig. 4.5 Propagation of Systematic Errors in a Pseudodynamic Response ( $\omega = 18.91 \text{ sec}^{-1}$ ,  $\Delta t = 0.02 \text{ sec}$ )



(a) Simulated Systematic Displacement-Control Errors ( $e_i^{dc}$ )

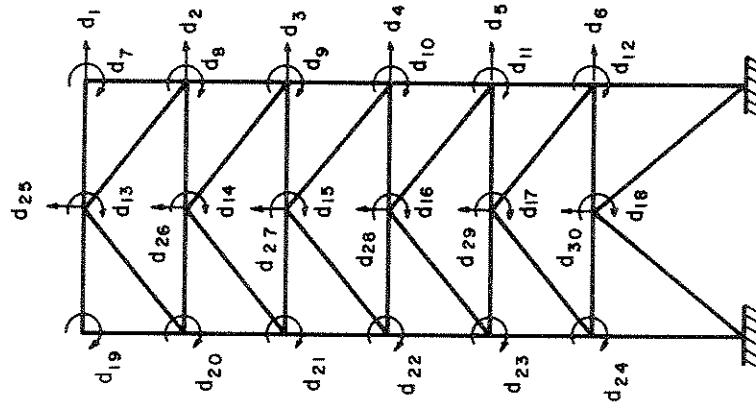


(b) Fourier Spectrum of  $e_i^{dc}$

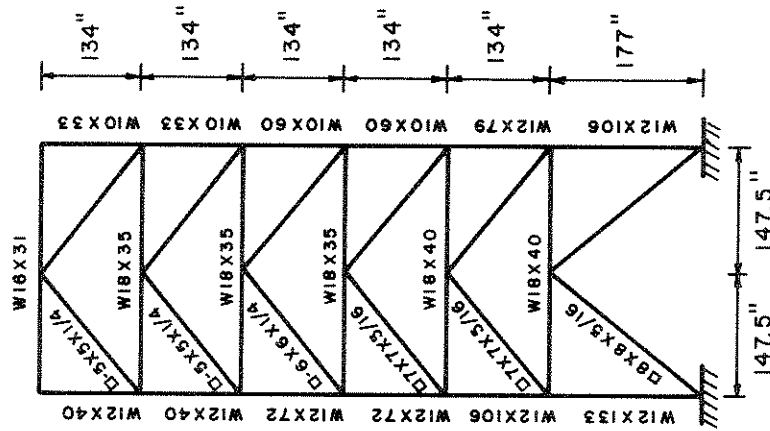


(c) Cumulative Displacement Errors ( $\bar{e}_i$ ) due to Force-Feedback Errors ( $e_i^f = k e_i^{dc}$ )

Fig. 4.6 Propagation of Systematic Errors in a Pseudodynamic Response ( $\omega = 18.91 \text{ sec}^{-1}$ ,  $\Delta t = 0.01 \text{ sec}$ )



(b) Total Number of Degrees of Freedom



(a) Frame Configuration and Member Sizes

Fig. 5.1 Six-Story K-Braced Steel Frame

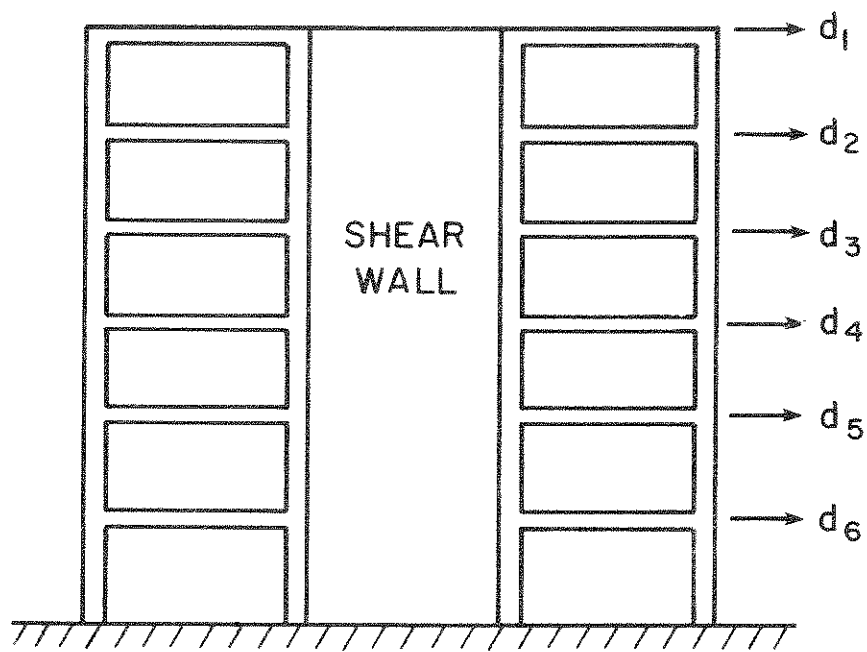
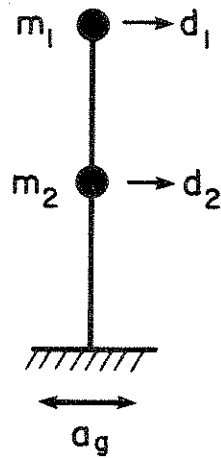


Fig. 5.2 Six-Story Reinforced Concrete Structure



$$\mathbf{k} = \begin{bmatrix} 5.979 & -14.947 \\ -14.947 & 47.830 \end{bmatrix} \text{ kip/in}$$

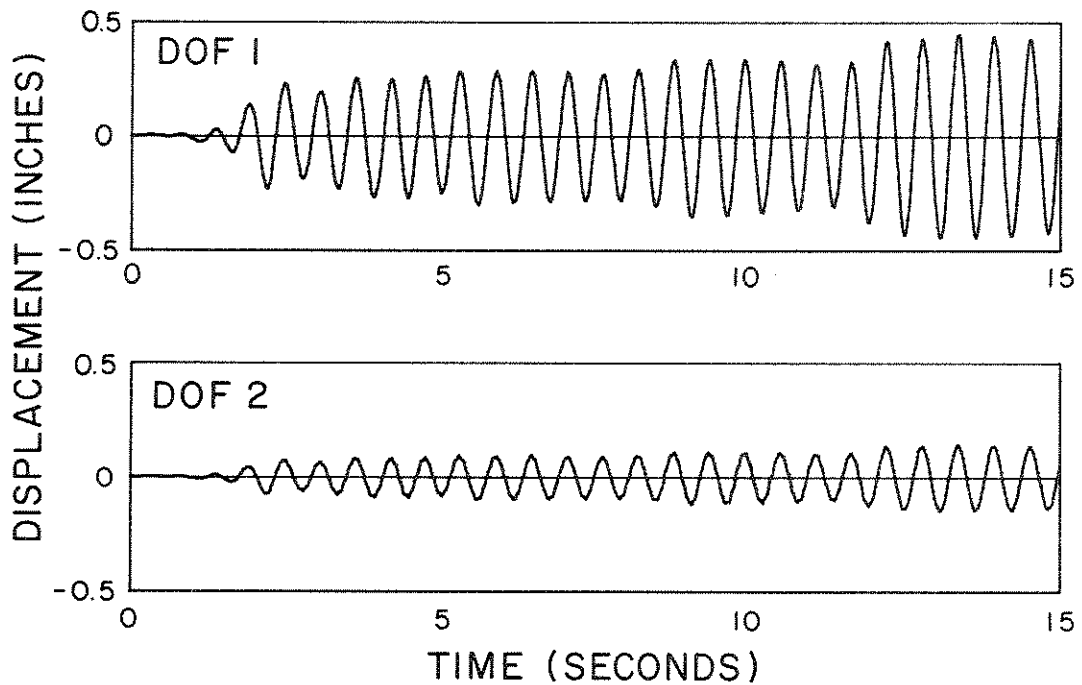
$$\mathbf{m} = \begin{bmatrix} 0.01 & 0 \\ 0 & 0.01 \end{bmatrix} \text{ kip}\cdot\text{sec}^2/\text{in}$$

$$\Phi = \begin{bmatrix} 0.952 & 0.305 \\ 0.305 & -0.952 \end{bmatrix}$$

$$\omega_1 = 10.90 \text{ sec}^{-1}$$

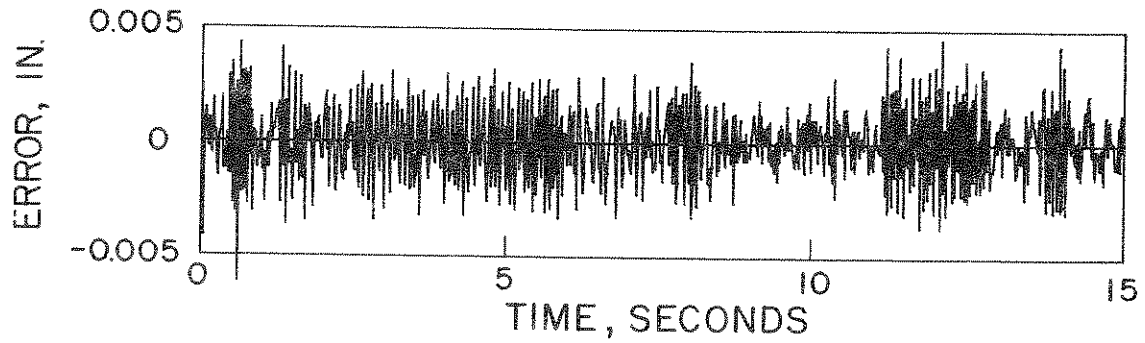
$$\omega_2 = 72.54 \text{ sec}^{-1}$$

(a) Two-Degree-of-Freedom Model

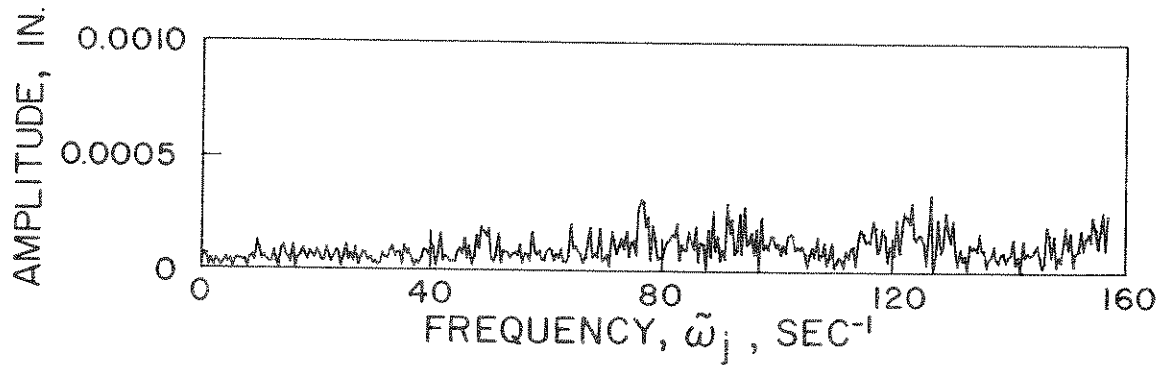


(b) Exact Numerical Responses using Newmark Explicit Method  
( $\Delta t = 0.02 \text{ sec}$ )

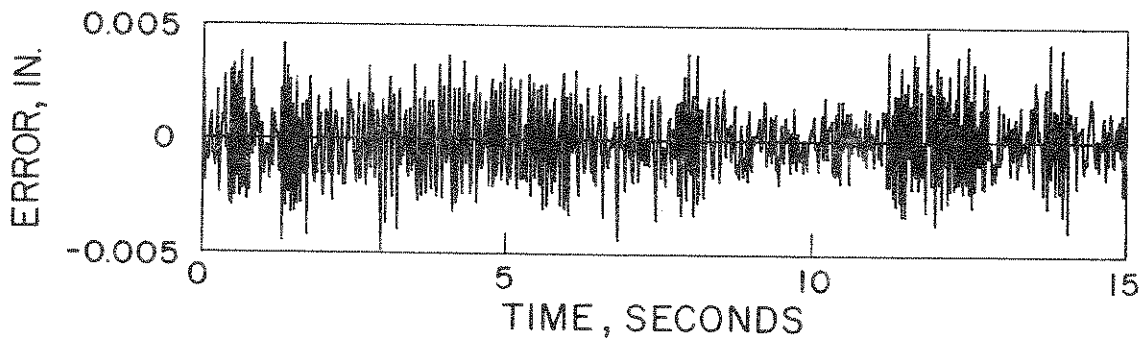
Fig. 5.3 Two-Degree-of-Freedom Simulation using El Centro 1940 (NS), 0.02g Ground Acceleration



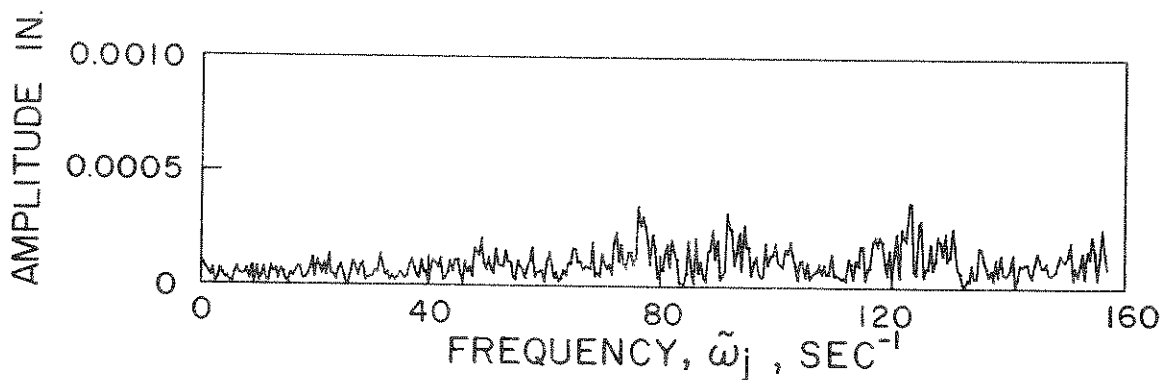
(a) Displacement-Control Errors ( $e_i^{dc}$ ) at DOF 1



(b) Fourier Spectrum of  $e_i^{dc}$  at DOF 1



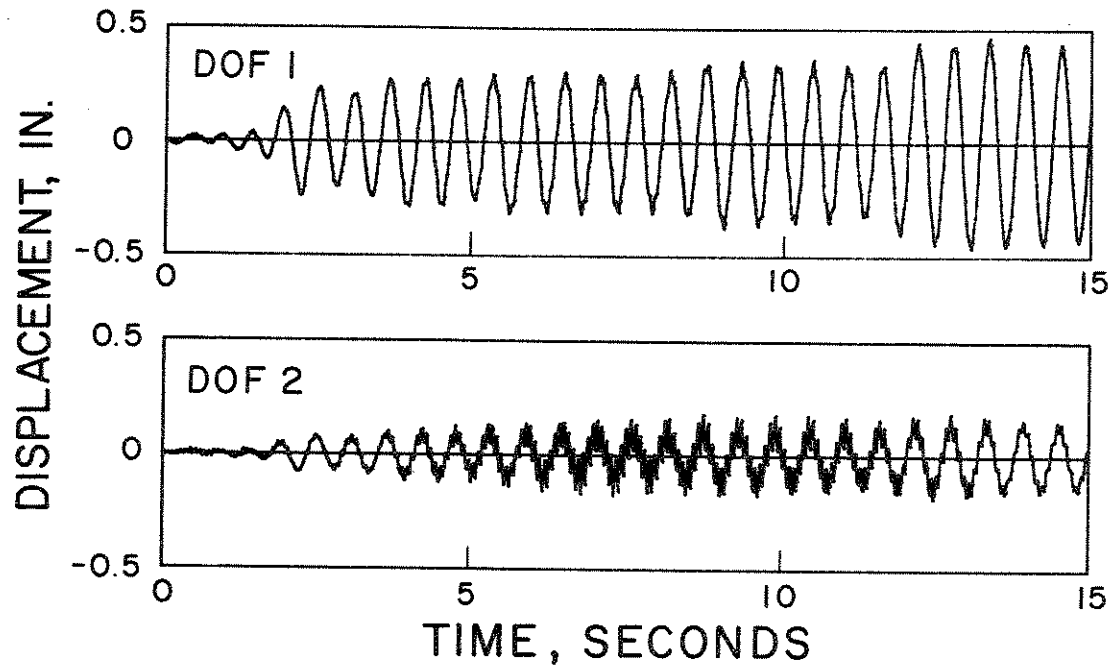
(c) Displacement-Control Errors ( $e_i^{dc}$ ) at DOF 2



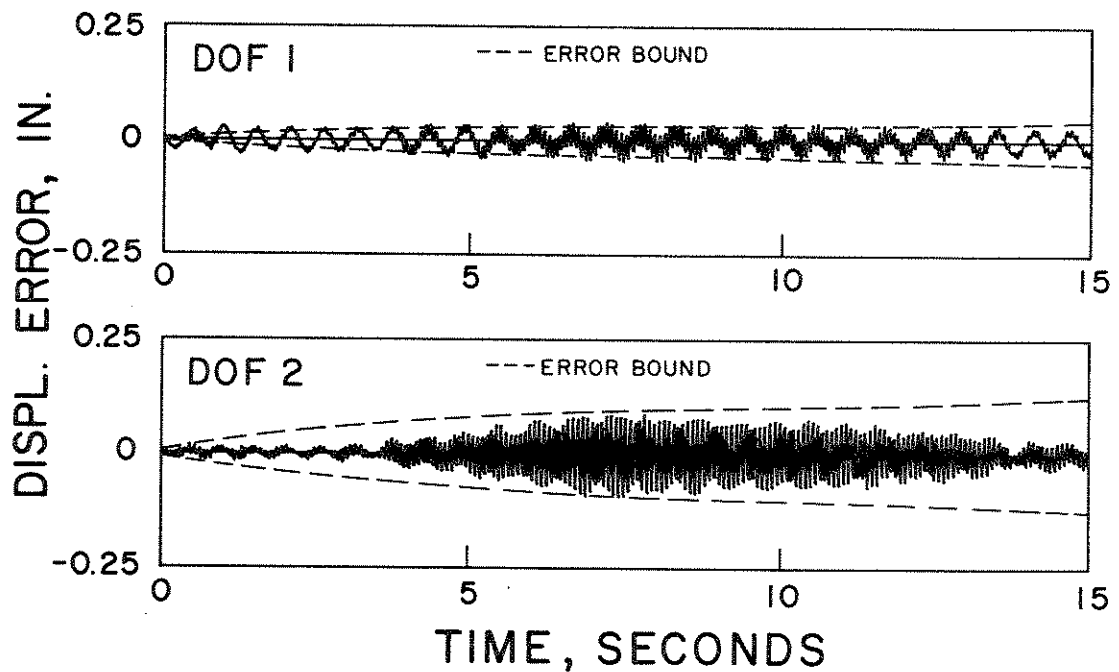
(d) Fourier Spectrum of  $e_i^{dc}$  at DOF 2

Fig. 5.4 Random Errors Generated in a 2 DOF Simulation



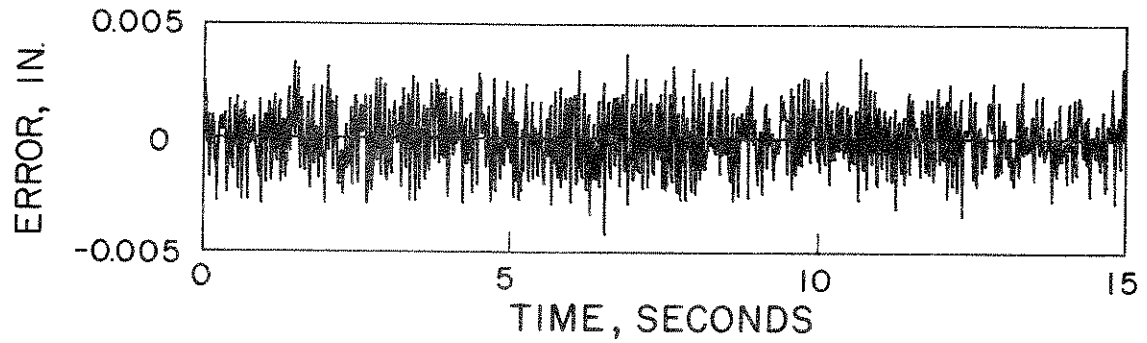


(a) Displacement Time Histories  
( $\omega_1 = 10.90 \text{ sec}^{-1}$ ,  $\omega_2 = 72.54 \text{ sec}^{-1}$ ,  $\Delta t = 0.02 \text{ sec}$ )

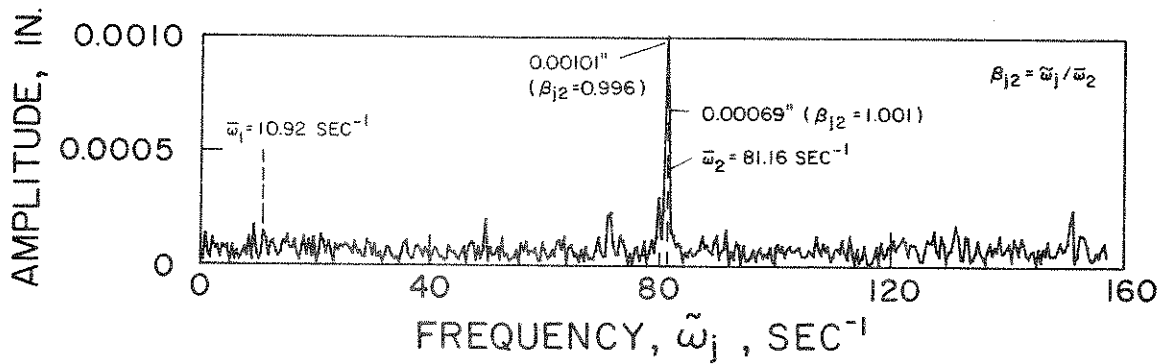


(b) Cumulative Displacement Errors ( $\bar{\epsilon}_i$ )

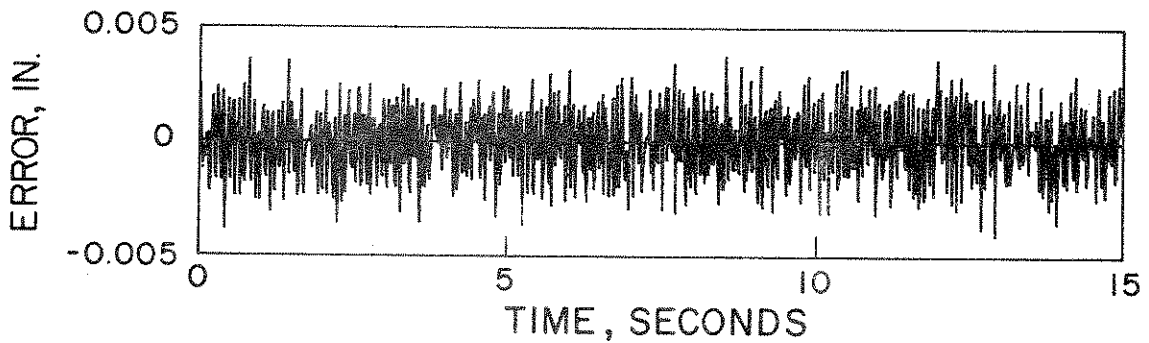
Fig. 5.5 Two-Degree-of-Freedom Simulation with Random Errors  
using El Centro 1940 (NS), 0.02g Ground Acceleration



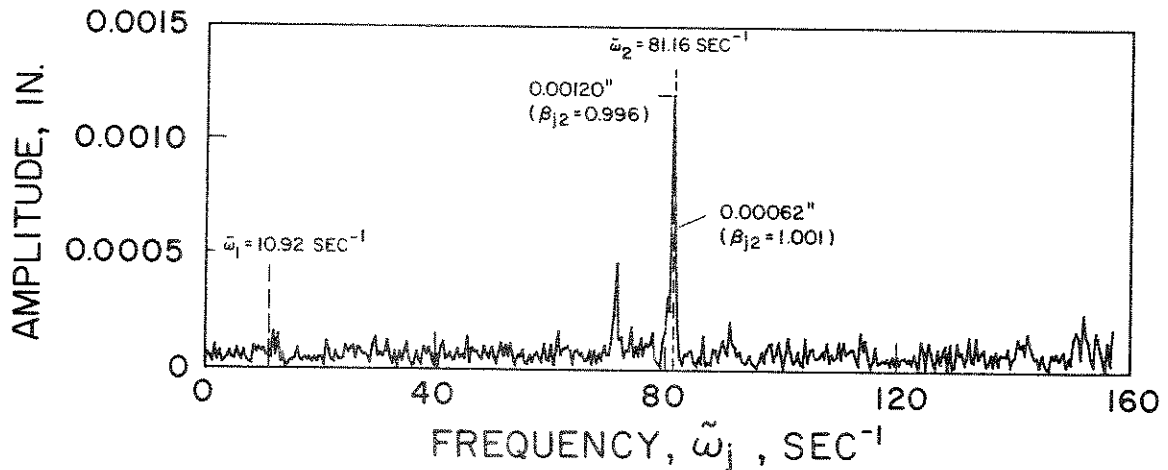
(a) Displacement-Control Errors ( $e_i^{dc}$ ) at DOF 1



(b) Fourier Spectrum of  $e_i^{dc}$  at DOF 1

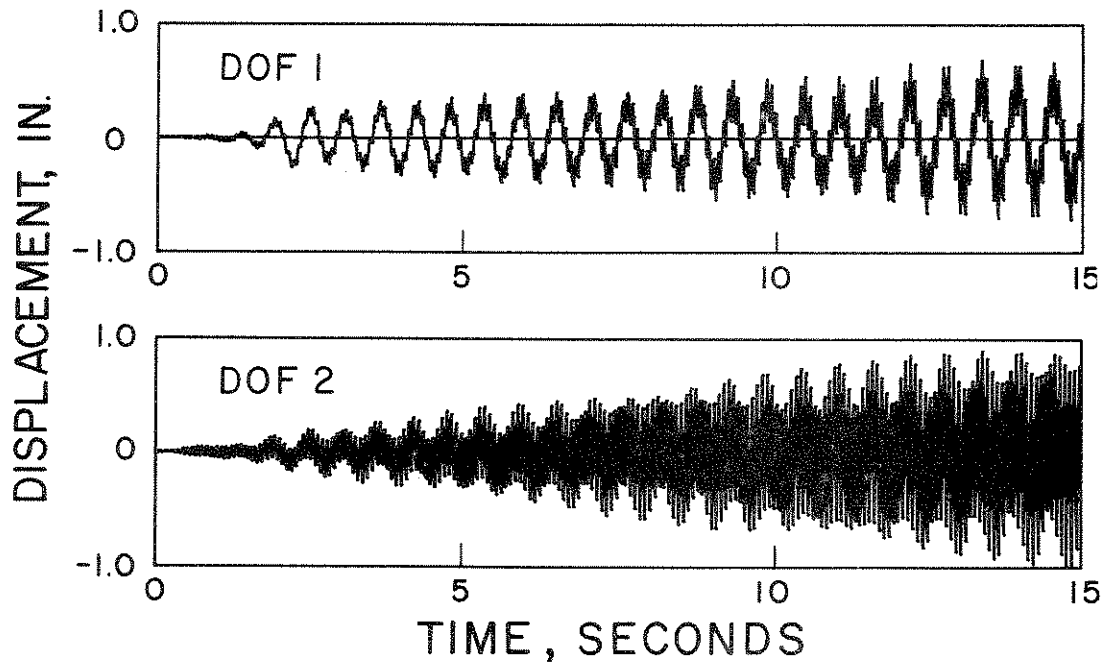


(c) Displacement-Control Errors ( $e_i^{dc}$ ) at DOF 2

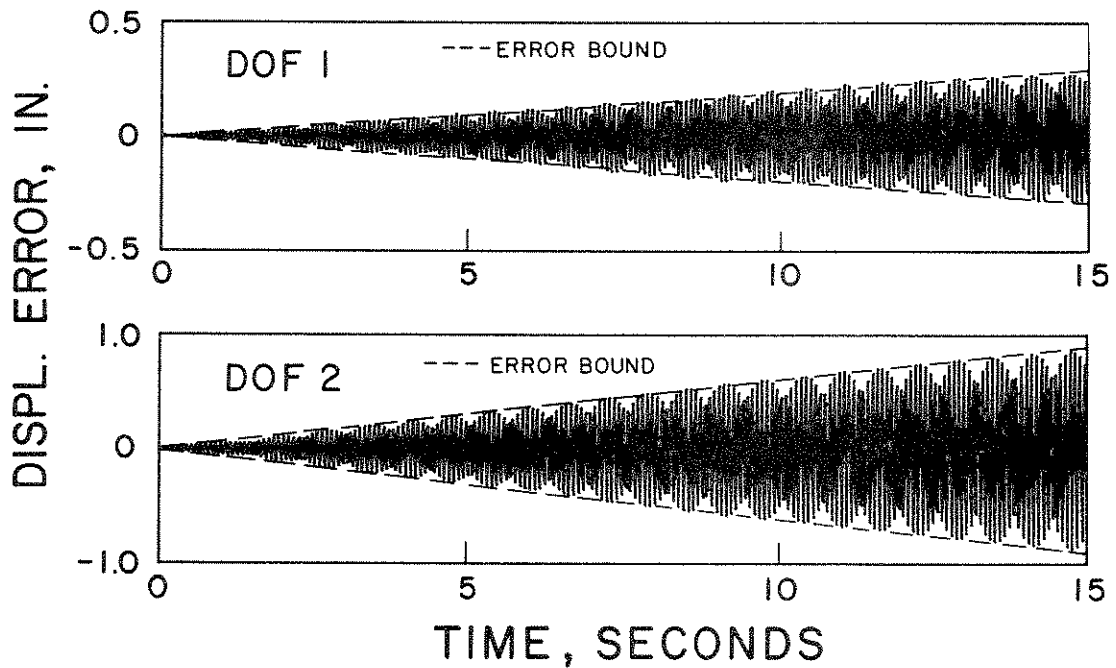


(d) Fourier Spectrum of  $e_i^{dc}$  at DOF 2

Fig. 5.6 Systematic Errors Generated in a 2 DOF Simulation



(a) Displacement Time Histories  
( $\omega_1 = 10.90 \text{ sec}^{-1}$ ,  $\omega_2 = 72.54 \text{ sec}^{-1}$ ,  $\Delta t = 0.02 \text{ sec}$ )



(b) Cumulative Displacement Errors ( $\bar{e}_i$ )

Fig. 5.7 Two-Degree-of-Freedom Simulation with Systematic Errors  
using El Centro 1940 (NS), 0.02g Ground Acceleration

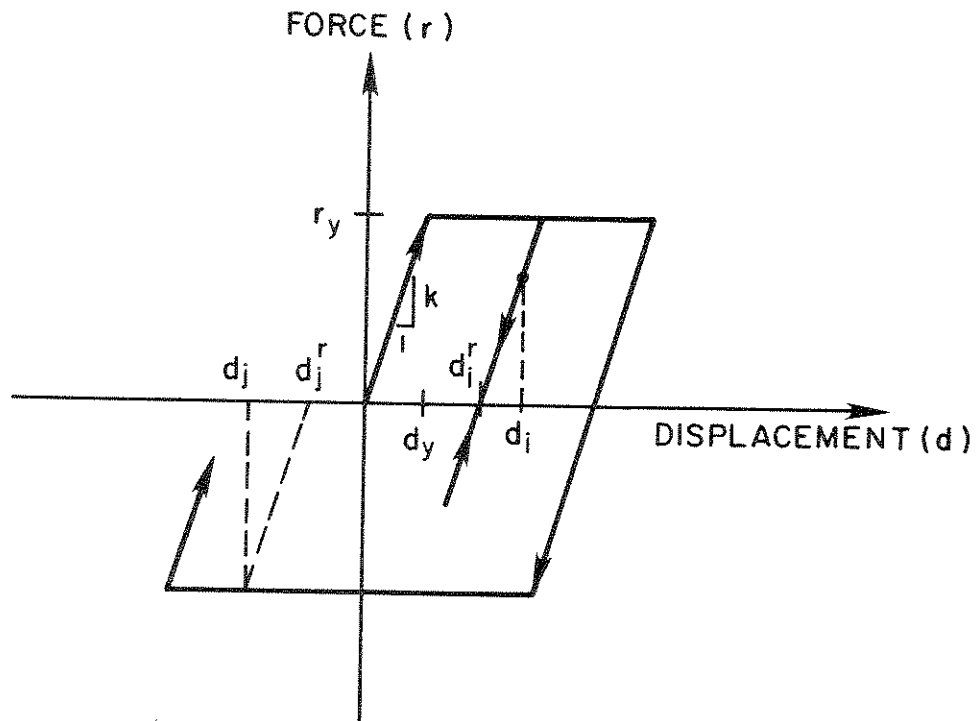


Fig. 6.1 Elasto-Plastic Model of a Single-Degree-of-Freedom System

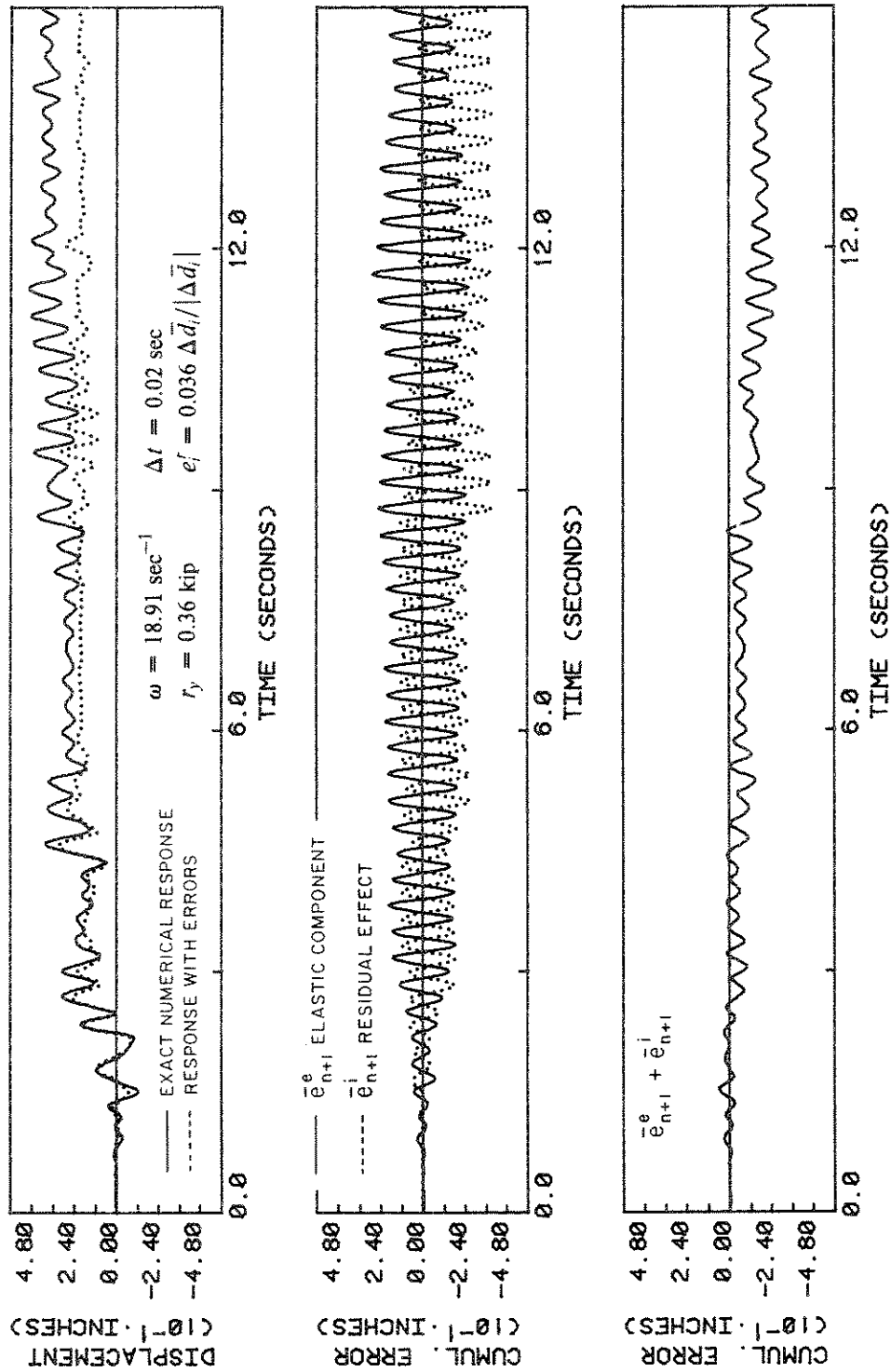


Fig. 6.2 Error Propagation in an Elasto-Plastic SDOF System with El Centro 1940 (NS), 0.1g Ground Acceleration

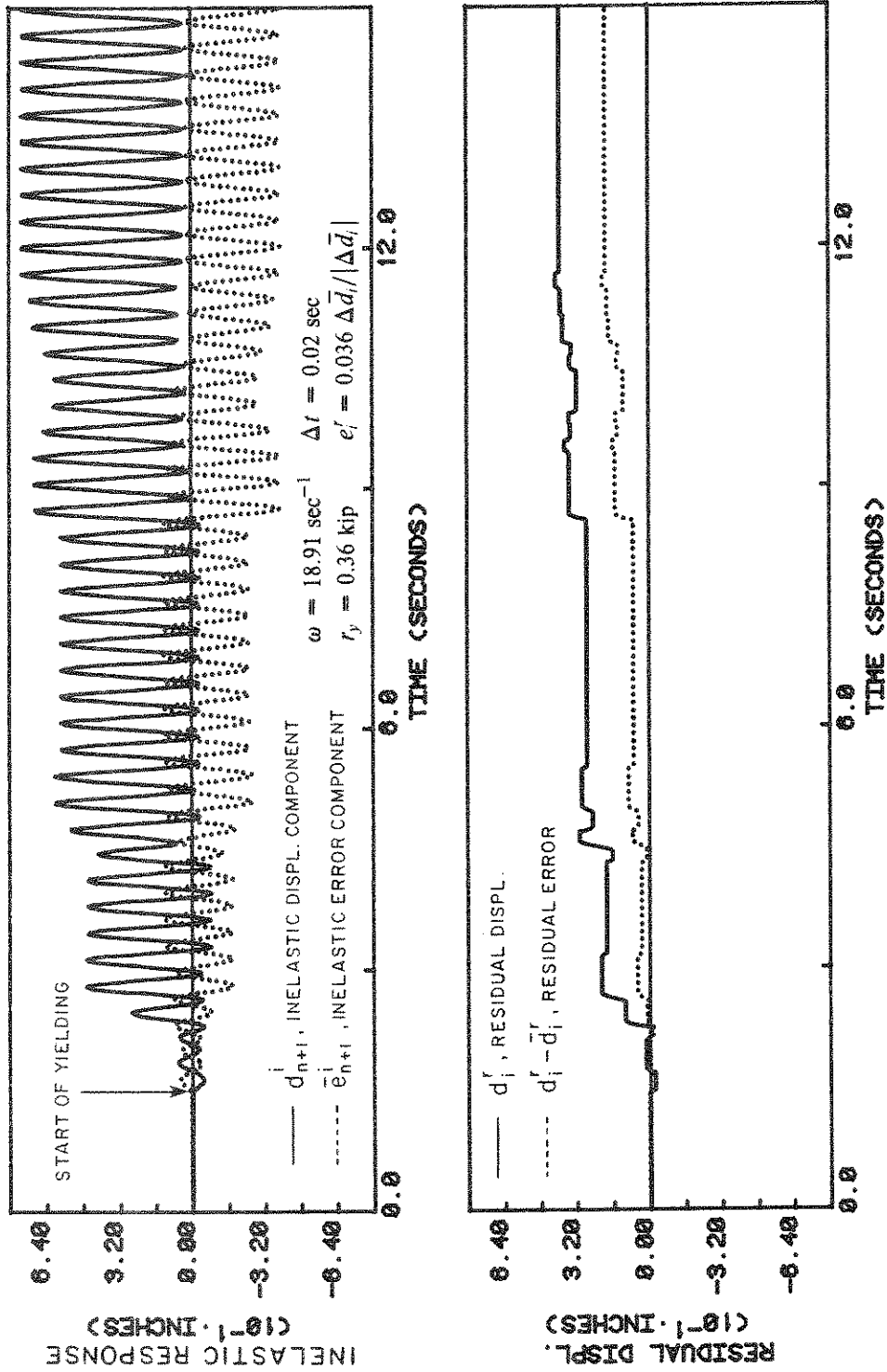


Fig. 6.3 Inelastic Residual Effect in an Elasto-Plastic SDOF System with El Centro 1940 (NS), 0.1g Ground Acceleration

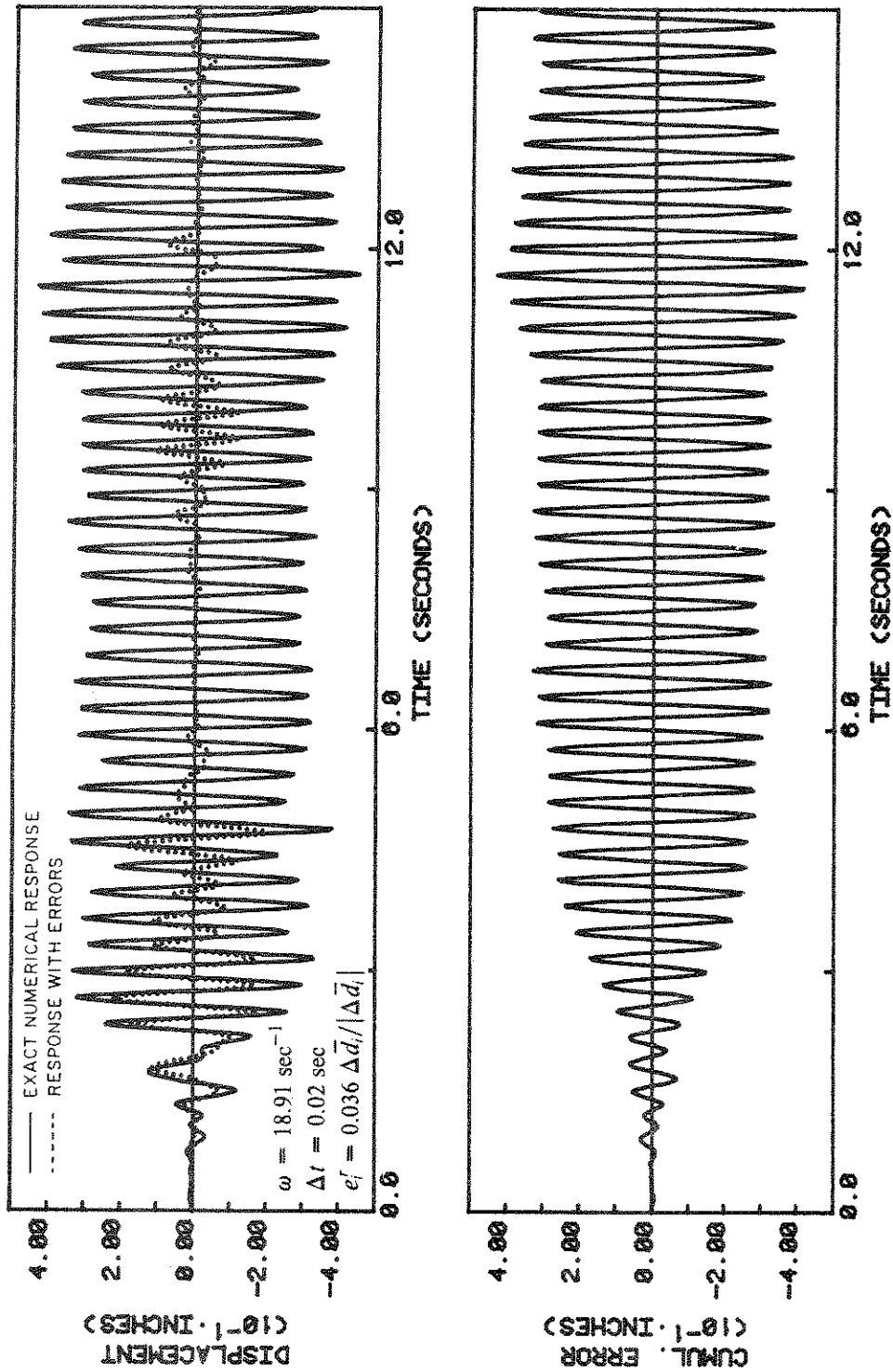


Fig. 6.4 Error Propagation in a Linear Elastic SDOF System with El Centro 1940 (NS), 0.1g Ground Acceleration

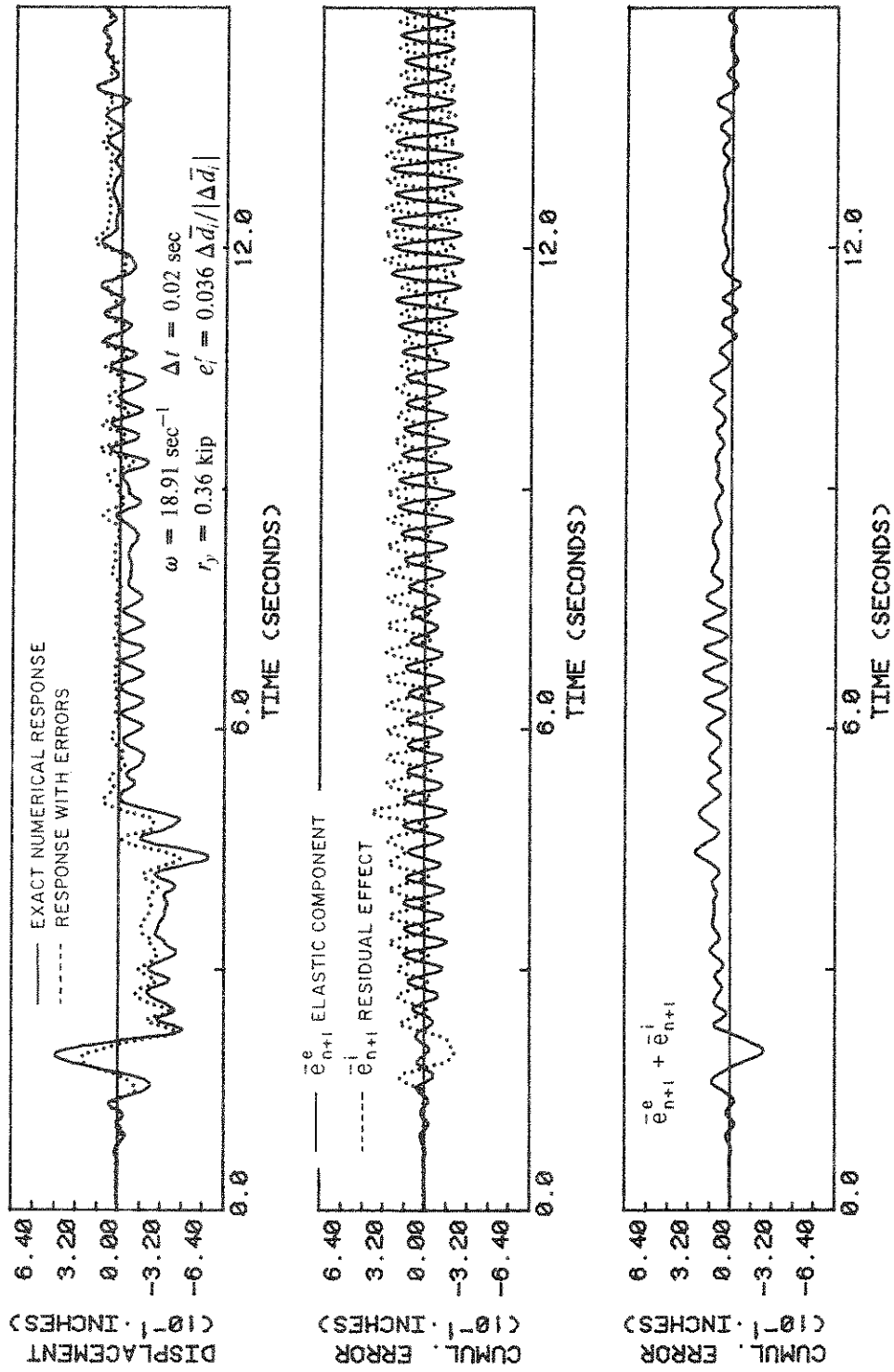


Fig. 6.5 Error Propagation in an Elasto-Plastic SDOF System with El Centro 1940 (NS), 0.15g Ground Acceleration



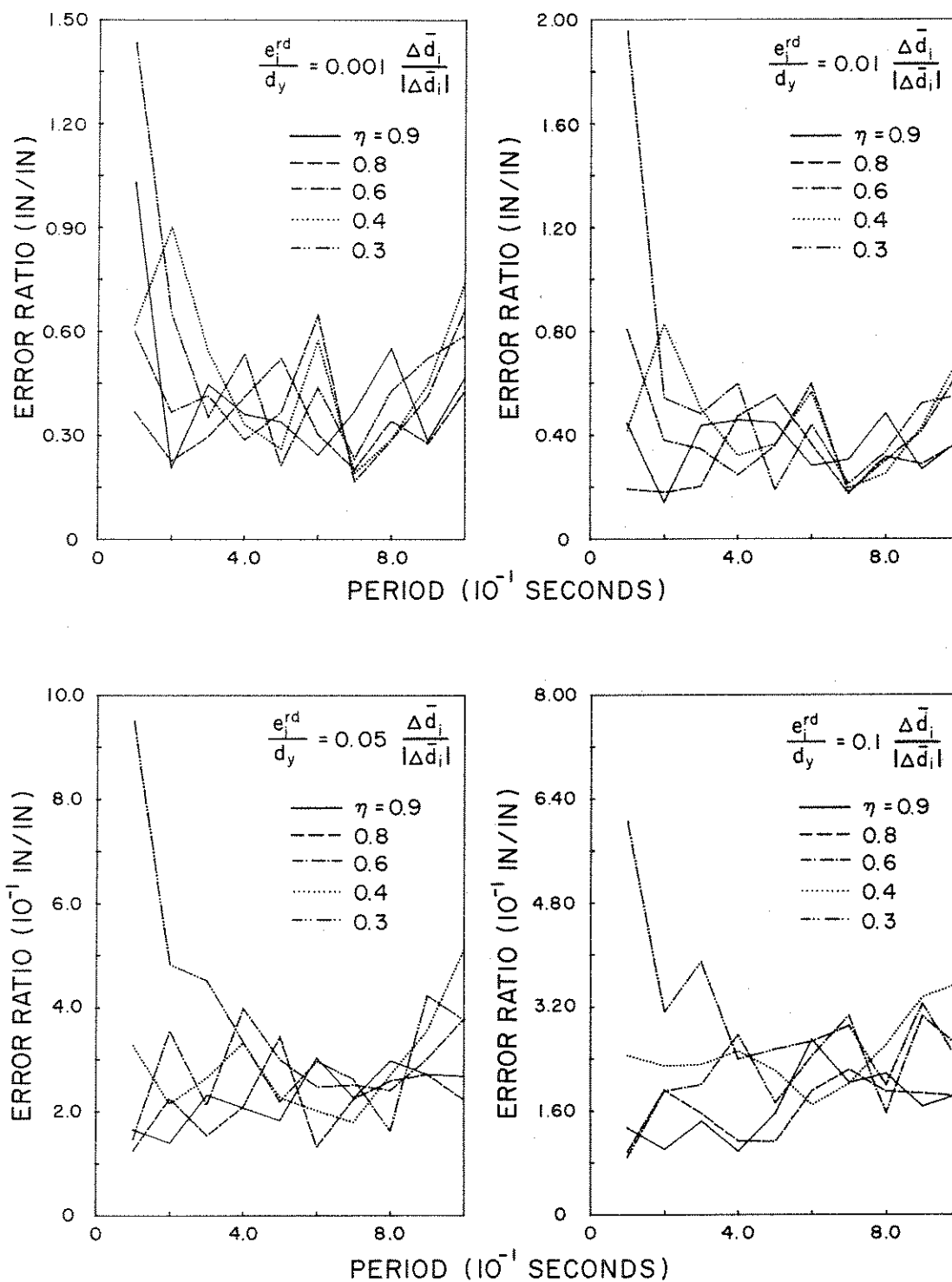


Fig. 6.6 Error Ratio Spectra with El Centro 1940 (NS) Ground Acceleration ( $\Delta t = 0.02$  sec)

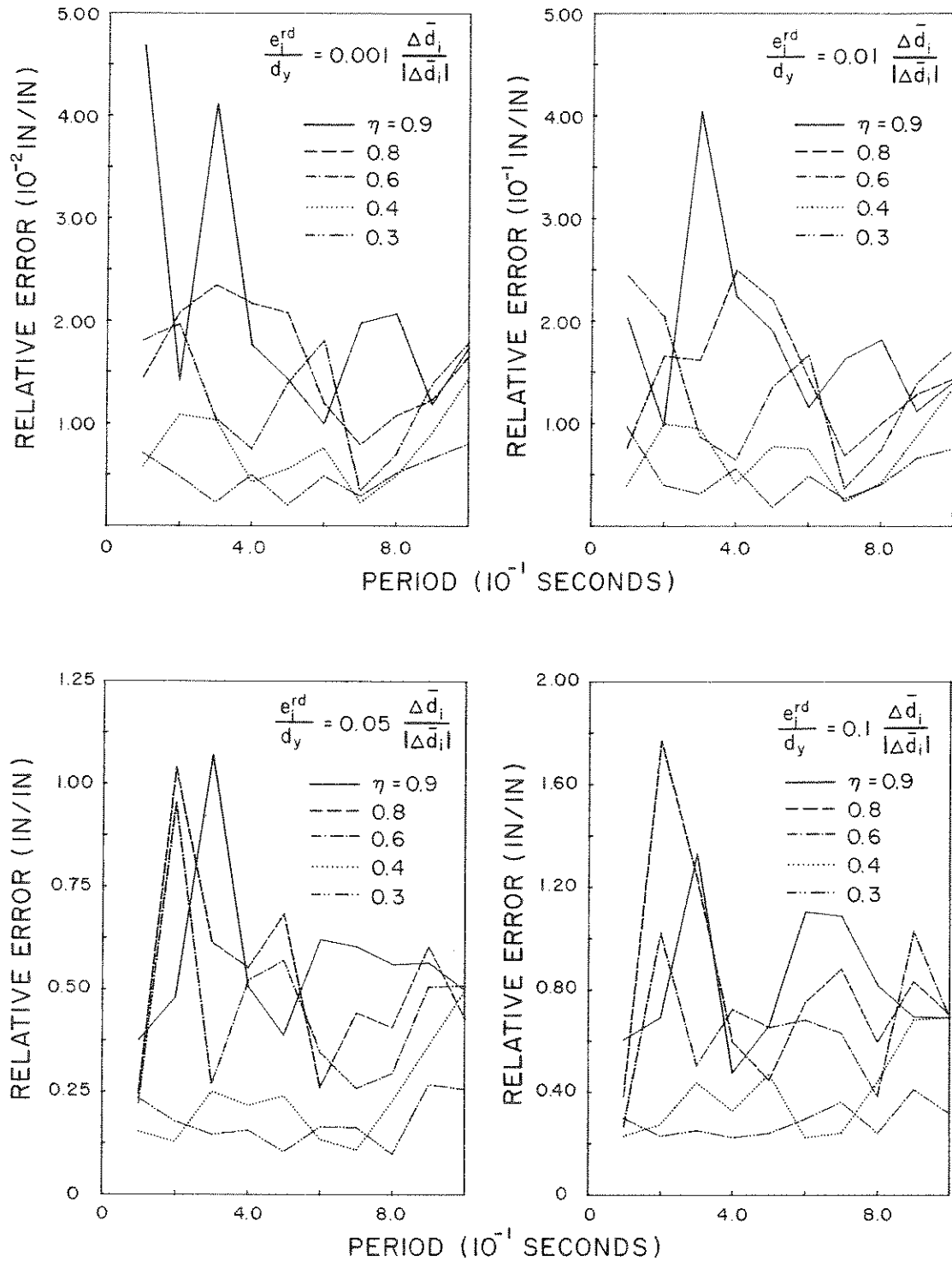
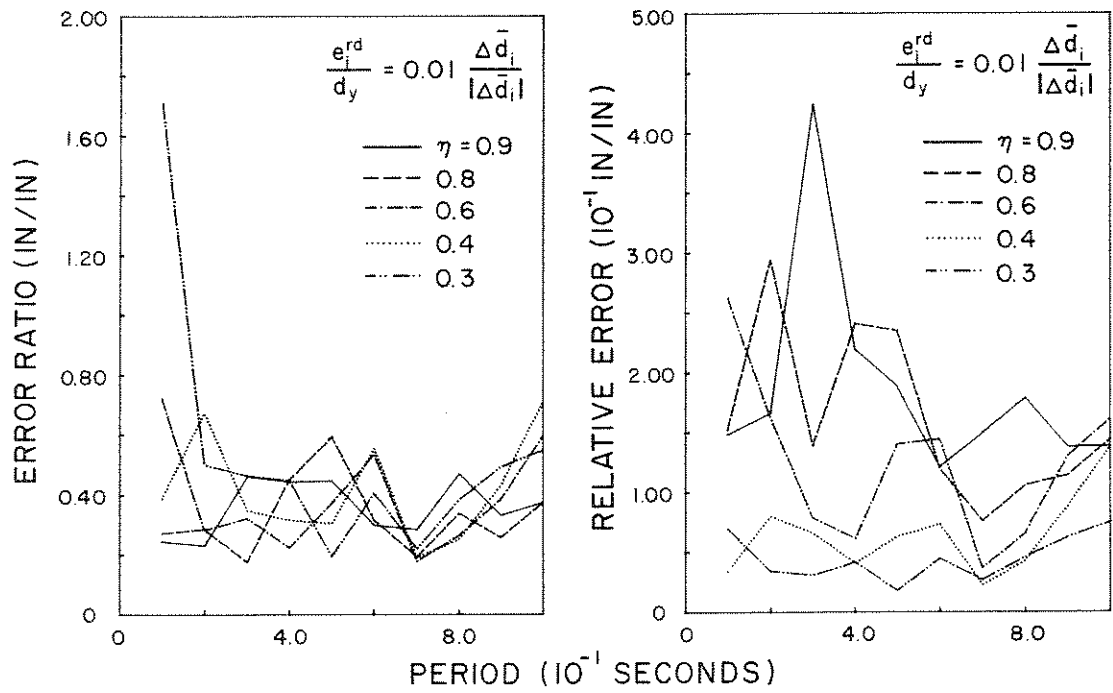
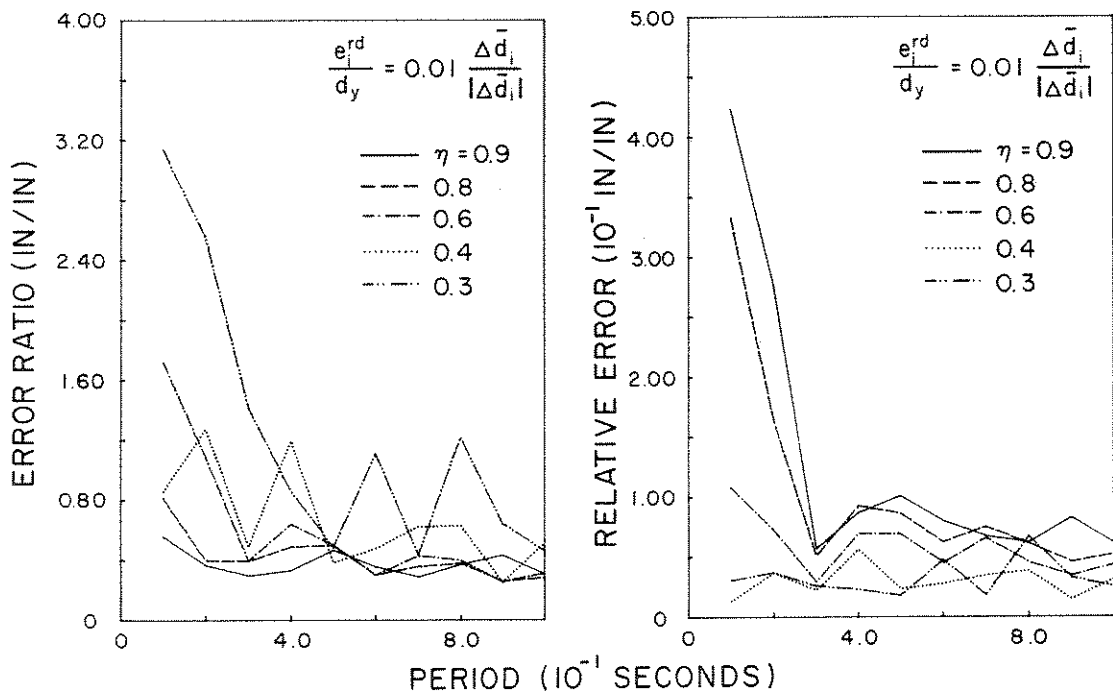


Fig. 6.7 Relative Error Spectra with El Centro 1940 (NS) Ground Acceleration ( $\Delta t = 0.02$  sec)

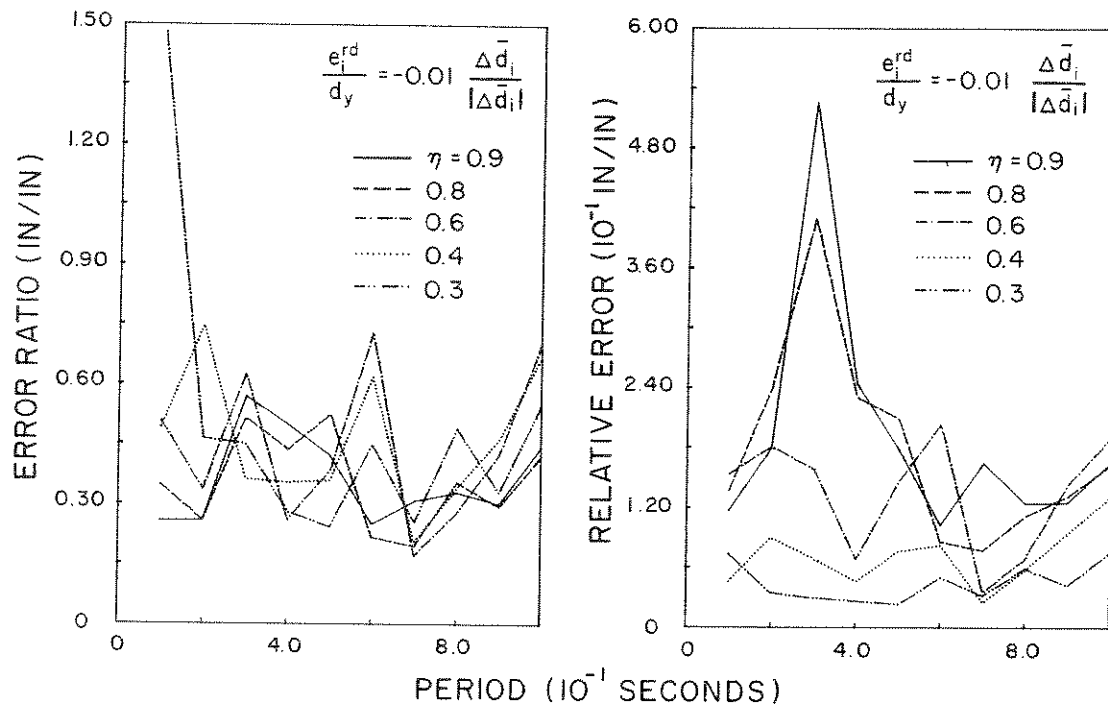


El Centro 1940 (NS),  $\Delta t = 0.01$  sec



Miyagi Oki 1978,  $\Delta t = 0.01$  sec

Fig. 6.8 Error Spectra Under Various Conditions



El Centro 1940 (NS),  $\Delta t = 0.02$  sec

Fig. 6.8 Error Spectra Under Various Conditions

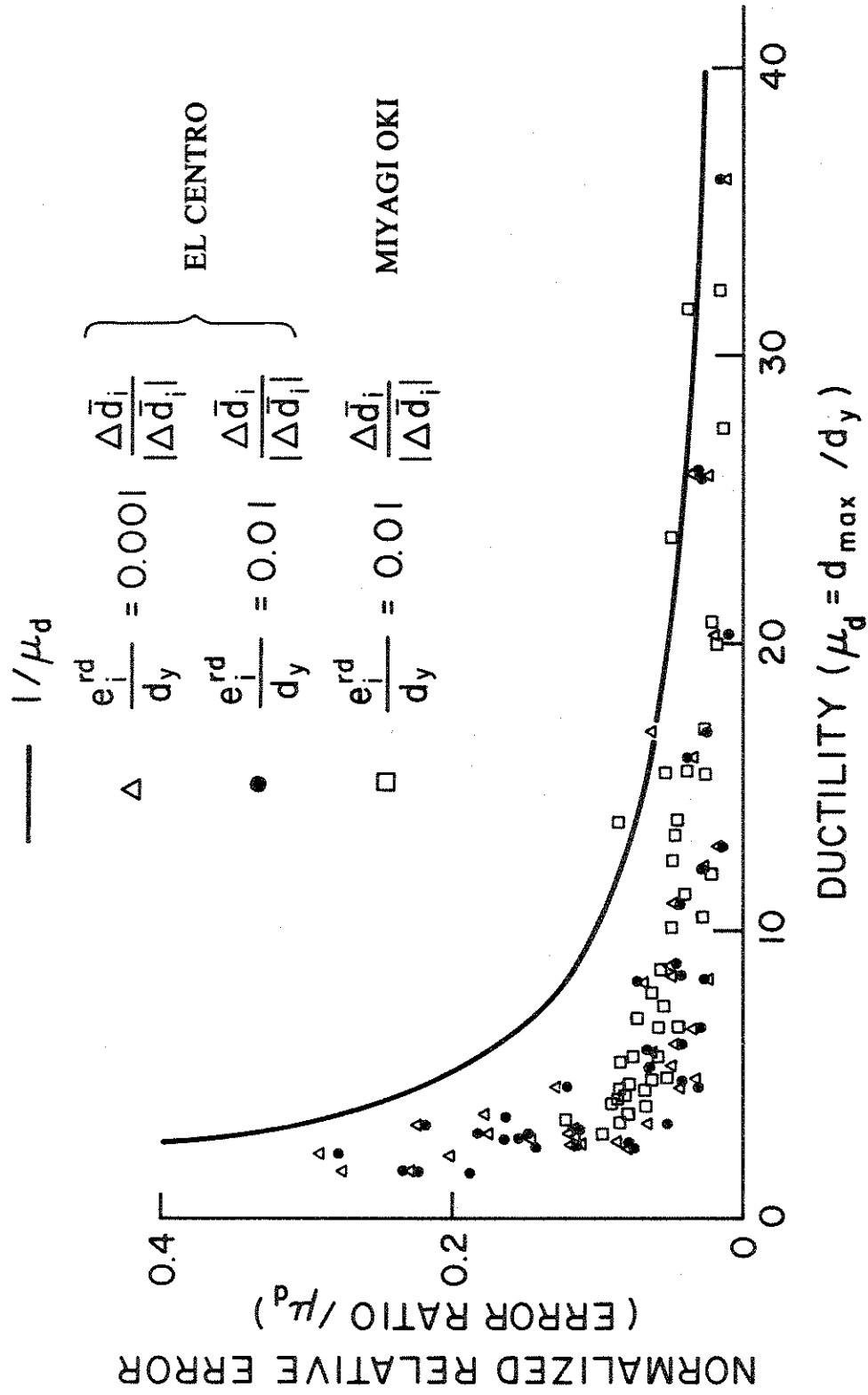


Fig. 6.9 Reduction of Relative Errors due to Increased Displacement Ductility

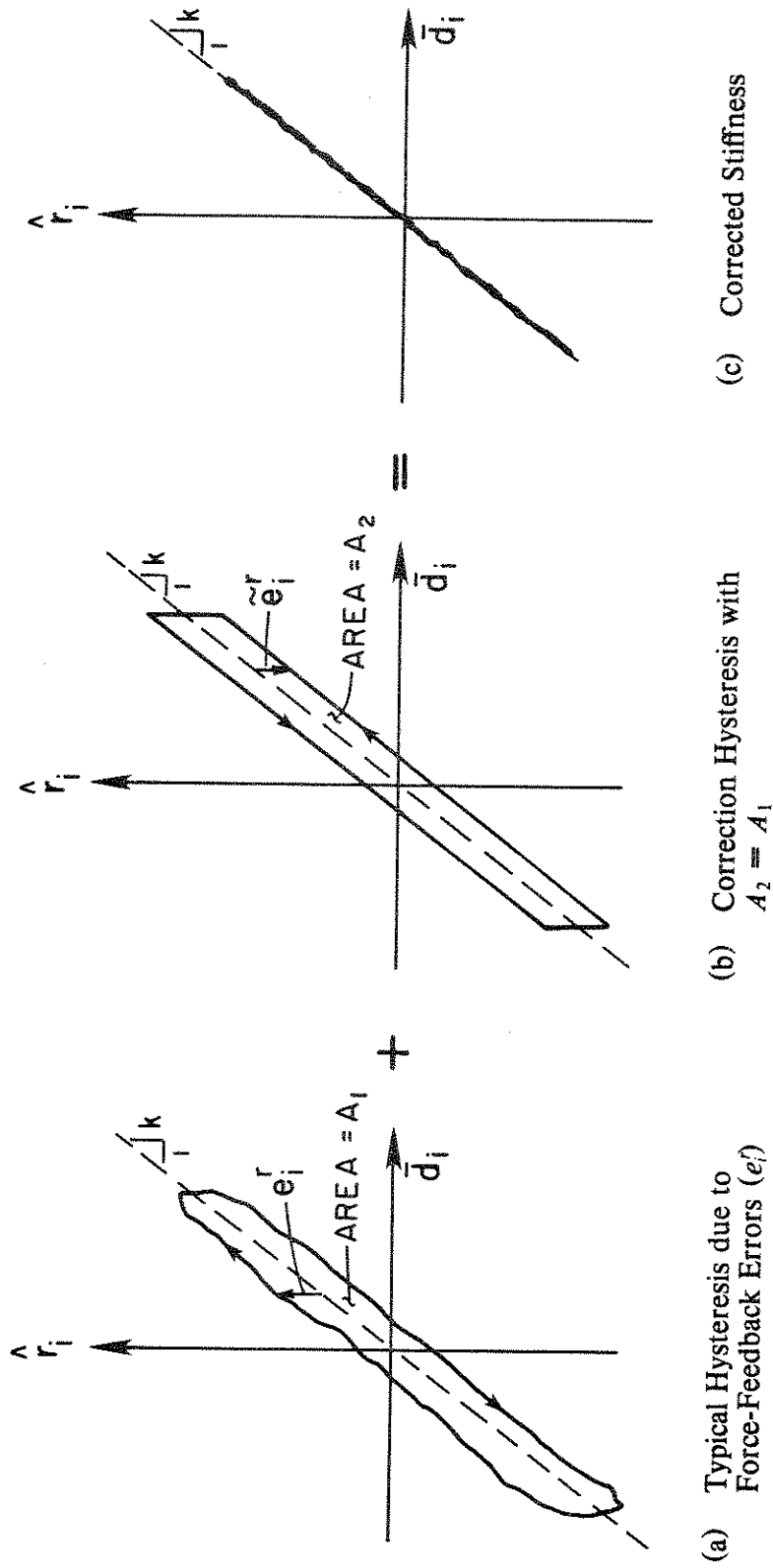


Fig. 7.1 Correction of Force-Feedback Errors in a Single-Degree-of-Freedom System

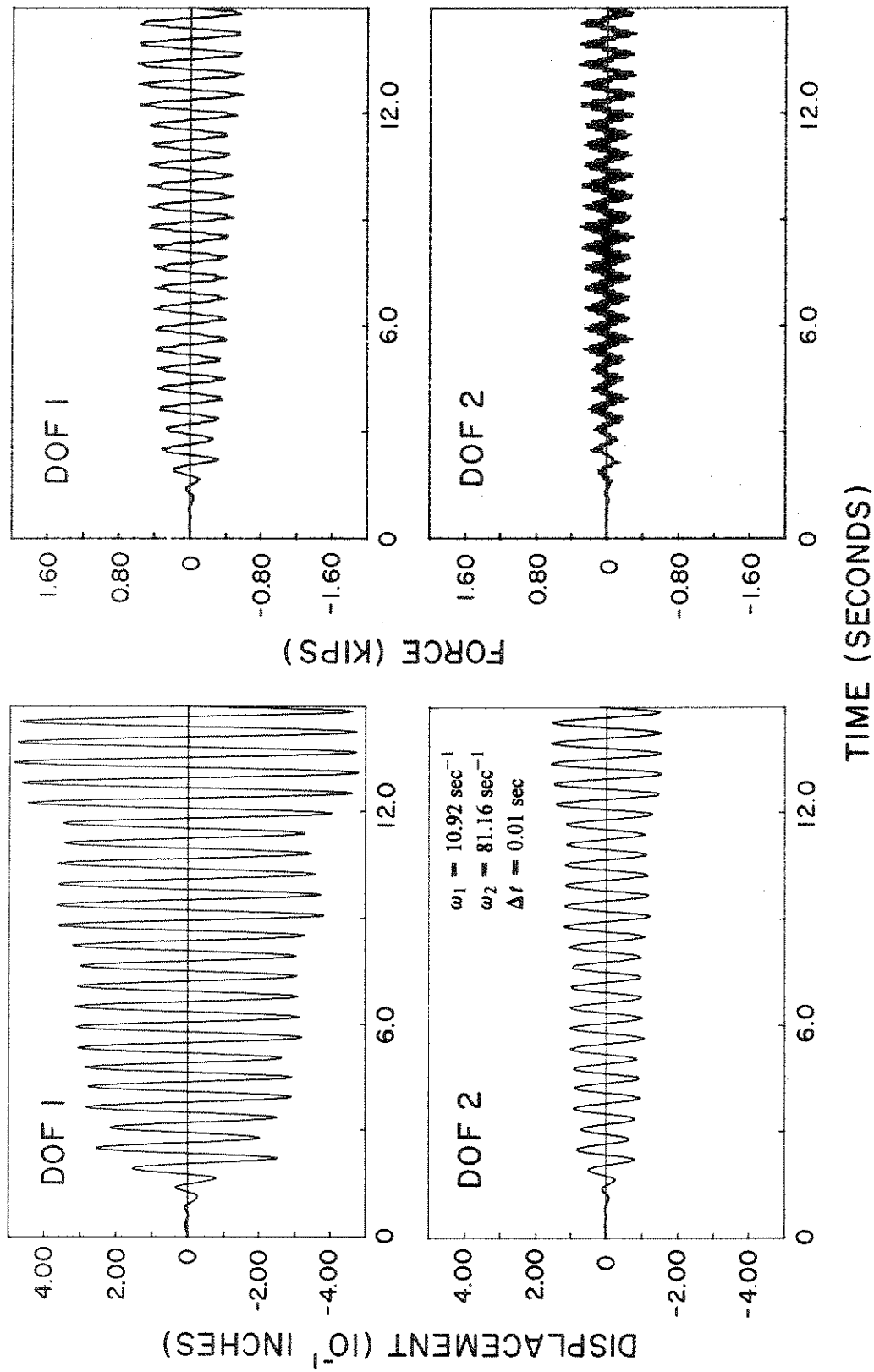


Fig. 7.2 Exact Numerical Responses of a 2 DOF System to El Centro 1940 (NS), 0.02g Ground Acceleration (Newmark Explicit Method)

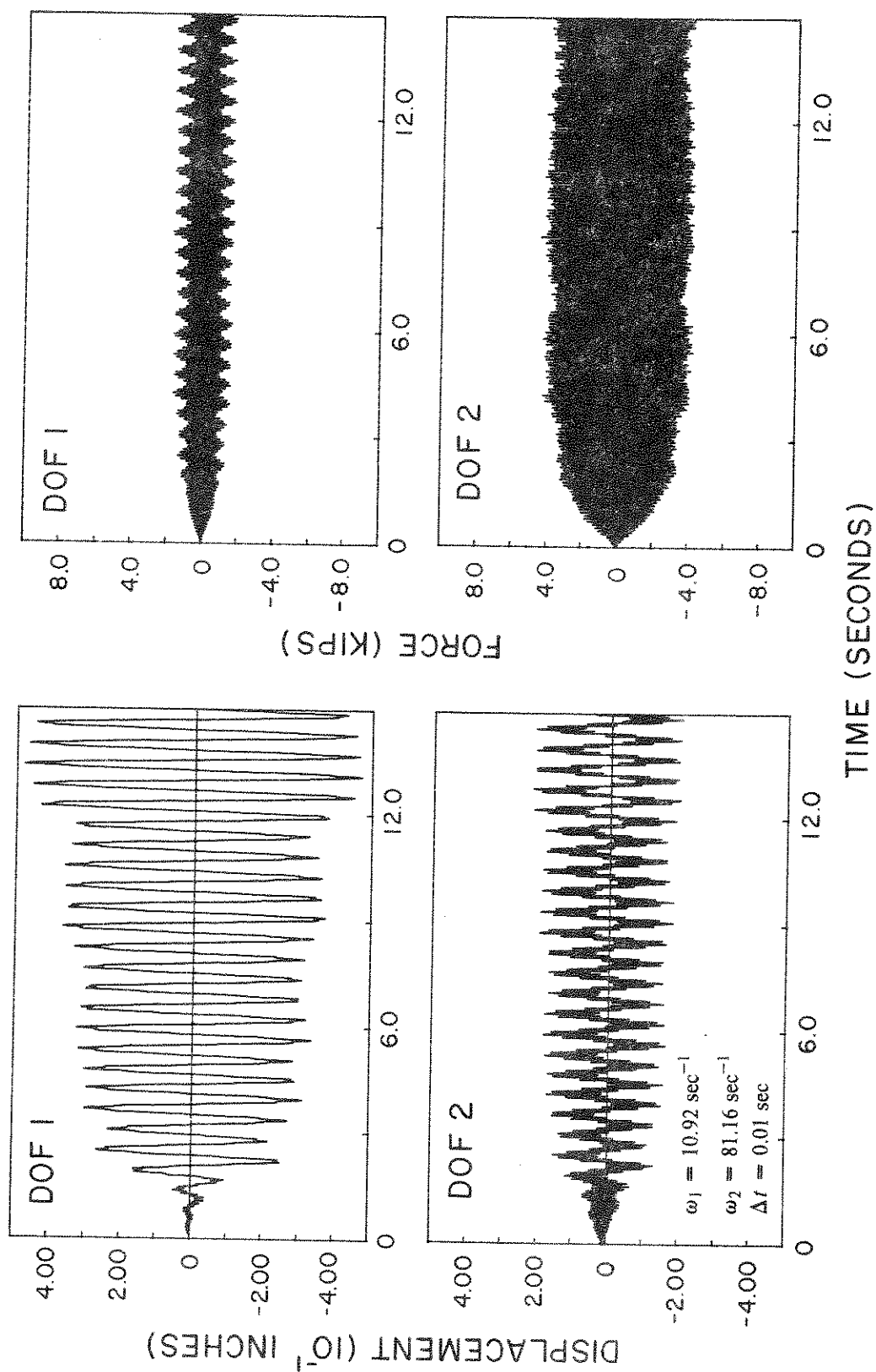


Fig. 7.3 Responses of a 2 DOF System with Systematic Errors ( $e_i$ ) to El Centro 1940 (NS), 0.02g Ground Acceleration



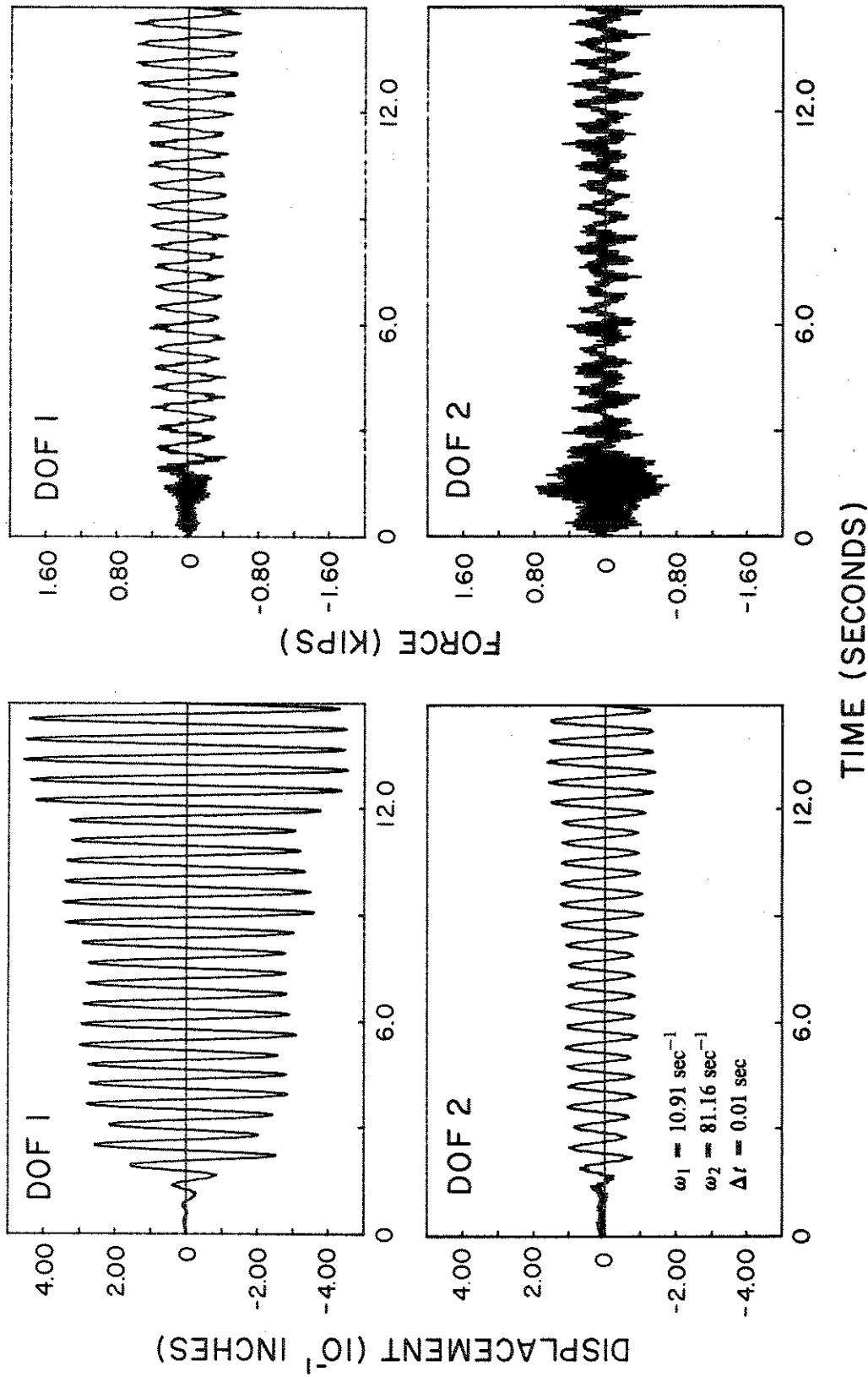


Fig. 7.4 Energy Compensated Responses of a 2 DOF System with Systematic Errors ( $\epsilon_f$ ) to El Centro 1940 (NS), 0.02g Ground Acceleration (Newmark Explicit Method)

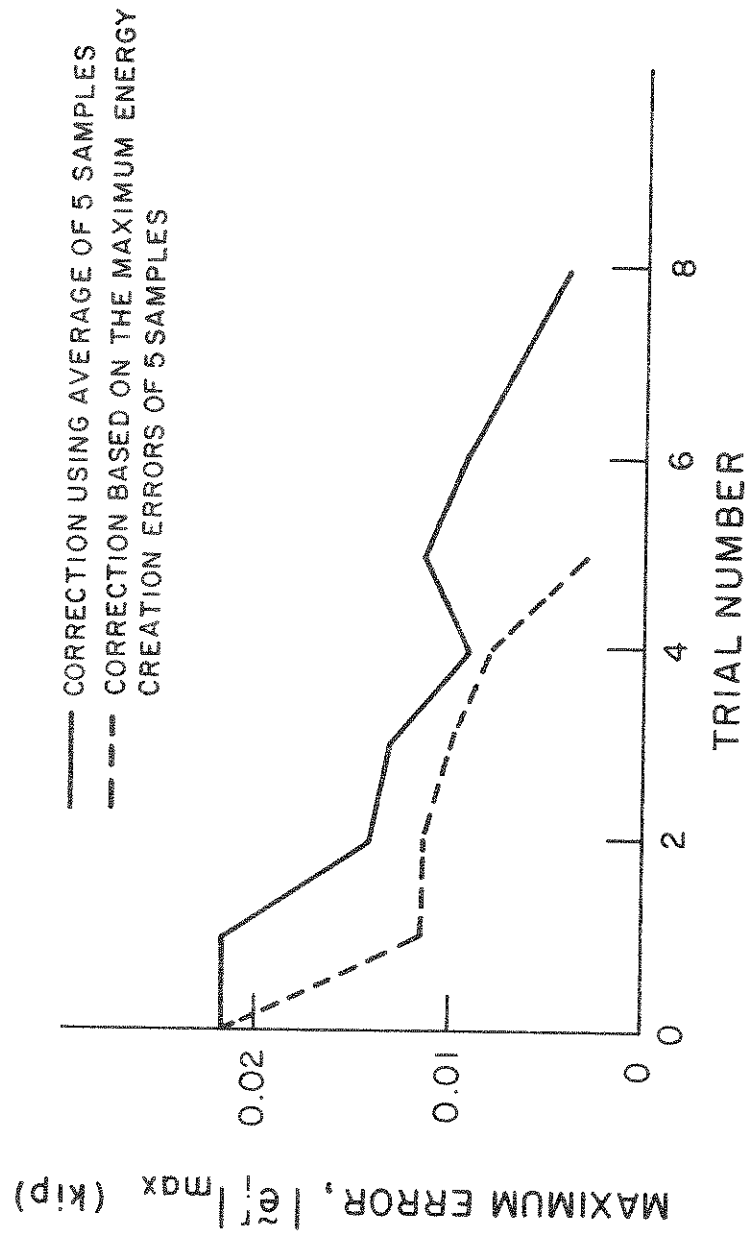


Fig. 7.5 Rates of Improvement by Equivalent Hysteretic Energy Correction in a 2 DOF System

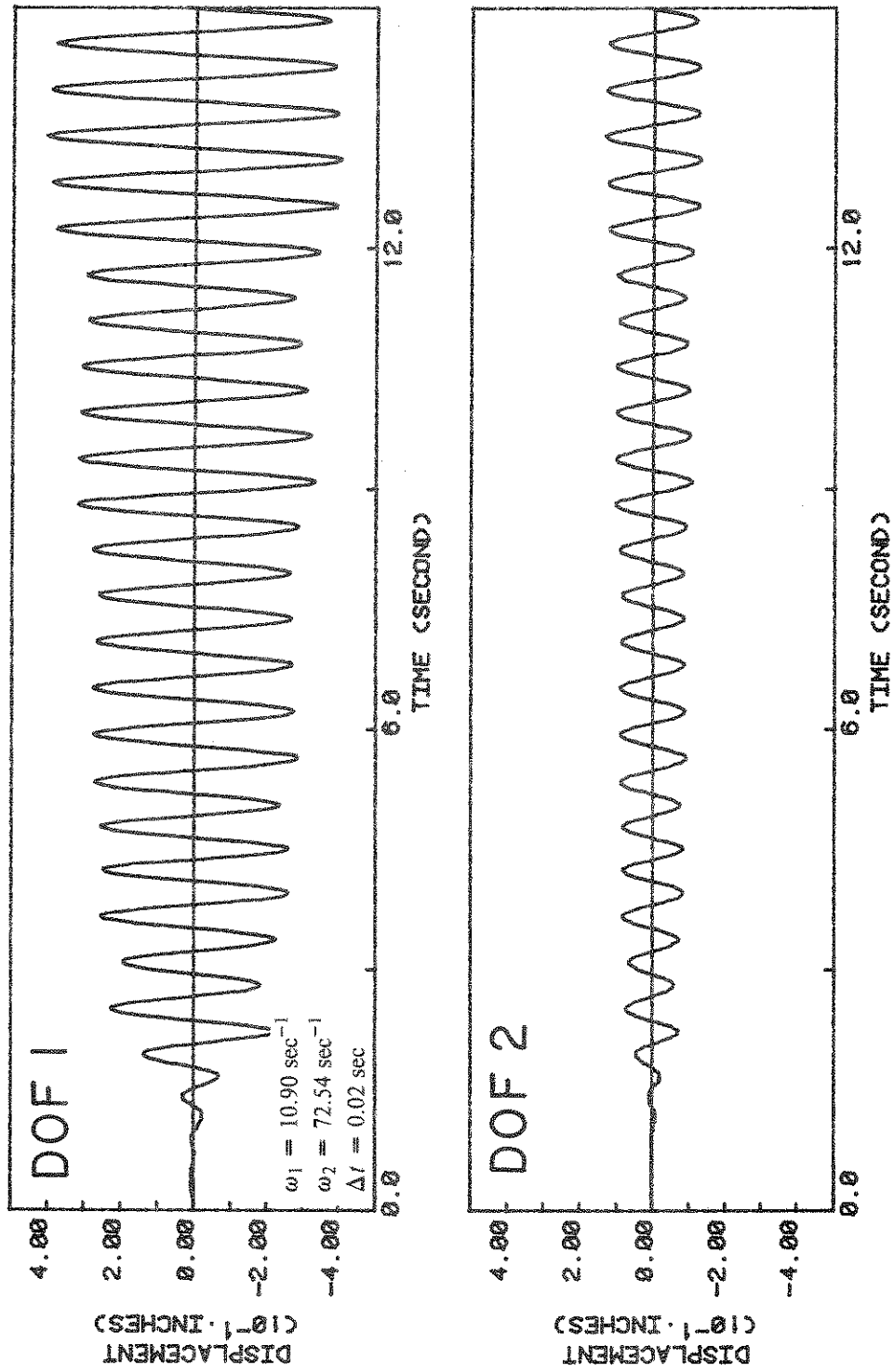


Fig. 7.6 Removal of High Frequency Noise in a 2 DOF System by Rayleigh Damping (the same example as in Figs. 5.3 and 5.7)

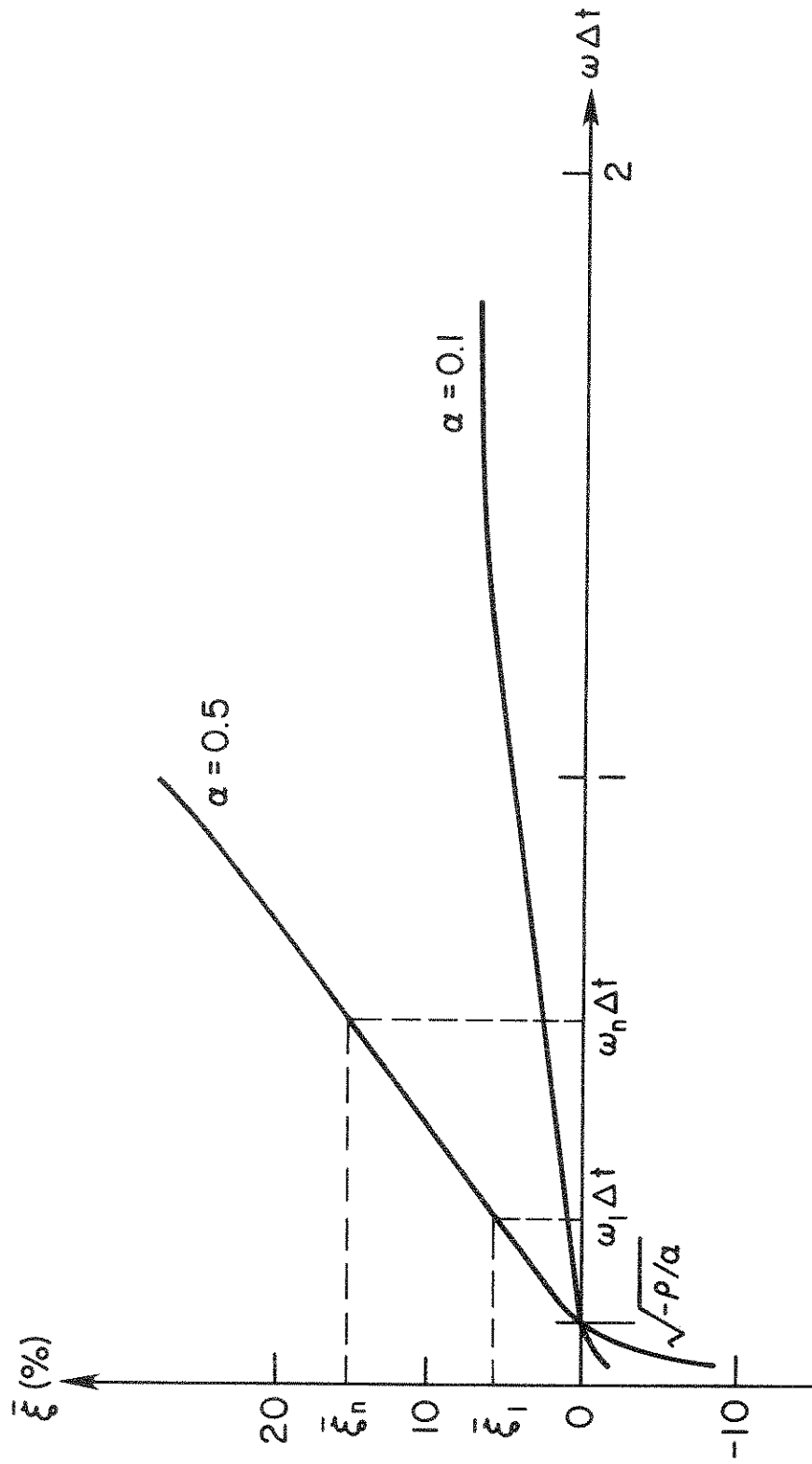


Fig. 7.7 Numerical Damping in the Modified Newmark Explicit Algorithm

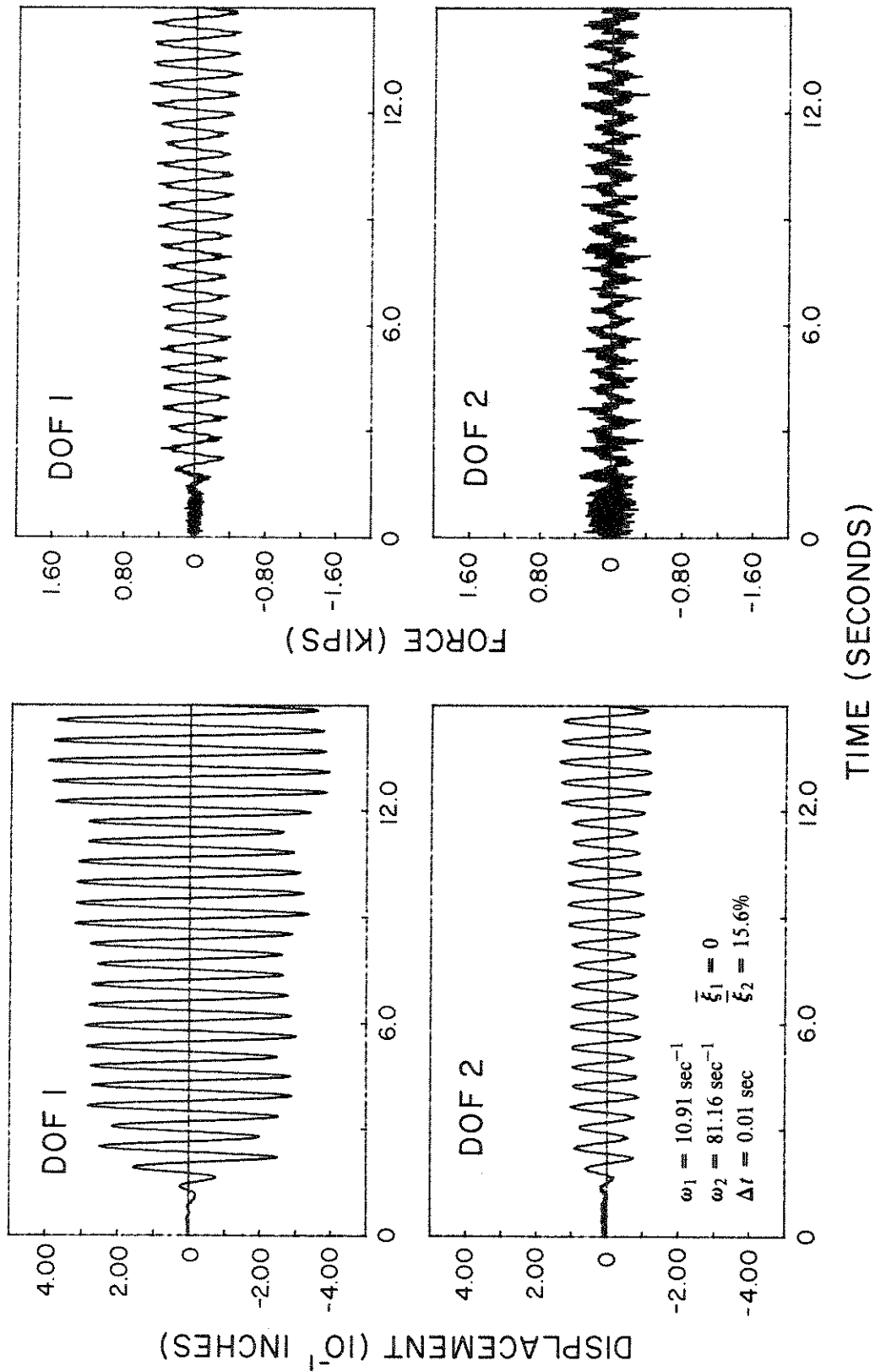
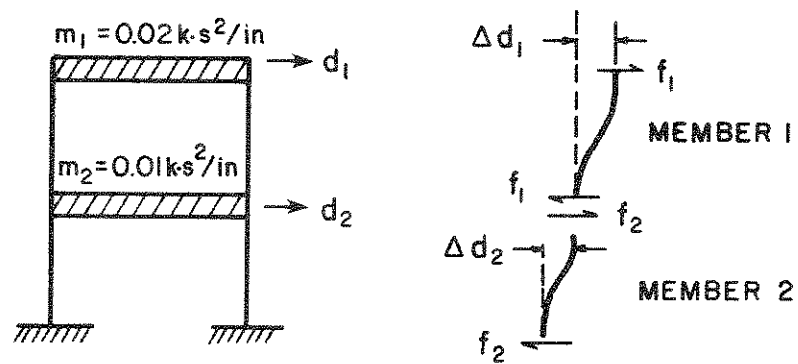
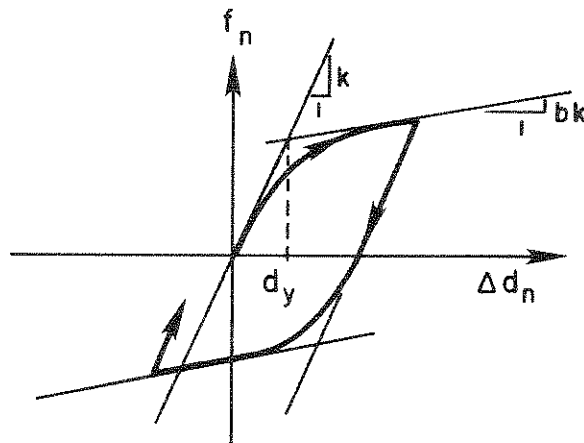


Fig. 7.8 Energy Compensated Responses of a 2 DOF System with Systematic Errors ( $e$ ) to El Centro 1940 (NS), 0.02g Ground Acceleration (Modified Newmark Algorithm,  $\alpha = 0.421$ ,  $\rho = -0.005$ )



(a) Shear Building



PARAMETERS	MEMBER 1	MEMBER 2
$k$	4 k/in	8 k/in
$d_y$	0.7 in	0.4 in
$b$	0.01	0.01
$R^*$	3	2

\*Parameter defining the curvature of the asymptotic curve

(b) Menegotto-Pinto Model

Fig. 7.9 Two-Story Shear Building with Inelastic Deformation

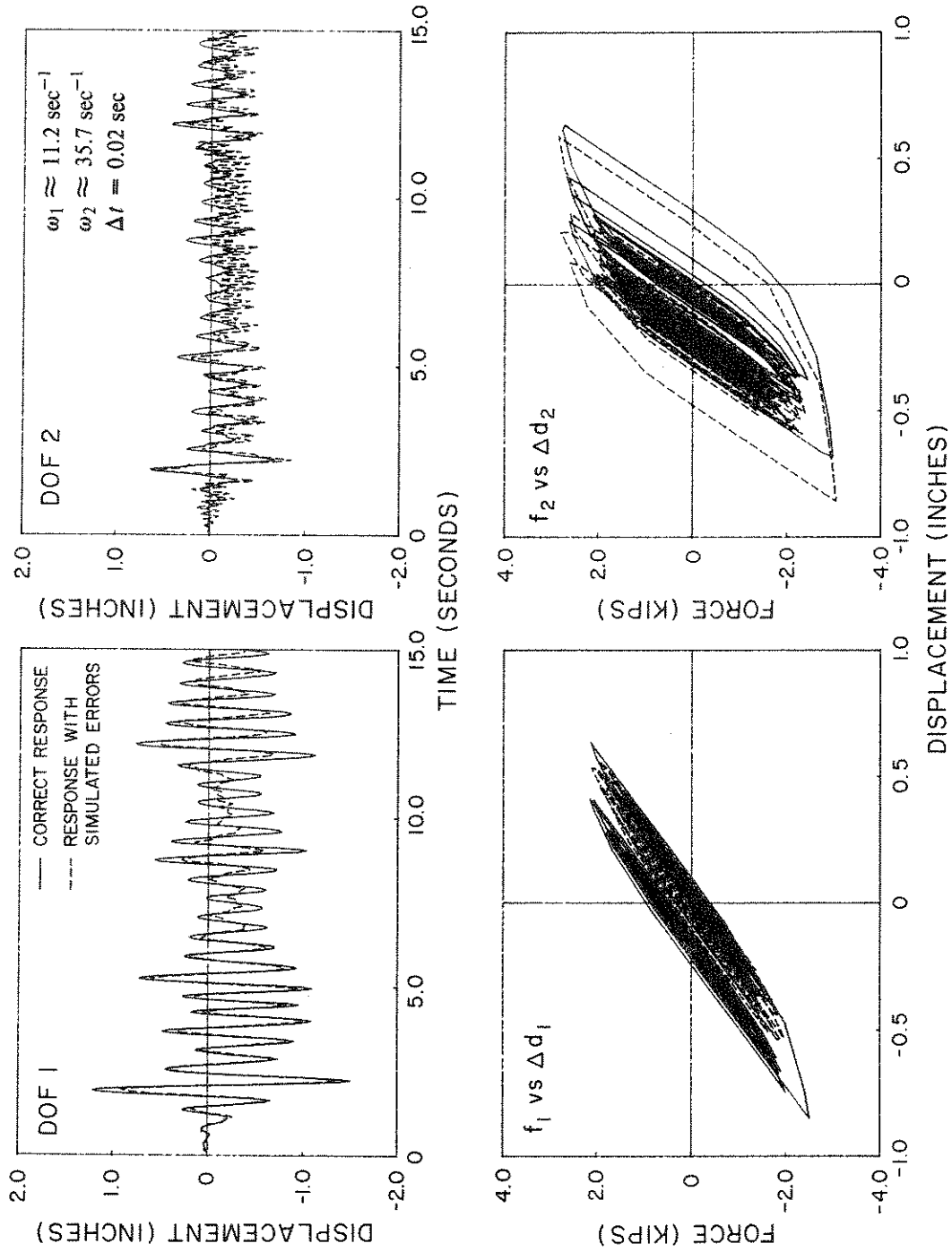


Fig. 7.10 Inelastic Responses of a Two-Story Shear Building with Systematic Errors ( $e_f$ ) to El Centro 1940 (NS), 0.18g Ground Acceleration (Newmark Explicit Algorithm)

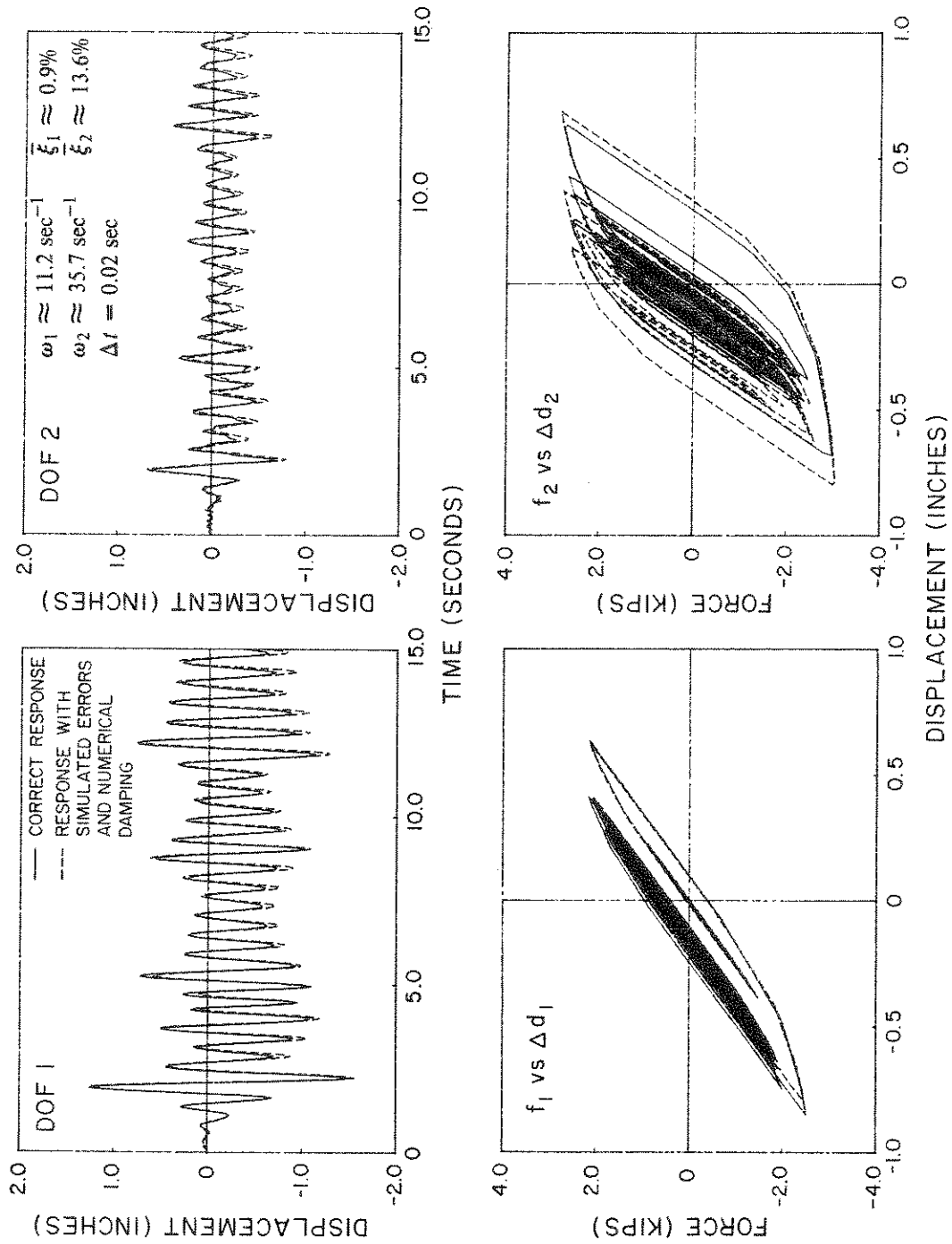


Fig. 7.11 Inelastic Responses of a Two-Story Shear Building with Systematic Errors ( $e'$ ) to El Centro 1940 (NS), 0.18g Ground Acceleration (Modified Newmark Algorithm,  $\alpha = 0.4$ ,  $\rho = -0.016$ )



## APPENDIX A

### MODELLING OF SYSTEMATIC ERRORS

#### A1. Transducer Calibration Errors

We assume that displacement and force transducers are mis-calibrated with small errors  $\pm \delta C_d$  and  $\pm \delta C_r$ , respectively, and that  $C_d$  and  $C_r$  are the correct calibration factors of the transducers. Due to the displacement transducer calibration error, the actually imposed and measured displacements are

$$\bar{d}_i^* = \bar{d}_i + e_i^{dc} \quad (\text{A1})$$

and

$$\hat{d}_i = \bar{d}_i^* + e_i^{dm}$$

respectively, where  $\bar{d}_i$  is the computed displacement; and  $e_i^{dc}$  and  $e_i^{dm}$  are the displacement control and measurement errors. The incremental displacement at each step is

$$\Delta \bar{d}_i^* = \bar{d}_i^* - \hat{d}_{i-1} \quad (\text{A2})$$

Because of the erroneous calibration factor, the displacement-voltage conversion is incorrect, and the actually imposed displacement becomes

$$\bar{d}_i^* = \bar{d}_{i-1}^* + \frac{\Delta \bar{d}_i^*}{C_d \pm \delta C_d} C_d \quad (\text{A3})$$

Neglecting the higher order terms of  $\delta C_d / C_d$ , we have

$$\bar{d}_i^* = \bar{d}_{i-1}^* + \Delta \bar{d}_i^* \left( 1 - \pm \frac{\delta C_d}{C_d} \right) \quad (\text{A4})$$

Substituting Eqs. (A1) and (A2) into Eq. (A4), we get

$$\bar{d}_i^* = \bar{d}_i - e_{i-1}^{dm} - \pm \frac{\delta C_d}{C_d} (\Delta \bar{d}_i - e_{i-1}^{dc} - e_{i-1}^{dm}) \quad (\text{A5})$$

in which  $\Delta \bar{d}_i = \bar{d}_i - \bar{d}_{i-1}$ . Due to the error in voltage-displacement conversion,

$$\hat{d}_{i-1} = \bar{d}_{i-1}^* \left( 1 \pm \frac{\delta C_d}{C_d} \right) \quad (\text{A6})$$

Consequently,  $e_{i-1}^{dm} = \pm \frac{\delta C_d}{C_d} \bar{d}_{i-1}^*$ . Substituting this into Eq. (A5) and neglecting the  $(\delta C_d / C_d) e_{i-1}^{dc}$  and  $(\delta C_d / C_d) e_{i-1}^{dm}$  terms, we obtain

$$\bar{d}_i^* = \bar{d}_i - \left( \pm \frac{\delta C_d}{C_d} \bar{d}_i \right) \quad (\text{A7})$$

Therefore, the displacement control and measurement errors are

$$e_i^{dc} = \pm \frac{\delta C_d}{C_d} \bar{d}_i \quad (\text{A8})$$

and

$$e_i^{dm} = - e_i^{dc}$$

Similary, because of the load transducer calibration error  $\pm \delta C_r$ , the measured force feedback is

$$\hat{r}_i = k \bar{d}_i^* \left( 1 \pm \frac{\delta C_r}{C_r} \right) \quad (\text{A9})$$

Consequently, the force measurement errors are

$$e_i^{rm} = \hat{r}_i - k \bar{d}_i^* = \pm \frac{\delta C_r}{C_r} k \bar{d}_i^* \quad (\text{A10})$$

Neglecting the  $(\delta C_r / C_r) e_i^{dc}$  term, we have

$$e_i^{rm} = \pm \frac{\delta C_r}{C_r} k \bar{d}_i \quad (\text{A11})$$

## A2. Actuator Displacement Calibration Error

If the calibration of actuator motion is inconsistent with displacement transducer calibration, such that there is an error  $\pm \delta C_j$ , the actually imposed displacement at step  $i$  becomes

$$\bar{d}_i^* = \bar{d}_{i-1}^* + \frac{\Delta \bar{d}_i^*}{C_j \pm \delta C_j} C_j \quad (\text{A12})$$

where  $C_j = C_d \times \text{SPAN}$  is the correct calibration factor of actuator displacement (see Fig. 2.2); and

$$\Delta \bar{d}_i^* = \bar{d}_i - \bar{d}_{i-1}^* \quad (\text{A13})$$

by assuming that displacement measurement errors do not exist. Substituting Eq. (A13) into Eq. (A12), and neglecting  $(\delta C_j / C_j) e_{i-1}^{dc}$  and the higher order terms of  $\delta C_j / C_j$ , we have

$$\bar{d}_i^* = \bar{d}_i \pm \frac{\delta C_j}{C_j} \Delta \bar{d}_i \quad (\text{A14})$$

Therefore, the displacement-control errors are

$$e_i^{dc} = \pm \frac{\delta C_j}{C_j} \Delta \bar{d}_i \quad (\text{A15})$$

## APPENDIX B

### EXPLICIT INTEGRATION ALGORITHMS

#### B1. Formulations and Numerical Properties

##### (i) Basic Central Difference Method

Without viscous damping, the dynamic equilibrium of a SDOF system at time  $t = i \Delta t$  is

$$m a_i + r_i = f_i \quad (B1)$$

where  $r_i = k d_i$ . In the basic central difference method, the velocity and acceleration terms are approximated by

$$v_i = \frac{d_{i+1} - d_{i-1}}{2 \Delta t} \quad (B2)$$

$$a_i = \frac{d_{i+1} - 2 d_i + d_{i-1}}{\Delta t^2}$$

respectively. Substituting the acceleration term in Eq. (B1) with Eq. (B2), we have the numerical formulation:

$$d_{i+1} = 2 d_i - d_{i-1} + \frac{\Delta t^2}{m} (f_i - r_i) \quad (B3)$$

Further, by letting  $r_i = k d_i$  and  $f_i = 0$  in Eq. (B3), we can obtain a recursive matrix form of free-vibration response:

$$\mathbf{x}_{i+1} = \mathbf{A} \mathbf{x}_i \quad (B4a)$$

where

$$\mathbf{x}_i = \begin{Bmatrix} d_i \\ d_{i-1} \end{Bmatrix} \quad (B4b)$$

and

$$\mathbf{A} = \begin{bmatrix} 2 - \omega^2 \Delta t^2 & -1 \\ 1 & 0 \end{bmatrix}$$

*Stability.* A numerical method is stable if the free-vibration response computed by it will not grow without bound for any initial conditions. From Eq. (B4), we can see that  $d_n = c_1 \lambda_1^n + c_2 \lambda_2^n$ , where  $\lambda_{1,2}$  are the eigenvalues of  $\mathbf{A}$  (refer to Sec. 3.3). Therefore, the method is stable if  $|\lambda_{1,2}| \leq 1$ . Furthermore,  $\lambda_{1,2}$  must be complex conjugates in order to have oscillatory response. By solving the eigenvalue problem  $(\mathbf{A} - \lambda \mathbf{I}) = 0$ , we have

$$\lambda_{1,2} = A \pm i B \quad (\text{B5a})$$

where

$$A = 1 - \frac{\omega^2 \Delta t^2}{2} \quad (\text{B5b})$$

$$B = \frac{\sqrt{4 - (\omega^2 \Delta t^2 - 2)^2}}{2}$$

To satisfy the stable oscillatory response conditions, we must have  $(A^2 + B^2) \leq 1$  and  $B$  be real. Since  $(A^2 + B^2)$  is always equal to 1, according to Eq. (B5b), we have the stability condition that

$$(\omega^2 \Delta t^2 - 2)^2 \leq 4 \quad (\text{B6})$$

which implies

$$0 \leq \omega \Delta t \leq 2 \quad (\text{B7})$$

When  $B = 0$ , the response is non-oscillatory, but stable.

*Accuracy.* The accuracy of a numerical method is measured by the deviation of numerical damping  $\bar{\xi}$  and frequency  $\bar{\omega}$  from the true  $\xi$  and  $\omega$  values of a system. According to Eqs.

(3.20) and (B5b), we have

$$\bar{\xi} = 0 \quad (\text{B8})$$

and

$$\bar{\omega} = \frac{1}{\Delta t} \arctan \left( \frac{\sqrt{4 - (\omega^2 \Delta t^2 - 2)^2}}{2 - \omega^2 \Delta t^2} \right)$$

Therefore, the central difference method does not have numerical dissipation property. From Eq. (B8), we can find that  $(\omega - \bar{\omega})/\omega$  is smaller than 1% when  $\omega \Delta t$  is less than 0.5. Consequently, both accuracy and stability can be achieved with reasonably small  $\Delta t$ .

*(ii) Newmark Explicit Method*

Using the Newmark integration method [11], we consider the equilibrium equation:

$$m a_{i+1} + r_{i+1} = f_{i+1} \quad (\text{B9})$$

and assume that the velocity and acceleration can be approximated by

$$v_{i+1} = v_i + [(1 - \alpha) a_i + \alpha a_{i+1}] \Delta t \quad (\text{B10})$$

$$d_{i+1} = d_i + v_i \Delta t + \left[ \left( \frac{1}{2} - \beta \right) a_i + \beta a_{i+1} \right] \Delta t^2 \quad (\text{B11})$$

where  $\alpha$  and  $\beta$  are parameters selected by the user. By letting  $\alpha = 1/2$  and  $\beta = 0$  in the above equations, we immediately obtain an explicit algorithm as

$$d_{i+1} = d_i + \Delta t v_i + \frac{\Delta t^2}{2} a_i \quad (\text{B12})$$

$$a_{i+1} = \frac{1}{m} (f_{i+1} - r_{i+1}) \quad (\text{B13})$$

$$v_{i+1} = v_i + \frac{\Delta t}{2} (a_i + a_{i+1}) \quad (\text{B14})$$

By setting  $f_{i+1} = 0$  and  $r_{i+1} = k d_{i+1}$ , we can obtain a recursive matrix equation of free vibration as Eq. (B4a) with

$$\mathbf{x}_i = \begin{Bmatrix} d_i \\ v_i \\ a_i \end{Bmatrix} \quad (\text{B15})$$

and

$$\mathbf{A} = \begin{bmatrix} 1 & \Delta t & \frac{\Delta t^2}{2} \\ -\frac{\omega^2 \Delta t}{2} & 1 - \frac{\omega^2 \Delta t^2}{2} & \frac{\Delta t - \omega^2 \Delta t^3}{2} \\ -\omega^2 & -\omega^2 \Delta t & -\frac{\omega^2 \Delta t^2}{2} \end{bmatrix}$$

In this case, the first two eigenvalues,  $\lambda_{1,2}$ , of  $\mathbf{A}$  turn out to be identical to those in (i), and  $\lambda_3 = 0$ . Therefore, this method has the same numerical properties as the basic central difference method.

### (iii) Summed Form of the Central Difference Method

From Eq. (B9), the dynamic equilibrium at  $t = (i + 1) \Delta t$ , we get

$$a_{i+1} = \frac{1}{m} (f_{i+1} - r_{i+1}) \quad (\text{B16})$$

Defining a new term  $z_i = (d_{i+1} - d_i)/\Delta t$ , we have

$$d_{i+1} = d_i + \Delta t z_i \quad (\text{B17})$$

Hence, knowing  $z_{i+1} - z_i = (d_{i+2} - 2 d_{i+1} + d_i)/\Delta t$ , we can obtain from Eqs. (B2) and (B16) the expression

$$z_{i+1} = z_i + \frac{\Delta t}{m} (f_{i+1} - r_{i+1}) \quad (\text{B18})$$

Eqs. (B17) and (B18) are the summed form of the central difference method. It can avoid unfavorable rounding errors which will occur in the basic central difference method when  $\Delta t$  is very small [14].

In a similar way as before, we find a recursive matrix formula with

$$\mathbf{x}_i = \begin{Bmatrix} d_i \\ z_i \end{Bmatrix} \quad (\text{B19})$$

and

$$\mathbf{A} = \begin{bmatrix} 1 & \Delta t \\ -\omega^2 \Delta t & 1 - \omega^2 \Delta t^2 \end{bmatrix}$$

The eigenvalues of  $\mathbf{A}$  are again identical to those in Eq. (B5). Therefore, the numerical properties here are similar to those of the two previous methods.

## B2. Transformability of the Explicit Algorithms

The three explicit integration algorithms just discussed have identical numerical properties. This can be expected if we know that they are transformable to one another and are mathematically identical. This will be shown in the following.

### (i) Summed Form to Basic Central Difference Form

Because of Eq. (B17), we have

$$d_{i+1} - d_i = d_i - d_{i-1} + \Delta t (z_i - z_{i-1}) \quad (\text{B20})$$

Substituting  $z_i - z_{i-1}$  in Eq. (B20) with Eq. (B18), we obtain Eq. (B3).

### (ii) Newmark Explicit Form to Basic Central Difference Form

Because of Eq. (B12), we have

$$d_{i+1} - d_i = d_i - d_{i-1} + \Delta t (v_i - v_{i-1}) + \frac{\Delta t^2}{2} (a_i - a_{i-1}) \quad (\text{B21})$$



Substituting  $v_i - v_{i-1}$  in Eq. (B21) with Eq. (B14), we get

$$d_{i+1} - d_i = d_i - d_{i-1} + \Delta t^2 a_i \quad (\text{B22})$$

which is again Eq. (B3) by substituting  $a_i$  with Eq. (B13).

However, because of the different numerical forms, these methods can have different magnitudes of rounding errors and error-propagation properties when computations are carried out with a digital computer and experimental feedback is used during a pseudodynamic test.

# APPENDIX C

## ERROR PROPAGATION EQUATION FOR THE BASIC CENTRAL DIFFERENCE METHOD

From the basic central difference method, we can identify the following characteristic matrices and vectors:

$$\mathbf{A} = \begin{bmatrix} 2 - \omega^2 \Delta t^2 & -1 \\ 1 & 0 \end{bmatrix}$$

$$\mathbf{B} = \begin{bmatrix} 2 & -1 \\ 1 & 0 \end{bmatrix} \quad (\text{C1})$$

$$\mathbf{L} = \begin{bmatrix} \frac{\Delta t^2}{m} \\ 0 \end{bmatrix}$$

$$\mathbf{S} = \{\omega^2 m, 0\}$$

Since  $\mathbf{x}_i = \{d_i, d_{i-1}\}^T$ , errors introduced in each step can be modelled as  $\mathbf{e}_i^d = \{e_i^d, 0\}^T$  and  $\mathbf{e}_i^{rd} = \{e_i^{rd}, 0\}^T$ , respectively. Using these error vectors and Eq. (C1), we can obtain from Eq. (3.23) that

$$\alpha_{ii} = 2 e_i^d \quad (\text{C2a})$$

$$\alpha_{(i+1) i} = (4 A - 1) e_i^d$$

and

$$\beta_{ii} = 2 (1 - A) e_i^{rd} \quad (\text{C2b})$$

$$\beta_{(i+1) i} = 4 (1 - A) A e_i^{rd}$$

in which  $A$  is the real part of the eigenvalues  $\lambda_{1,2}$  of  $\mathbf{A}$ , as defined in Eq. (B5) in Appendix B. Since the third eigenvalue  $\lambda_3$  does not exist and  $\bar{\xi} = 0$ , as shown in Appendix B, Eqs. (3.22b)

and (3.22c) give

$$\alpha_{ni} = a_{1i} \cos \bar{\omega} \Delta t (n-i) + a_{2i} \sin \bar{\omega} \Delta t (n-i) \quad (\text{C3a})$$

$$\beta_{ni} = b_{1i} \cos \bar{\omega} \Delta t (n-i) + b_{2i} \sin \bar{\omega} \Delta t (n-i) \quad (\text{C3b})$$

By substituting Eq. (C2a) into Eq. (C3a), we can solve for  $a_{1i}$  and  $a_{2i}$ :

$$a_{1i} = 2 e_i^d \quad (\text{C4a})$$

$$a_{2i} = \frac{2 A - 1}{B} e_i^d$$

knowing that  $A = \cos \bar{\omega} \Delta t$  and  $B = \sin \bar{\omega} \Delta t$  from Eq. (3.19). Similarly, we find

$$b_{1i} = 2 (1 - A) e_i^{rd} \quad (\text{C4b})$$

$$b_{2i} = \frac{2 (1 - A) A}{B} e_i^{rd}$$

Substituting these parameters back into Eq. (3.22), we arrive at Eq. (3.30), the cumulative displacement error equation.

## APPENDIX D

### MODIFIED NEWMARK EXPLICIT ALGORITHM WITH NUMERICAL DAMPING

The modified Newmark explicit algorithm formulated in Eq. (7.10) can be written in a recursive matrix form as

$$\mathbf{x}_{i+1} = \mathbf{A} \mathbf{x}_i \quad (\text{D1a})$$

where

$$\mathbf{x}_i = \begin{Bmatrix} d_i \\ \Delta t \, v_i \\ \Delta t^2 \, a_i \end{Bmatrix} \quad (\text{D1b})$$

$$\mathbf{A} = \begin{bmatrix} 1 & 1 & \frac{1}{2} \\ -\frac{\Omega^2}{2} & 1-(1+\alpha)\frac{\Omega^2}{2}-\frac{\rho}{2} & \frac{1}{2}-(1+\alpha)\frac{\Omega^2}{4}-\frac{\rho}{4} \\ -\Omega^2 & -(1+\alpha)\Omega^2-\rho & -(1+\alpha)\frac{\Omega^2}{2}-\frac{\rho}{2} \end{bmatrix}$$

Matrix  $\mathbf{A}$  has eigenvalues

$$\lambda_{1,2} = A_1 \pm (A_1^2 - A_2)^{1/2} \quad (\text{D2a})$$

and

$$\lambda_3 = 0$$

where

$$A_1 = 1 - (1 + \alpha) \frac{\Omega^2}{2} - \frac{\rho}{2} \quad (\text{D2b})$$

$$A_2 = 1 - \alpha \Omega^2 - \rho$$

To satisfy the stable oscillatory condition, we must have  $A_1^2 < A_2 \leq 1$ , such that  $\lambda_{1,2}$  are complex conjugates and  $|\lambda_{1,2}| \leq 1$ , as discussed in Appendix B. When  $A_1^2 = A_2$ , the algorithm will have a non-oscillatory solution, but the solution will remain stable if  $A_1 \leq 1$ . The condition  $A_1^2 \leq A_2$  implies that

$$\frac{-1 + \sqrt{1 - (1 + \alpha)\rho}}{1 + \alpha} \leq \Omega \leq \frac{1 + \sqrt{1 - (1 + \alpha)\rho}}{1 + \alpha} \quad (\text{D3a})$$

and from  $A_2 \leq 1$ , we have

$$\Omega \geq \sqrt{-\frac{\rho}{\alpha}} \quad (\text{D3b})$$

If  $\rho$  is always negative and  $\alpha$  is positive, we can combine the conditions in Eqs. (D3a) and (D3b) as

$$\sqrt{-\frac{\rho}{\alpha}} \leq \Omega \leq \frac{1 + \sqrt{1 - (1 + \alpha)\rho}}{1 + \alpha} \quad (\text{D4})$$

This is the stability condition for the modified Newmark explicit algorithm.